

# **Fabrication and Properties of 1-Dimensional TiO<sub>2</sub> and ZnO Nanocomposites Prepared by Hydrothermal Method**

**by**

**Phuong Dao**

---

---

**This work has been carried out at Department of Micro and Nano Systems  
Technology, under the supervision of**

**Professor Kaiying Wang**

**University College of Southeast Norway**

**Vestfold, May 2016**

# Abstract

The necessary of renewable energies as the replacement for fossil fuel such as fuel gas from CO<sub>2</sub> or hydrogen from photoelectrochemical water splitting process are feasible by using semiconductors as photocatalysts. Among many photocatalytic candidates, titanium dioxide and zinc oxide are the most widely investigated and the most suitable for industrial scale applications due to their attractive physical and chemical properties. In this work, we report the synthesis and photocatalytic properties of silicon doped TiO<sub>2</sub> nanotubes (TNTs) and the composite of silicon dioxide and gold layer on ZnO nanorods arrays simply by hydrothermal method.

The diameter of the TiO<sub>2</sub> nanotubes is about 20 nm with several micrometers in length and dopant (Si/(Si+Ti)) molar ratio in range of 1~30%. X-ray diffraction analysis verifies formation of nanocrystalline anatase phase for both pristine and Si-doped TNTs. The light absorption spectra of doped TNTs exhibit red shift from 375 nm to 410 nm as compared with that of the un-doped TNTs. Photodegradation experiment shows that this red-shift of spectra absorption is desirable for the redox reaction under relatively long wavelength light illumination.

The morphology of ZnO nanorods array is quite uniform with the rod length in range of 1-2 micrometers and the rod diameter in range of several hundred micrometers. UV-vis absorption spectra of SiO<sub>2</sub> coated ZnO nanorods performs the red shift and the results from photodegradation test indicate a slight increase in the photocatalytic activity of SiO<sub>2</sub> coated ZnO nanorods compared to the pristine one. When incorporating SiO<sub>2</sub> onto Au-ZnO nanorods plasmonic structure, a great enhancement in photocurrent and a rapid photoresponse were observed. This unique structure is favorable for high performance of photoelectrochemical water splitting.

This work elucidates the economic and efficient hydrothermal pathway to produce nanostructure of photocatalyst. By further modification, both TiO<sub>2</sub> nanotubes and ZnO nanorods array shows a promising potential as photocatalyst.

# Preface

This thesis is submitted in partial fulfilment of the requirements for the Master degree from the Department of Micro and Nano Systems Technology in the Faculty of Technology and Maritime Sciences at University college of Southeast Norway.

The work has been carried out from September 2015 to May 2016, at the Department of Micro and Nano Systems Technology at University college of Southeast Norway.

# Acknowledgements

Deeply in my heart, I would like to express my gratitude to my supervisor, Professor Kaiying Wang, for his valuable guidance, keen interest and encouragement at various stages of my thesis project. The unique idea from his expert knowledge initiated my inspiration in designing and conducting my project.

Together with Kaiying, I am very much thankful Kang Du and Dr. Guohua Liu. They not only gave excellent comments to instruct me to a right way but they also shared their valuable experience as a scientist.

I would also like to express my acknowledgement to the Department of Micro and Nano Systems Technology for the most useful facility and invaluable administrative assistance. I want to thank Ms. Zekija Ramic for her enthusiasm in supporting me the equipment and chemicals. I send a thank you to Mr. Tuan Nguyen, Mr. Ragnar Dahl Johansen, Mr. Thomas Martinsen and Mr. Tayyib Muhammad for their instruction during the period in lab.

Especially, I would like to express a thankful gratitude to my dear friend Vy Nguyen, Huyen Nguyen, Duy Le, Thong Huynh, Duyen Do, Hoa Tran, Khuong Pham who supported me in both emotional and scientific ways.

Last but not least, I wish to thank my beloved parents for their encouragement and their love for me.

# CONTENTS

<b>Abstract.....</b>	<b>II</b>
<b>Preface.....</b>	<b>III</b>
<b>Acknowledgements .....</b>	<b>IV</b>
<b>List of Figures.....</b>	<b>VIII</b>
<b>List of Tables .....</b>	<b>X</b>
<b>Acronyms.....</b>	<b>XI</b>
<b>CHAPTER 1. INTRODUCTION .....</b>	<b>1</b>
1.1 The necessary of renewable energy .....	1
1.2 Chemical energy conversion .....	1
1.2.1 Producing hydrogen gas from water .....	2
1.2.2 Producing fuel gas from CO <sub>2</sub> .....	3
1.3 TiO <sub>2</sub> photocatalyst approaching and modifying.....	4
1.4 ZnO photocatalyst approaching and modifying.....	5
1.5 Organization.....	6
<b>CHAPTER 2. LITERATURE SURVEY OF 1D TiO<sub>2</sub> AND ZnO NANOMATERIALS.....</b>	<b>8</b>
2.1 Literature review of silicon doped TiO <sub>2</sub> nanotubes .....	8
2.1.1 Methods for producing Si-doped TiO <sub>2</sub> .....	8
2.1.1.1 Sol-gel technique .....	8
2.1.1.2 Thermal plasma and oxide bath technique .....	9
2.1.1.3 Chemical vapor deposition technique.....	9
2.1.1.4 Impregnation, precipitation, co-precipitation technique.....	10
2.1.1.5 Hydrothermal technique .....	10
2.1.2 The influences of silica to TiO <sub>2</sub> photochemical properties.....	14
2.1.2.1 Band gap extension.....	14
2.1.2.2 Band gap narrowing.....	15
2.1.3 Proposed mechanism by using TMAH as template in hydrothermal pathway..	15
2.1.4 Tubular formation mechanism using NaOH as template in hydrothermal pathway .....	17
2.1.4.1 Acid washing mechanism.....	18
2.1.4.2 Peeling-scrolling mechanism.....	18
2.1.4.3 Seeding-oriented crystal growth mechanism.....	19
2.2 Literature review of silicon dioxide and gold on ZnO nanorods array composite nanostructures.....	20
2.2.1 Methods for producing ZnO nanorods.....	20
2.2.1.1 Physical vapor deposition.....	20
2.2.1.2 Metal-organic chemical vapor deposition .....	20

2.2.1.3	Pulsed laser deposition .....	21
2.2.1.4	Electrospinning .....	21
2.2.1.5	Wet chemical method .....	21
2.2.1.6	Others.....	22
2.2.2	The hydrothermal growth mechanism of ZnO nanorods.....	22
2.2.2.1	In water medium.....	22
2.2.2.2	In alkali medium.....	23
2.2.2.3	In amine medium.....	23
2.2.3	Silicon incorporation.....	24
2.2.4	Gold incorporation.....	25
2.2.4.1	Electron trap sites and spatial electricfield enhancement.....	25
2.2.4.2	Surface plasmon resonance (SPR).....	26
<b>CHAPTER 3. MATERIALS FABRICATION.....</b>		<b>29</b>
3.1	Si doped TiO <sub>2</sub> nanotubes synthesis .....	29
3.1.1	Hydrothermal reaction using TMAH as reagent.....	29
3.1.2	Hydrothermal reaction using NaOH as reagent.....	29
3.2	SiO <sub>2</sub> and Au layer on ZnO nanorods array synthesis.....	29
3.2.1	Hydrothermal growth of ZnO nanorods directly on Zn metal using DI water ..	29
3.2.2	Hydrothermal growth of ZnO nanorods directly on Zn metal using KOH.....	30
3.2.3	Two steps hydrothermal growth of ZnO nanorods on ITO glass .....	30
3.2.4	Deposition of the silicon oxide and gold layer .....	31
3.2.4.1	Deposition of SiO <sub>2</sub> on ZnO nanorods array synthesized by using KOH....	32
3.2.4.2	Deposition of SiO <sub>2</sub> and Au on ZnO nanorods array on ITO glass .....	32
<b>CHAPTER 4. MATERIALS CHARACTERIZATION AND MEASUREMENTS ...</b>		<b>34</b>
4.1	Hydrothermal equipment.....	34
4.2	Materials characterization .....	34
4.2.1	Scanning electron microscopy (SEM), Energy-dispersive X-ray spectroscopy (EDX) and Mapping .....	34
4.2.2	X-ray diffraction (XRD) .....	36
4.2.3	Uv-vis absorption.....	36
4.2.4	Transmission electron microscopy (TEM) .....	37
4.3	Measurements.....	38
4.3.1	Methylene blue (MB) degradation test of Si doped TNTs .....	38
4.3.2	Methylene blue degradation test of ZnO nanorods array on Zn metal .....	39
4.3.3	Photoelectrochemical (PEC) measurement of ZnO nanorods array on ITO glass .....	39
4.3.3.1	Steady state measurement.....	39
4.3.3.2	Transient photoresponse .....	39
<b>CHAPTER 5. RESULTS AND DISCUSSION.....</b>		<b>41</b>
5.1	Silicon doped TiO <sub>2</sub> nanotubes.....	41

5.1.1	Morphology of titania using TMAH as reagent.....	41
5.1.2	Morphology of titania nanotubes using NaOH as reagent.....	42
5.1.2.1	Backscattering electron.....	42
5.1.2.2	Secondary electron .....	43
5.1.3	Transmission electron microscopy (TEM).....	43
5.1.4	Composition of TiO <sub>2</sub> nanotubes.....	44
5.1.5	Crystal structure of TiO <sub>2</sub> nanotubes.....	46
5.1.6	UV-visible absorption test .....	47
5.1.7	Methylene blue degradation test .....	49
5.2	Composite of SiO <sub>2</sub> and Au on ZnO nanorods array.....	50
5.2.1	Morphology of ZnO nanorods on Zn foil using water.....	50
5.2.2	Investigating the optical properties of various SiO <sub>2</sub> layer thickness incorporating ZnO nanorods on Zn foil using KOH.....	50
5.2.2.1	Morphology of ZnO nanorods on Zn foil using KOH.....	50
5.2.2.2	The UV-vis absorption test.....	51
5.2.2.3	Methylene blue degradation test.....	52
5.2.3	Investigation the photocurrent properties of difference plasmonic configurations .....	53
5.2.3.1	Morphology of ZnO nanorods before and after sputtering.....	53
5.2.3.2	The UV-vis absorption test.....	54
5.2.3.3	PEC measurement.....	55
<b>CHAPTER 6. CONCLUSIONS AND PROSPECTS.....</b>		<b>61</b>
6.1	Achievements.....	61
6.1.1	TiO <sub>2</sub> approach.....	61
6.1.2	ZnO approach .....	61
6.2	Prospects.....	62
6.2.1	TiO <sub>2</sub> approach.....	62
6.2.2	ZnO approach .....	62
<b>References.....</b>		<b>63</b>
<b>Appendix.....</b>		<b>74</b>

## LIST OF FIGURES

Fig 1.1. The general route for solar energy to fuel conversion. (Copy from Royal Society of Chemistry).....	1
Fig 1.2. Photoelectrochemical cell design for water splitting [8]......	2
Fig 1.3. The valence band and conduction band of some semiconductor compounds [2]. .....	3
Fig 2.1. Pressure-Temperature diagram of pure water (molecular thermodynamics of Complex Systems). .....	11
Fig 2.2. a) Rod-like morphology of titania. b) Rectangular nanocrystal of uniform shape. c) Superlattice with dimensions of the order of $\mu\text{m}$ . d) Polymers with a polydispersity in length [37]......	16
Fig 2.3. Growth mechanism of $\text{TiO}_2$ nano-pillar crystals [70]. .....	16
Fig 2.4. Proposed growth mechanism for layered nanostructured $\text{TiO}_2$ .....	17
Fig 2.5. Formation process of $\text{Na}_2\text{Ti}_2\text{O}_4(\text{OH})_2$ [76]......	18
Fig 2.6. Structure models of (a) $2 \times 2$ unit cells of $\text{H}_2\text{Ti}_3\text{O}_7$ on the [010] projection and (b) a layer of $\text{H}_2\text{Ti}_3\text{O}_7$ on the (100) plane from which the nanotube is constructed. AA' and AA'' indicate the chiral vectors. Schematic diagrams show (c) the introduction of a displacement vector AA' when wrapping up a sheet to form a scroll-type nanotube and (d) the structure of the trititanate nanotube. The crystal orientations indicated are the orientations according to the $\text{H}_2\text{Ti}_3\text{O}_7$ layer [80]......	19
Fig 2.7. The crystal growth theory [81]. .....	19
Fig 2.8: Proposed mechanism of ZnO nanorods growth in water under hydrothermal condition [95]......	22
Fig 2.9. Schematic view of the growth mechanism of the ZnO nano form [108]. .....	23
Fig 2.10. Schematic illustration of growth mechanism of ZnO nanorods array [109]. .....	24
Fig 2.11. Electron transfer and Fermi level shift at a metal/semiconductor interface [117]. ..	25
Fig 2.12. Energy band for n-type semiconductor and the formation of space charge area [116]......	25
Fig 2.13. Band diagram when $V=V_{fb}$ , $V > V_{fb}$ and $V < V_{fb}$ when irradiated [116]. .....	26
Fig 2.14. Mechanism of charge transfer from SPR band under visible light [8]. .....	27
Fig 2.15. Electric field intensity at the interface of Au – $\text{TiO}_2$ calculated using FDTD.....	27
Fig 2.16. Schematic illustrating the scattering mechanism [8]......	28
Fig 3.1. Image of ZnO nanorods array on Zn foil a) using water b) using KOH after hydrothermal treatment.....	30
Fig 3.2. 3D schematic of hydrothermal treatment a) on Zn foil b) on ITO glass. ....	30
Fig 3.3. Image of dip coating process. ....	31
Fig 3.4. a) Au sputter VG Microtech SC500 machine b) AJA Sputtering .....	31
Fig 3.5. Illustration of sputtering process .....	32
Fig 3.6. The schematic of fabrication process. ....	33
Fig 3.7. Picture of 5 samples after sputtering. ....	33
Fig 4.1. 3D schematic of hydrothermal reactor .....	34
Fig 4.2. The schematic of SEM working principle.....	35
Fig 4.3. Illustration of XRD working principle .....	36

Fig 4.4. Schematic of UV-vis machine and measurement for solid sample .....	37
Fig 4.5. Schematic of UV-vis measurement for liquid sample.....	37
Fig 4.6. Schematic of TEM working principle .....	38
Fig 4.7. Methylene blue degradation setup .....	39
Fig 4.8. POL setup for transient photoresponse measurement .....	40
Fig 5.1. Titania morphology from reaction with a) TMAH 5 wt.% b) TMAH 8.3 wt.% c) TMAH 25wt. % .....	41
Fig 5.2. SEM image of TiO <sub>2</sub> nanotube a) at 5 hours reaction time b) at 24 hours reaction time c) after doping with small amount of Si.....	42
Fig 5.3. SEM image of TiO <sub>2</sub> nanotubes using secondary electron mode a) 0.01 Si doping b) 0.3 Si doping. ....	43
Fig 5.4. High resolution SEM image of a) undoped TiO <sub>2</sub> nanotubes b) doped TiO <sub>2</sub> nanotubes .....	43
Fig 5.5. TEM image of titania nanotubes a) Individual tube b) Numerous tubes.....	44
Fig 5.6. Mapping profile of a) Titanium b) Silica and c) the SEM image of 0.1 Si doped sample. ....	45
Fig 5.7. EDS spectra of 0.1 silica doped sample. ....	45
Fig 5.8. XRD pattern of a) Standard anatase crystal b) TiO <sub>2</sub> nanotubes c) 0.1 Si doped TNTs d) 0.3 Si doped TNTs.....	46
Fig 5.9. UV-vis absorption spectra of titania nanoparticles and titania nanotubes with the amount of Si doping in range of 0.01-0.3. ....	47
Fig 5.10. Band gap energy of different doped silicon amount.....	48
Fig 5.11. Photodegradation of MB using undoped TNTs and doped TNTs.....	49
Fig 5.12. Different morphologies of nanorods on Zn foil using water .....	50
Fig 5.13. SEM image of a) Pure ZnO nanorods array on Zn foil b) ZnO nanorods array with SiO <sub>2</sub> thin layer on top.....	51
Fig 5.14. Uv-vis absorption spectra of ZnO nanorods with different SiO <sub>2</sub> thickness coating. 51	
Fig 5.15. Illustration of light trap structure of SiO <sub>2</sub> coated sample. ....	52
Fig 5.16. Methylene blue degradation under white light illumination of SiO <sub>2</sub> coated ZnO nanorods.....	52
Fig 5.17. The SEM image of a) pure ZnO nanorods b) ZnO nanorods with SiO <sub>2</sub> and Au on top c) Mapping profile of ZnO-Au-SiO <sub>2</sub> sample on single rod. ....	53
Fig 5.18. The EDS profiles of ZnO-Au-SiO <sub>2</sub> sample. ....	54
Fig 5.19. UV-VIS absorption spectra of a) 5 pure ZnO nanorods arrays b) after coating with different configurations.....	55
Fig 5.20. I-V curves of the samples under white light illumination .....	55
Fig 5.21. Transient photocurrent of the samples at 0.5V biasing under white light illumination.....	56
Fig 5.22. The transient photoresponse of ZnO-Au-SiO <sub>2</sub> sample at 0.3, 0.5, 0.7 V bias.....	56
Fig 5.23. Band diagram of ZnO-Au sample .....	58
Fig 5.24. Band diagram of ZnO-SiO <sub>2</sub> -Au sample.....	58
Fig 5.25. Band diagram of ZnO-Au-SiO <sub>2</sub> sample.....	59
Fig 5.26. The photoresponse time of five samples in term of decaying and rising time .....	60

## LIST OF TABLES

Table 2.1 Summarization of synthesis conditions for Silica modifying TiO <sub>2</sub> .....	11
Table 3.1 SiO <sub>2</sub> Sputtering condition .....	33
Table 3.2 Au Sputtering condition.....	33
Table 5.1 The composition of Si doped TiO <sub>2</sub> samples .....	44
Table 5.2 XRD results of doped and undoped samples .....	47
Table 5.3 Band gap of the calcined samples at 450°C.....	48

## ACRONYMS

VB	Valence band
CB	Conduction Band
EDX	Energy dispersive X-ray
ITO	Indium tin oxide
NHE	Normal hydrogen electrode
PEC	Photoelectrochemical
SPR	Surface plasmon resonant
SEM	Scanning electron microscopy
TNTs	Titanium dioxide nanotubes
TEM	Transmission electron microscope
MB	Methylene blue

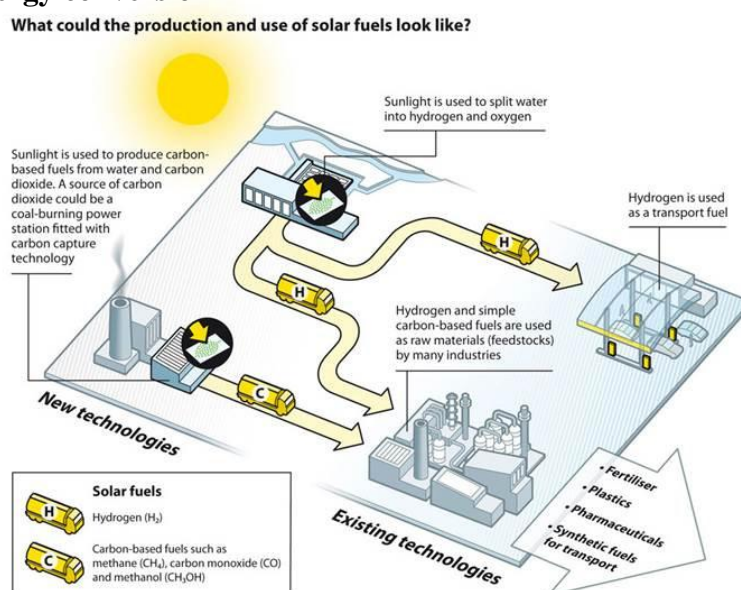
## CHAPTER 1. INTRODUCTION

In this chapter, renewable energy utilizing solar energy appears as the solution for the current energy issues. Semiconductors are considered as the most promising photocatalyst for solar energy to usable energy source conversion. Both basic large band gap semiconductors, TiO<sub>2</sub> and ZnO are introduced as the potential photocatalyst. The first look into this work is summarized in the end of this chapter.

### 1.1 The necessary of renewable energy

The fossil fuel is considered as the most important source of energy in the world. According to the US energy, the fossil fuel (natural gas, coal, petroleum and other liquids) accounts for 83 percent of the total primary energy consumption in 2013 [1]. High energy content, easy to transport, abundant amount stored in nature, the availability are the advantages of this kind of resources. This drives mankind on fossil fuel dependence [2]. However, the fossil fuel has its limitations. The current prediction indicates that it will run out of oil in 50 to 75 years, natural gas in twice of that of oil, coal in several hundred years. Hence, a mission has been set up to find out an appropriate renewable energy sources. Among the major renewable energy systems including photovoltaic (or solar cell), solar thermal, wind, biomass (plant and tree), hydroelectric, ocean, and geothermal, solar cell appears to be the competitive candidate in converting directly sun's energy into electricity with no moving part [3].

### 1.2 Chemical energy conversion



© Royal Society of Chemistry

Fig 1.1. The general route for solar energy to fuel conversion. (Copy from Royal Society of Chemistry)

There are three paths to solar fuels namely: Bio-routes, concentrated solar thermal and low temperature conversion using semiconductor [4]. The complexity, high cost and lack of robustness is the drawback of bio-routes. Besides, the operation at high temperature creating a number of issues in term of materials and stability, cost effectiveness and productivity are the disadvantages of the concentrated solar thermal path [5]. Thus, low temperature conversion using semiconductor will be approached. The keys for the success of artificial photocatalytic system are solar light absorption by the light harvesting agent, charge separation and electron transport, and effective utilization of the generated redox potential to drive desired chemical reactions [6]. Typically, solar energy is stored under the form of fuel gas or hydrogen gas by using photochemical reduction as illustrated in Fig 1.1.

### 1.2.1 Producing hydrogen gas from water

Photocatalyst hydrogen production system utilizes the sunlight energy to decompose water into hydrogen and oxygen. In the configuration of splitting of water experiment introduced by Fujishima and Honda [7], a working semiconductor electrode is deposited on a conductive substrate and connected through an external circuit to a counter electrode (typically Pt) as described in Fig 1.2. Base on the comparable band energy level with the oxidation potential of H<sub>2</sub>/H<sub>2</sub>O in Fig 1.3, a suitable semiconductor could be selected.

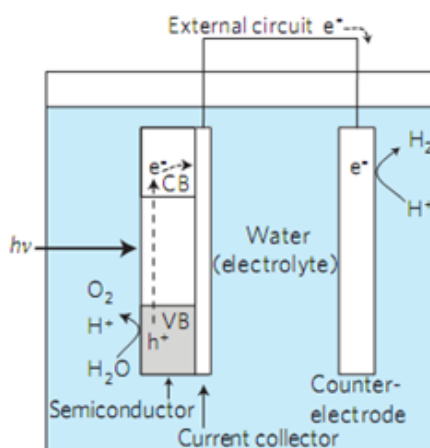


Fig 1.2. Photoelectrochemical cell design for water splitting [8].

A source of photon illuminates on this substrate to create excitation electron-hole pair. For n-type semiconductors, energetic holes will diffuse to the interface of semiconductor/liquid and involve in oxygen evolution half reaction and the energetic electrons will move to counter electrode where they take part in hydrogen evolution half reaction. The inverse order is presented for p-type semiconductors. According to Linic et al, beside robustness and affordability, an efficient photocatalyst has to (1) absorb photons across the UV-vis region of

the solar spectrum and transform them into electron-hole pairs; (2) allow effectively separation of electron-hole pairs and their transport to the liquid/semiconductor junction; (3) have appropriate surface electronic structure facilitating the half-reactions thermodynamically feasible; (4) own high catalytic activity [8].

### 1.2.2 Producing fuel gas from CO<sub>2</sub>

An ideal that mimicks the ability of plant and other photosynthetic organism in their use of CO<sub>2</sub> to make high energy compound has been investigated in last several years [5, 9]. Combining the availability of the sun's energy as well as solar cell system to convert the CO<sub>2</sub> into fuels which is possible for storage or transporting as needed is the major advantage of this route [2].

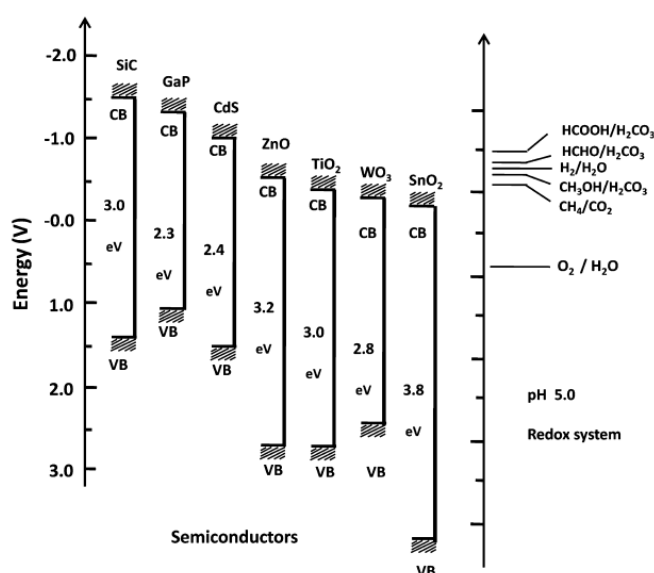
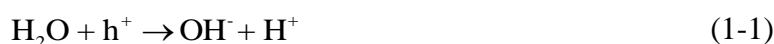


Fig 1.3. The valence band and conduction band of some semiconductor compounds [2].

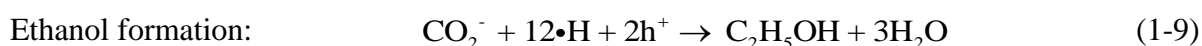
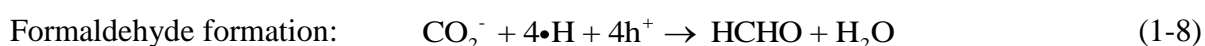
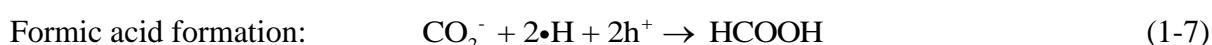
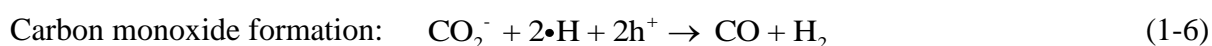
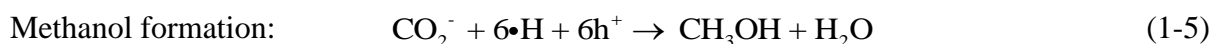
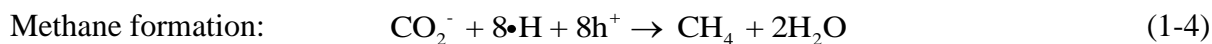
There are various semiconductor compounds used for CO<sub>2</sub> reduction such as SiC, GaP, CdS, ZnO, TiO<sub>2</sub>, WO<sub>3</sub>, SnO<sub>2</sub> which have different band gaps and band edges position as shown in [2]. This band gap and band edge position plays a crucial role in product formation. For instance, when WO<sub>3</sub> was used as catalyst, the absent of methyl alcohol further indicating the influence of band edge position on CO<sub>2</sub> reduction [2].

The mechanism of CO<sub>2</sub> reduction using water as a reductant is proposed by many published literature. When receiving the light, photoexcited electrons and holes are generated and trapped by suitable sites of catalyst to avoid recombination. The holes oxidize water and provide the protons for reduction. Then, electrons transfer from conduction band create two species of hydrogen radical ( $\cdot\text{H}$ ) and carbon dioxide anion radical ( $\cdot\text{CO}_2^-$ ) [5].





These species above are the raw sources for hydrocarbon formation reaction.



### 1.3 TiO<sub>2</sub> photocatalyst approaching and modifying

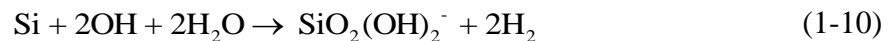
Among many photocatalytic candidates, TiO<sub>2</sub> is the most widely investigated and the most suitable for industrial scale applications in term of photoactivity efficiency, stability and cost [10]. However, TiO<sub>2</sub> only exhibits high reactivity and chemical stability under ultraviolet light ( $\lambda < 387$  nm) because of its wide band gap 3.3 eV in the anatase crystal phase [11]. As a result, various TiO<sub>2</sub> modifications have been carried out including: metal ion implanted (Cu, Co, Ni, Mn, Mo, Nb, Fe, Ru, Au, Ag, Pt ...) [12-14], TiO<sub>x</sub> photocatalyst reduced [15], non-metal doped-TiO<sub>2</sub> (N, S, C, B, P, I, F) [16, 17], or in composite with other low band gap compounds [18], TiO<sub>2</sub> sensitizing with dyes [19] and upconversion luminescence agent doped TiO<sub>2</sub>. These modifications aim to narrow the TiO<sub>2</sub> band gap or create impurity level [20] or oxygen vacancies [21] to have better photocatalytic performances.

It is known that TiO<sub>2</sub> has three polymorphs: anatase (tetragonal), brookite (orthorhombic) and rutile (tetragonal) while anatase phase titania exhibits the highest photoactivity than others [22]. Nevertheless, anatase and brookite phase are metastable generally formed at low temperature which will transform to thermodynamically stable rutile phase by heating or even by mechanical grinding [23]. Following this transformation is the rapid decrease in surface area and porosity which causes the negative effect on photocatalytic activity [24]. Among various additives, silica has been reported to have a significant stabilizing effect [24, 25] and photocatalytic activity enhancing [25, 26]. However, the effects of silica additive are quite

different depending on the doping process, the amount of additive [27]. The most widely studied method is sol-gel [25, 26, 28-30] and some others are thermal plasma [31], glycothermal [27], thin film coating [32], chemical vapor deposition to load TiO<sub>2</sub> onto silica gel [33] or sol-hydrothermal process [34-36]. Recently, some studies have reported that using ammonia water as hydrolysis catalyst could suppress the phase transformation and enhance the surface area [25].

Tetramethylammonium hydroxide has been recorded as a TiO<sub>2</sub> structure, size, shape controlling agent [37]. Nevertheless, the effects of basic template in photocatalytic activity of titania-silica hydrothermal pathway have been less investigated. Thus, one of the aims in this work is to carry out the characterization of silica doped-TiO<sub>2</sub> using TMAH as template in hydrothermal treatment which take advantage from waste in clean room.

In clean room, the lithography process often use TMAH as basic anisotropic etchant to etch away the silicon to create a desired structure on silicon wafer [38]. The waste after etching process is the mixture of TMAH and Silicon which exists as following [39]:



This is an excellent starting point for hydrothermal treatment.

The second approach is to utilize NaOH as template in hydrothermal treatment. This is conventional path way to organize tubular structure of titania [10].

#### **1.4 ZnO photocatalyst approaching and modifying**

Similar to TiO<sub>2</sub>, due to their attractive physical and chemical properties, ZnO nanostructures become the most promising metal oxides especially their 1D structure such as nanorods, nanowires, nanobelts and nanotubes [40]. The reasons for the great interest in 1-D nanostructure include the direct electron transport, high surface to volume ratio, fast reaction kinetic, high electronic conductance, simple preparation methods, and superior stability [41]. Also, compared to TiO<sub>2</sub>, ZnO is supposed to have higher efficiency in the photocatalytic performance in many case due to its higher quantum efficiency [42]. However, as a wide band gap semiconductor (3.37 eV), ZnO are only able to utilize 4% of the UV portion of solar energy [43]. Therefore, considerable attempts have been applied to extend the photoresponse of ZnO to visible light region. For photocatalytic applications, metal and non-metal doping are the most well-known groups. Metal dopants could create charge carrier traps, create donor or acceptor mid-gap level and increase the surface area and the crystal defects. Non-metal dopants could increase the defect formation and shift the valance band upward [43].

ZnO also has three polymorphs: wurtzite, rock-salt and zinc-blende crystal structures. Nevertheless, the thermodynamically stable phase at ambient condition is wurtzite structure. This structure will not be varied during the growth process such as hydrothermally growth of nanorods [44]. The drawback of this semiconductor are the low quantum efficiency and photocorrosion [45].

Thus, noble metals appear as the solution which promote the separation of photogenerated charges in photocatalyst and improve the photocatalytic stability [45]. In recent years, localized surface plasmon resonance created by doping with noble metal has become a hot topic [46]. This effect has been addressed to solar cells, surface-enhanced Raman spectra (SERS) and PEC water splitting with substantially enhanced performances [47]. Au is the most intensified investigated plasmonic metal which not only acts as effective surface passivation as well as electric-field amplification effect in UV region but also acts as electron injection source upon SPR excitation in visible region [48].

From many researches before, we know that the plasmon resonance frequency and intensity strongly depend on the dielectric of surrounding medium [49]. Enhancing the refractive index followed by the changing of dielectric circumstance would result in red-shift and intensified plasmon resonance and these are highly expected to improve the overall PEC performance [50]. Besides, this dielectric layer can enhance the stability of nanostructures under corrosive environment.

To clarify the dominant mechanism in different plasmonic configurations, a series of composite nanostructures based anodic ZnO nanorods backbones coated with Au, SiO<sub>2</sub> and both of them in different orders, i.e., ZnO-SiO<sub>2</sub>, ZnO-Au, ZnO-SiO<sub>2</sub>-Au, ZnO-Au-SiO<sub>2</sub> have been constructed.

## **1.5 Organization**

This thesis is organized in six chapters. Each chapter has its own specific content.

The potentials of large band gap semiconductors TiO<sub>2</sub> and ZnO as photocatalyst for sunlight to fuel conversion are highlighted in chapter 1. The possibilities of modified TiO<sub>2</sub> and ZnO for higher photocatalytic activity are also introduced. Particularly, silicon doped TiO<sub>2</sub> nanotubes (TNTs) powder and SiO<sub>2</sub>, Au coated ZnO nanorods array will be investigated in this work.

In Chapter 2, the first part presents the overview on how researchers dope silicon in various TiO<sub>2</sub> morphology. The effects of silica on the photocatalytic properties of titania are also discussed. All of possible formation mechanisms when using TMAH and NaOH as template are reviewed. The second part summarizes the methods for ZnO nanorods, followed by the

formation mechanism. The influences when incorporating with silicon and gold are proposed based on previous studies.

Chapter 3 performs in detail how to fabricate the silicon doped TNTs as well as SiO<sub>2</sub> and Au coated ZnO nanorods. Chapter 4 shows the principle of each equipment for catalyst characterization and measurements.

Chapter 5 is the most important section in this work with two main contents. Various investigations about the morphology of TNTs as well as its ability to capture light at longer wavelength after doping with silicon are discussed in the first content. In the second content, many explanations based theory and previous works are made to understand the outstanding photocurrent of ZnO-Au-SiO<sub>2</sub> configuration compared to others.

Chapter 6 highlights what this work has achieved and some more improvements in future to obtain better properties of these modified semiconductor photocatalysts.

## CHAPTER 2. LITERATURE SURVEY OF 1D TiO<sub>2</sub> AND ZnO NANOMATERIALS

The first part of this chapter presents various methods for silicon modified titania synthesis. The influences of silica on the properties of TiO<sub>2</sub> in this section point out the lack of discussion about the band gap changing in many researches before. Many structure formation mechanisms are proposed when using the TMAH and NaOH as template. In the second part, some well-known methods for producing 1D ZnO nanostructure are reviewed. The surface plasmon resonant and the effect of SiO<sub>2</sub> on plasmonic structure would be the potential combination for high photoelectrochemical (PEC) water splitting performance.

### 2.1 Literature review of silicon doped TiO<sub>2</sub> nanotubes

#### 2.1.1 Methods for producing Si-doped TiO<sub>2</sub>

##### 2.1.1.1 Sol-gel technique

The basic technique to produce silica-titania mixture is sol-gel. This method is the most widely used because of its ability in controlling the texture and surface properties of the mixed oxide [51]. Kyeong et al. [28] embedded silica onto titania particle using Titanium ethoxide (TEOT) and tetraethylorthosilicate (TEOS) as precursors of titania and silica. TEOS was introduced in the pre-mixed solution including hydrochloric acid and ethanol before TEOT because of its slow hydrolysis rate. The silica-titania particles were obtained after mixing for 24h, heating at 80°C for 5h, drying for 24h and calcining from 400-800°C. The final product had pure anatase phase with the highest photoactivity collected at 30-silica/titania calcined at 700°C.

Chao et al. [25] also prepared titania-silica mixed oxide by using ammonia water as hydrolysis catalyst. After slow dropping into beaker with anhydrous ethanol under stirring, the mixture was aged for 72h and calcined at the same temperature above. The obtained silica-titania mixed oxide had higher thermal stability, lower bulk defects, optimal Bronsted acidity and highest photoactivity at TiO<sub>2</sub>-9.1% mol SiO<sub>2</sub> because of sufficient active sites. An excellent activity in destruction of R-6G of mixed oxide SiO<sub>2</sub> and TiO<sub>2</sub> prepared by sol-gel route in nearly the same procedure above [52]. The resulting solution was stirred in ice bath, aged for 1 week and heated at 200°C for 12h in vacuum. Calleja et al. [29] prepared mesostructured TiO<sub>2</sub>-SiO<sub>2</sub> in 20h synthesis time using triblock copolymer P-123 as structure-directing agent. Then washing with ethanol and calcination at 300°C for 2h was carried out. The results show that silicon atoms were highly dispersed and homogeneity in TiO<sub>2</sub> framework. There are still

several works about doping silica on titania in approximately the same procedure such as co-doping aluminum and silicon on titania [53], high temperature stable mesoporous anatase TiO<sub>2</sub> [54], coating Si-doped TiO<sub>2</sub> on inorganic membrane [55], or on silicon wafer [32] or on soda-lime silica glass substrate by dip-coating technique [56] but they mostly relied on basic principle of sol-gel route.

Ying et al. [26] and Pitoniak [57] et al. synthesized SiO<sub>2</sub>-TiO<sub>2</sub> nanocomposite, a distinct structure, by sol-gel route without calcination. The final product was collected after heat treatment at 103 °C in 18h and 180°C in 6h. This composite material contains high surface area (~ 272 m<sup>2</sup>/g) nanostructured SiO<sub>2</sub> gel containing TiO<sub>2</sub> nanoparticles with high adsorptive capacity [57].

The morphology of titania also has significant effect on photocatalytic activity. Bao et al. [30] doped silica on mesoporous TiO<sub>2</sub> continuous fibers by combining sol-gel and then centrifugal spinning. The addition of silica enhanced the length of titanium fiber. With appropriate amount of silica, it could improve the surface texture, thermal stability and crystal stability.

#### **2.1.1.2 Thermal plasma and oxide bath technique**

According to thermal plasma technique, Si-doped TiO<sub>2</sub> was synthesized from titanium tetrachloride and silicon tetrachloride in plasma reactor. The precursors were injected into plasma region by Ar carrier gas and the setting up pressure range was 700 to 760 Torr in 10 min [31]. With the appropriate amount of SiO<sub>2</sub> doping (< 2%), the photocatalytic activity of modified TiO<sub>2</sub> is significantly improved [31].

Oxide bath is a simple technique for preparation of Si-doped TiO<sub>2</sub> thin film by thermal treatment of titanium metal plate embedded in silicon dioxide powder [58]. In this method, clean Ti sheets were partly embedded in SiO<sub>2</sub> powder in porcelain crucible following by thermal treatment in muffle furnace at atmospheric pressure in air at various times and temperature (400-550°C) [58]. The result implies that the concentration of Silica in thin film was proportional to thermal treatment time and temperature. By this treatment, the response in visible light region, the negative flat band and the density of carrier were enhanced [58]. On the other hand, these two methods require special equipment as well as high operation cost.

#### **2.1.1.3 Chemical vapor deposition technique**

In this field of technique, Ding et al. [59] chose tetra-isopropoxide to be a precursor because of its evaporative. TTIP was introduced into chemical vapor deposition (CVD) reactor by the carrier gas under vacuum after silica gel loaded. The reaction took place at 300°C then the

sample was calcined at 500°C for 3h. CVD method offered uniform crystallite size and strong adhesion of TiO<sub>2</sub> particle on silica gel but the best activity is only half of that of the commercial one [59].

CVD method was also used to introduce silicon atoms into the TiO<sub>2</sub> nanotube array which was synthesized by anodization method [60] or into titanium sheet [61]. TEOS was admitted into CVD reactor by Ar gas at 500°C for 15 min. The sample was then annealed at 650°C for 30 min [60]. This method gives highly ordered Si-doped TiO<sub>2</sub> nanotubes array which performs higher photo-response in UV spectrum, higher photocurrent density and photo-conversion efficiency than those un-doped [60].

#### **2.1.1.4 Impregnation, precipitation, co-precipitation technique**

Long time ago, in 1989, precipitation method was carried out to form titania/silica [62]. Aqueous ammonia was used as PH controlling agent in mixture of titanyl sulfate, silica sol in sulfuric acid until pH was about 9.5. The precipitation was washed, dried overnight and calcined at 550°C for 6h in air [62]. However, Khouw et al. [63] mentioned that co-precipitation method for preparing TiO<sub>2</sub>-SiO<sub>2</sub> mixed oxide showed bad performance on oxidation reaction.

Along with co-precipitation, impregnation is the basic method for preparing catalyst for almost processes. Silica was also impregnated with a toluene solution of diisopropoxy-dipivaroylmethanato-titanium (IV) (Ti(DPM)<sub>2</sub>(O-iPr)<sub>2</sub>) for 2h under reflux condition. The filtrate was dried and calcined for 5h at 500°C [64]. These techniques are not preferable because of its low efficient.

#### **2.1.1.5 Hydrothermal technique**

As an environment friendly technology, hydrothermal synthesis takes place in a closed system under controlled temperature and pressure [65]. Hydrothermal is also considered as a direct synthesis of a well-crystallized titania method which can improve the stability of titania [27]. Hirano et al. [23] synthesized TiO<sub>2</sub>/SiO<sub>2</sub> composite nanoparticles with highly stable crystallite at 1300°C. TiOSO<sub>4</sub> and tetraethyl orthosilicate were injected in Teflon container of a stainless steel vessel which was heated at 200°C for 24h with rotation at 1.5 rpm [23]. Some studies modify the step before injecting into the autoclave to obtain different characteristic [27, 34, 36]. Iwamoto et al. [27] added 1,4-butanediol in mixture of TIP and TEOS and this mixture was placed in an autoclave for heating at 300°C for 2h. Yan et al. [34] used octadecylamine as template for hydrothermal condensation of (Ti(OBu)<sub>4</sub>) and (TEOS). A white precipitate was transferred to an autoclave and aging for 24h at room temperature, then heated at 353K for 1 day. This modification gives high specific area, photocatalytic activity and the optimum Silica

content is in range 25-40% [34]. Recently, Jin et al [36] prepared silica-doped TiO<sub>2</sub> in ethanol solvent in stainless steel autoclave. The hydrothermal treatment was carried out at 473 K for 12h. In addition, hydrothermal treatment is economic, high efficient and the most feasible method for creating 1D nanostructure.

During the hydrothermal treatment, temperature directly control the pressure inside the chamber. Besides, filling factor is also considered in this method because the level of it is equivalent with the pressure inside the reactor. This relation is shown in Fig 2.1.

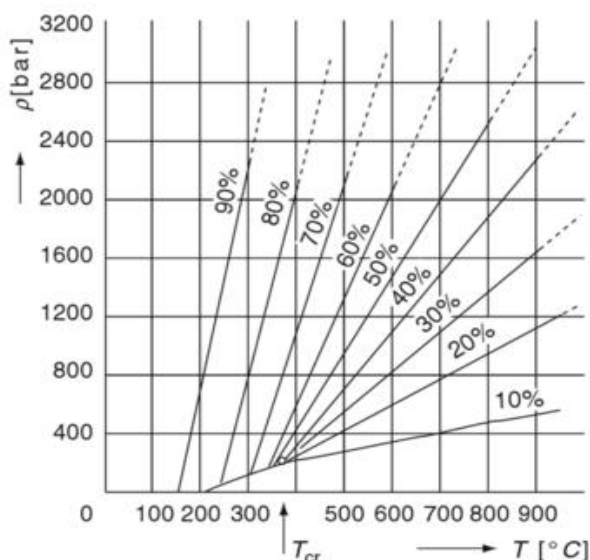


Fig 2.1. Pressure-Temperature diagram of pure water (molecular thermodynamics of Complex Systems).

All techniques are summarized in Table 2.1.

Table 2.1 Summarization of synthesis conditions for Silica modifying TiO<sub>2</sub>

TiO <sub>2</sub> precursor	Si precursor	Method	Condition	Final geometry	References
Titanium sheets	Tetraethylort hosilicate (TEOS)	Anodization.	Ti sheet: anode, Pt foil: cathode	Si doped	[60]
		Doping by CVD	Electrolyte NH <sub>4</sub> F + (NH <sub>4</sub> ) <sub>2</sub> SO <sub>4</sub> , PH 5.5-6.5 CVD took place at 500°C for 15 min, annealing at 650°C for 30 min	TiO <sub>2</sub> nanotubes	
Degussa P25 TiO <sub>2</sub>	TEOS	Sol-gel	Hydrolysis in ethanol + HNO <sub>3</sub> + HF, after gelation, the sol was aged for 2 days at room temperature, then 2 day at 65°C. Heat treatment at 103 and 180°C.	TiO <sub>2</sub> /SiO <sub>2</sub> composite nanopartic les	[26, 57]

TiOSO <sub>4</sub>	TEOS	Hydrothermal	Heating at 200°C for 24h with rotation of 1.5 rpm in an autoclave.	TiO <sub>2</sub> /SiO <sub>2</sub> composite nanoparticles	[23]
Titanium ethoxide	TEOS	Sol-gel	Mixture including HCl and ethanol with precursor in 24h was heated at 80°C for 5h. drying and calcining between 400 and 800°C	Nano phase silica-embedded titania particle	[28]
Titanium tetrabutoxide	TEOS	Base hydrolysis	Using ammonia, dropping under stirring condition, aged for 72h followed by calcination from 400-800°C for 2h	Titania-silica mixed oxides	[25]
TBOT	TEOS	Sol-gel	Hydrolysis in ethanol and HCl at room temperature under stirring condition. Ceramic membrane was immersed in the sol for coating.	Si-doped TiO <sub>2</sub> coating on inorganic membrane	[55]
Titanium oxysulphate	TEOS	Sol-gel	Mixed at 70°C and calcined at 500, 600, 700, 800, 900, 1000°C	Silica doped anatase titania	[29]
TBOT	TEOS	Centrifugal spinning combined sol-gel	Titania-silica sol was injected into centrifugal tube at speed 6500 rpm/min	Long Si-doped mesoporous TiO <sub>2</sub> fibers	[30]
Titanium tetrachloride	Silicon tetrachloride	Thermal plasma	Ar carrier gas, pressure from 700-760 Torr	Si doped TiO <sub>2</sub> powder	[31]
TIP	TEOS	Glycothermal	Autoclave 300°C for 2h with 1,4-butanediol. Then calcined at 400°C	Silica-modified titania anatase phase	[27]
Titanium sheets	Silicon dioxide powder	Thermal treatment	Atmospheric pressure, sample was heated various time and temperature (400-550)	Silicon doped	[58]

				TiO <sub>2</sub> thin film.	
Titanium sheets	TEOS	Chemical vapor deposition	The CVD reaction took place at 220°C. Substrate was then anneal in air at 550°C for 1h	Si-doped TiO <sub>2</sub> nanofilm	[61]
Rectangular piece of Ti	Na <sub>2</sub> SiF <sub>6</sub>	Anodization	Current density: 2.5 mA cm <sup>-2</sup> , 20V in 30min, calcined at 400°C	Si doped TiO <sub>2</sub> nanotubes film.	
Tetrabutyl titanate	TEOS	Hydrothermal condensation	Age for 24h, heat 353K in 1 day.	Si-doped TiO <sub>2</sub> mesoporous	[34]
Tetrabutyl titanate	Ethyl silicate	Hydrothermal process	473K in 12h, separated by centrifugation, using ethanol	Si-doped TiO <sub>2</sub>	[36]
Tetraiso-propyl orthotitanate	TEOS	Sol-gel	Hydrolysis in anhydrous 2-propanol and HCl. Stirring in ice bath, aging in 1 week, heating to 200°C under vacuum for 12h	Mixed oxide SiO <sub>2</sub> and TiO <sub>2</sub>	[52]
TBOT	TEOS	Sol-gel	Using Glacial acetic acid as hydrolysis inhibitors. The colorless sol was heated at 100°C for 24h	Si-Al co-doping of titania nanoparticles.	[53]
Tinanyl oxysulphate	TEOS	Sol-gel	Silica sol is added into titania sol, stirring for 2h, placing in oven at 70°C. The dried gel was calcinated at 500-1000°C	Silica-titania mixed oxide	[54]
TiO <sub>2</sub> dispersed in isopropanol	TEOS	Sol-gel	Hydrolysis in ethanol and HCl. Glass substrate was immersed in sol to form the thin film layer. The film was then aged for 10h, following by drying at 90°C for 14h and heating at 350°C for 1h.	TiO <sub>2</sub> nanoparticles doped SiO <sub>2</sub> film with ordered mesopore channels.	[56]

TTIP	Silica gel	Chemical vapor deposition	CVD reaction took place at 300°C. Sample was then calcined at 500°C for 3h.	Silica gel supported TiO <sub>2</sub>	[59]
Tinanyl sulfate	Silica sol	Precipitation	NH <sub>3</sub> was used to precipitate sample. The mixture was then washed, dried and calcined at 550°C for 6h in air.	Titania/Silica	[62]
-	-	Co-precipitation	The precipitate was dried in air at 200°C for 24h.	TiO <sub>2</sub> -SiO <sub>2</sub> oxide	[63]
(Ti(DMP) <sub>2</sub> (O-iPr) <sub>2</sub> )	Silicon tetraethoxide	Impregnation	The filtrate was dried and calcined for 5h at 500°C.	D-TiO <sub>2</sub> /SiO <sub>2</sub>	[64]

### 2.1.2 The influences of silica to TiO<sub>2</sub> photochemical properties

Most of papers about silica incorporated TiO<sub>2</sub> proved the positive effects on photoactivity. Kyeong et al. confirmed that addition of silica suppresses the phase transformation of titania from anatase to rutile which will increase the thermal stability of this catalyst [28]. He also stated that higher crystallinity leads to higher photoactivity and the optimal composition of Silica is 30% because of high surface area.

Chao et al. also observed that the addition of silica inhibited the growth of crystalline size and suppress the phase transformation through XRD and TGA analysis. FT-IR spectra indicate the Ti-O-Si linkages at 948 cm<sup>-1</sup> which is the evident of the interaction between titania and silica [25]. This will enhance surface properties and photocatalytic activity.

A controversy involving the addition of silica narrows or extends the band gap of titania which significantly relates to the atomic structure of silica-titania mixed oxide. FT-IR results again imply that Ti atoms transform from octahedral environment to tetrahedral environment. This transformation forms Bronsted acidity and it reaches maximum at 10% mol of silica. Moreover, the experiment confirms the significant blue-shifted of silica-doped titania due to well-known quantum size effect. On the other hand, the simulation and some other researchers claimed the red-shift.

#### 2.1.2.1 Band gap extension

Calleja et al. indicated that the interruption of silicon to TiO<sub>2</sub> structure leads to increase the band gap ( $E_G$ ). This interruption also hinders the phase segregation and delays the crystallization over the calcination process [29].

Nan Bao et al. stated that a proper amount of silica might be dissolved in titania matrix which suppresses the phase transformation [30]. The higher calcination temperature, the higher

crystallization and formation of larger crystallites. The interaction between titania and silica can be proved by the present of Ti-O-Si linkages. The amorphous silica forms a Si-O-Ti-O-Si network which associated with the generation of Bronsted acidity. Blue shift is observed due to doping which is attributed to a combined effect of the quantum size and the interface interactions. The recombination rate is reduced because of this effect. A combination between anatase phase and rutile phase produce better photoactivity.

Periyat [54] claimed that a suitable amount of silica can effectively suppress the phase transformation. He also claims that the entering of silica atoms into the matrix increase the defects in titania matrix thus increases the surface area. The increment in band gap energy results in lowering the energy of valance band and an increase in the conduction band edge.

#### **2.1.2.2 Band gap narrowing**

However, according to first-principles calculation for geometrical structures and electronic properties of Si-doped TiO<sub>2</sub>, the substitution of Ti by Si results in band-gap narrowing about 0.25 eV which is responsible for visible light optical absorption [66]. But high level Si doped anatase TiO<sub>2</sub> is limited because of high formation energy required [67]. There are also some experimental works which are in good agreement with the simulation results. Oh et al. who investigated thermal plasma method clarified that the exceed amount of Si-dopant (>2%) reduces Ti atoms of the surface of catalyst. Sun et al. [58] observed an enhancement in photochemical respond of the Si-doped TiO<sub>2</sub> under visible light illumination. Recently, Asiah et al. [68] have indicated the red-shift of the absorption spectrum when doped Si onto the TiO<sub>2</sub> nanowire using hydrothermal method.

In conclusion, according to simulation and the nature band of of silicon (1.1 eV), truly doping silicon into titania crystal structure, the band gap should be narrowed.

#### **2.1.3 Proposed mechanism by using TMAH as template in hydrothermal pathway**

From the beginning of the 21<sup>st</sup> century, researchers have used TMAH as capping agent for controlling nanocrystal structure, size, shape and organization [37, 69]. By varying the concentration of TMAH and the synthesis condition, Abdelkrim et al. [37] obtained different morphology of titania as shown below in Fig 2.2.

The apparent preference for this variety is that the interaction between [101] surfaces and Me<sub>4</sub>N<sup>+</sup> accounted for the differential velocity in the [101] and [001] directions [37]. The directing ability of TMAH was also reported in the revealing cubic-like and truncated tetragonal nanocrystals [69].

In many systems especially hydrothermal system, TMAH plays a crucial role as a directing agent. Dong et al. prepared controllable morphology, size and orientation of TiO<sub>2</sub> nano-pillar arrays by varying the TMAH concentration and hydrothermal temperature [70] which is illustrated in Fig 2.3. TMAH was also used as mineralizer (pH-adjusting agent) for pure, stable lead titanate (PbTiO<sub>3</sub>) particles synthesis [71].

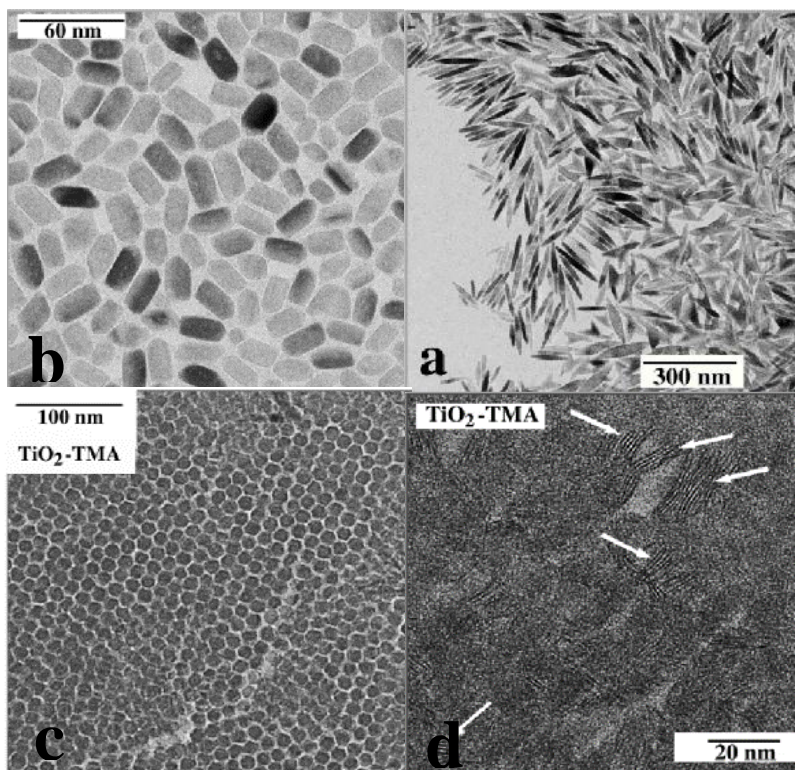


Fig 2.2. a) Rod-like morphology of titania. b) Rectangular nanocrystal of uniform shape. c) Superlattice with dimensions of the order of  $\mu\text{m}$ . d) Polymers with a polydispersity in length [37].

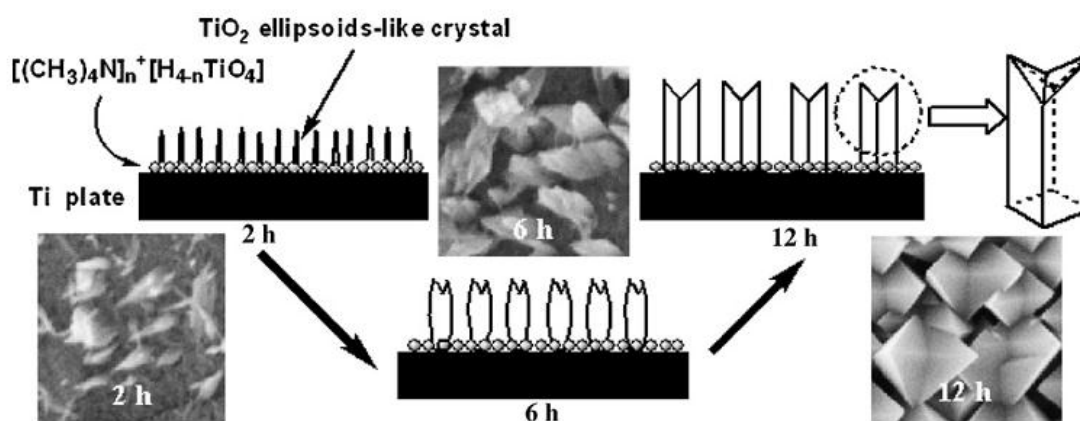


Fig 2.3. Growth mechanism of TiO<sub>2</sub> nano-pillar crystals [70].

Ooi et al. is one of the first researchers who investigated the intercalating ability of TMAH [72]. The motivation for the intercalation is the distinct proton activity between the supernatant solution and the interlayer [72]. Gao et al. [73] investigated continuously on the intercalating ability of TMAH on preparing of nanometer-sized manganese oxides in a year later. TMAH intercalated into the organic layer which led to larger distance between layers thus inducing layer easier to break into smaller pieces [73]. Recently, layered nanostructured TiO<sub>2</sub> has been synthesized by hydrothermal method using TMAH [74]. The layered nanostructured TiO<sub>2</sub> is supposed to be form in the initial stage of the hydrothermal treatment where TMAH acts as capping agent to TiO<sub>2</sub> precursor [74]. The intercalating mechanism is shown in Fig 2.4.

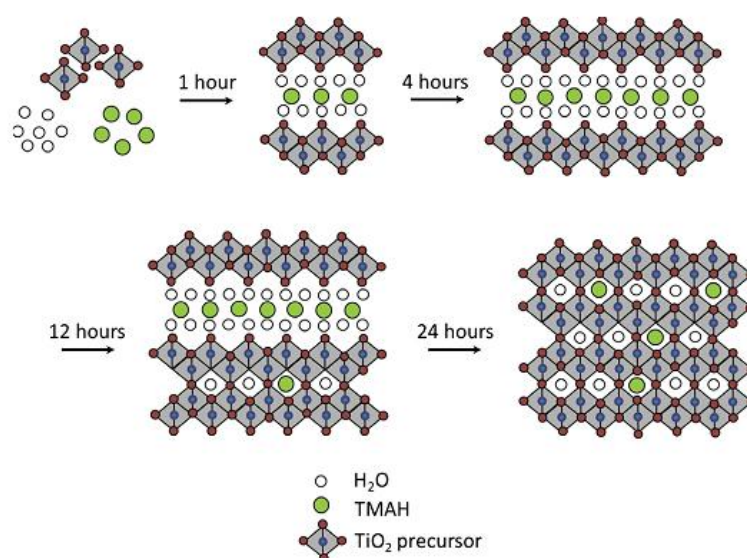


Fig 2.4. Proposed growth mechanism for layered nanostructured TiO<sub>2</sub> [74].

As discussed, TMAH has ability to create sheet nanostructure. It's worth to try the possibility of tube formation from these nanosheets.

#### 2.1.4 Tubular formation mechanism using NaOH as template in hydrothermal pathway

In the end of 20<sup>th</sup> century, simply via hydrothermal treatment of crystalline titanium dioxide nanoparticle with highly concentrated sodium hydroxide, TiO<sub>2</sub> nanotube with small diameter are created [65, 75]. This is a cost-effectiveness, low energy consumption, mild reaction condition and simple equipment requirement method [75]. Compared to the other forms of titanium dioxide, titania nanotubes perform better physical and chemical properties in photocatalysis [65]. Thus, one of the main purposes of this work is to produce the titania nanotubes. For better controllable morphology, the comprehensive knowledge of the mechanisms of titania nanotubes formation were proposed in various manners [10].

### 2.1.4.1 Acid washing mechanism

Yang et al. [76] proposed a mechanism that the Ti-O bonds within the TiO<sub>6</sub> unit seem to be divided under the concentrated NaOH which results in irregular swelling. The linear fragments are then linked to each other by <sup>-</sup>O-Na<sup>+</sup>-O<sup>-</sup> bond. After the replacement of Na<sup>+</sup> by H<sup>+</sup> through acid washing, nanotubes are obtained through covalent bonding as demonstrated in Fig 2.5.

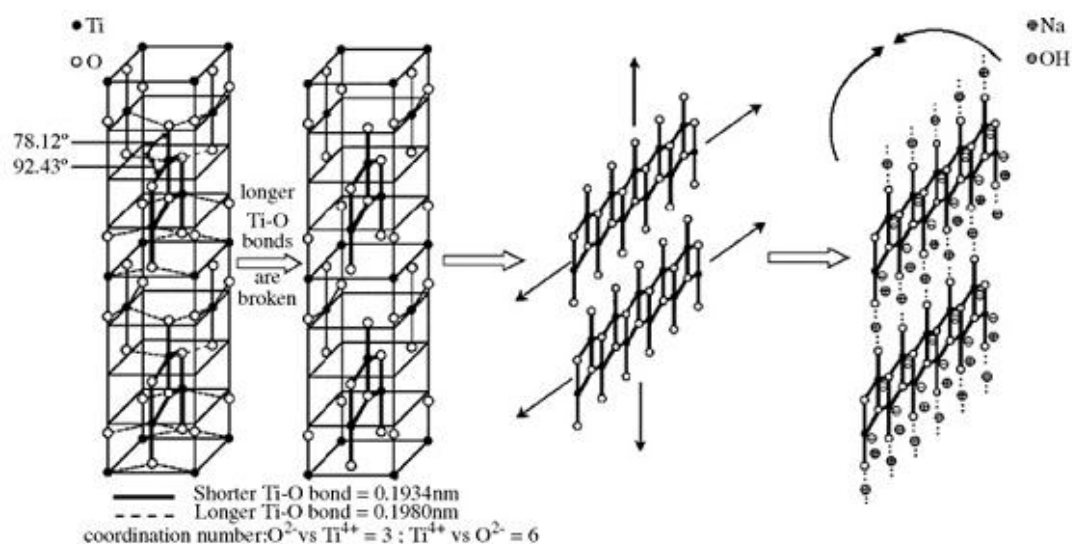


Fig 2.5. Formation process of Na<sub>2</sub>Ti<sub>2</sub>O<sub>4</sub>(OH)<sub>2</sub> [76].

This mechanism is in good agreement with the mechanism proposed by Kasuga et al. [77] that washing with acid eliminates electrostatic repulsion and scrolls the lamellar sheets into tubes during the hydrothermal process. The same idea offered by Tsai et al. [78] that hydrothermal condition breaks Ti-O-Ti bonds into Ti-O-Na and Ti-OH bonds. The sheets are formed by the rearrangement of Na<sup>+</sup> and H<sup>+</sup> which then scroll into tube by the variation of the surface charge caused by ion exchange of Na<sup>+</sup> and H<sup>+</sup>.

### 2.1.4.2 Peeling-scrolling mechanism

In conflict with the idea above, Peng et al. [79] indicated that trititanate (Ti<sub>3</sub>O<sub>7</sub>)<sup>2-</sup> sheets are established within the intermediate phase during the reaction of NaOH and TiO<sub>2</sub>. The growing of this nanosheets have tendency to curl leading to the formation of nanotubes. The driving force for this curling is the hydrogen-deficiency on the surface of (Ti<sub>3</sub>O<sub>7</sub>)<sup>2-</sup> (surface tension) [79]. Most of researchers agreed that hydrothermal is a crucial step for the formation of TNTs meanwhile washing with acid only produces protonated titanates and the formation mechanism involves in four stages: (1) dissolution of TiO<sub>2</sub> precursor and breaking Ti-O-Ti in alkaline solution, (2) growth of layered nanosheets of sodium titanates, (3) exfoliation of

nanosheets and (4) growing of nanosheets with the tendency of curling to the formation of nanotubes [10]. A typical example of trititanate tubes formation is demonstrated in Fig 2.6.

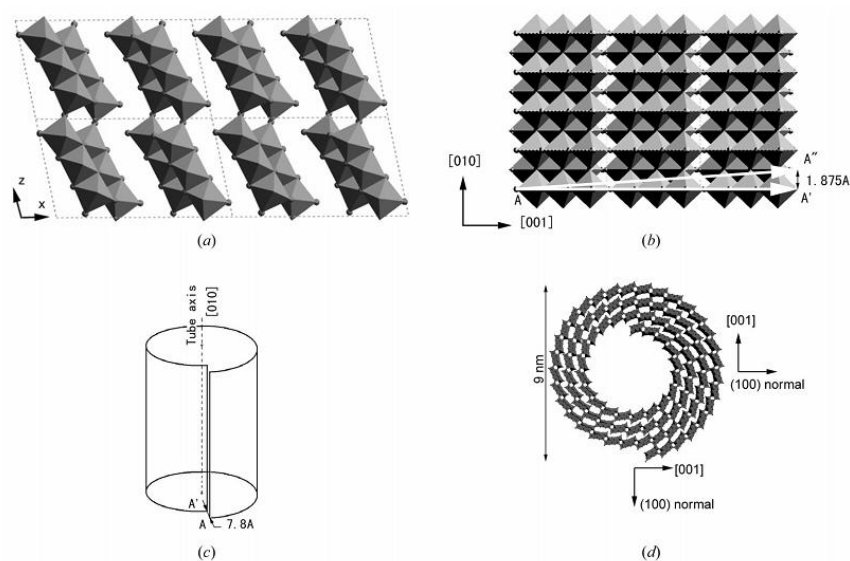


Fig 2.6. Structure models of (a) 2 x 2 unit cells of H<sub>2</sub>Ti<sub>3</sub>O<sub>7</sub> on the [010] projection and (b) a layer of H<sub>2</sub>Ti<sub>3</sub>O<sub>7</sub> on the (100) plane from which the nanotube is constructed. AA' and AA'' indicate the chiral vectors. Schematic diagrams show (c) the introduction of a displacement vector AA' when wrapping up a sheet to form a scroll-type nanotube and (d) the structure of the trititanate nanotube. The crystal orientations indicated are the orientations according to the H<sub>2</sub>Ti<sub>3</sub>O<sub>7</sub> layer [80].

### 2.1.4.3 Seeding-oriented crystal growth mechanism

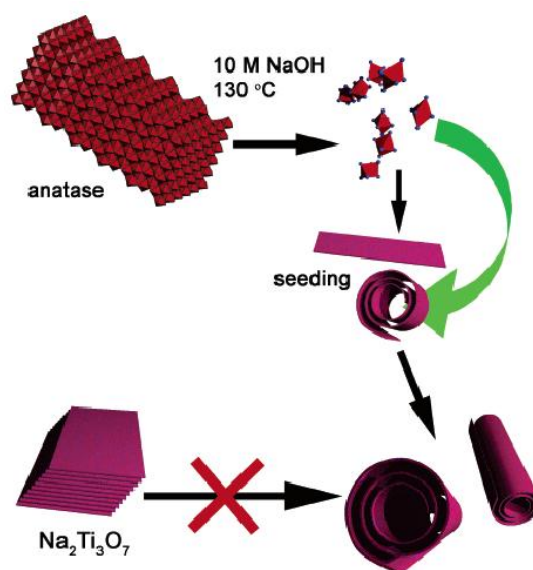


Fig 2.7. The crystal growth theory [81].

Kukovecz et al. [81] observed that when subjected directly as-synthesis Na<sub>2</sub>Ti<sub>3</sub>O<sub>7</sub> lamellar structure (intermediate phase), the trititanate sheets were only cut into block of stripes but did not roll up into nanotubes. The presented trititanate sheet rollup theory cannot explain their

phenomenon. With further investigation, they suggested that rollup theory is in effect only when the extreme conditions at the surface of nanoparticles are generated by local concentration fluctuations. Then a small amount of material is removed from the surface of anatase crystalline. This material recrystallizes into a trititanate sheets resulting in nanoloop of single-spiral, multiple-spiral or onion-like cross-section. The rest of material is transformed into nanotube by oriented crystal growth which is supplied with TiO<sub>6</sub> building blocks. The as-prepared Na<sub>2</sub>Ti<sub>3</sub>O<sub>7</sub> is the most stable phase under hydrothermal reaction condition which cannot be transformed further by NaOH. Thus, it does not roll up into nanotubes. Under mixed autoclave, fewer and longer nanotubes are formed which can be well explained by this crystal growth theory as shown in Fig 2.7. Until now, no researcher confirms the major mechanism in nanotubes formation. Most of them agrees with peeling-scrolling mechanism.

## **2.2 Literature review of silicon dioxide and gold on ZnO nanorods array composite nanostructures**

### **2.2.1 Methods for producing ZnO nanorods**

One-dimensional (1D) ZnO nanostructures have been investigated by a wide range of synthesis techniques.

#### **2.2.1.1 Physical vapor deposition**

Pan et al. synthesized nanobelts of ZnO by thermal evaporation at 1400°C for 2h in an alumina tube [82]. The nanobelts product performs well defined geometry and perfect crystallinity which could be doped with different elements and used for fabricating nanosize sensors. Huang et al. deposited ZnO nanowires on Au coated silicon substrate using vacuum thermal evaporator [83]. The diameter of nanowires could be control by varying the Au layer thickness. Yao et al. developed various nanostructures base on thermal evaporation process of ZnO without the presence of a catalyst [84]. Starting from the source of ZnO and graphite, the formation of distinct geometries depend on the temperature at open end of quartz tube. The drawback of this method is the consuming of large energy for evaporation.

#### **2.2.1.2 Metal-organic chemical vapor deposition**

Typically in this method, a metal organic substance is used as precursor and the growth take place at high temperature. Park et al. grew ZnO nanoneedles on Silicon substrate using low pressure metal-organic chemical vapor deposition (MOCVD) system with dimethyl zinc and oxygen as reactants [85]. This nanoneedles array exhibits high crystallinity and excellent photoluminescent characteristic. In another work, Park also synthesized ZnO nanorods array with almost the same method but the different is the thin buffer layer is formed before the

growth of ZnO nanorods [86]. The advantages of this method include the feasibility of large area growth as well as simple, accurate doping and thickness control.

#### **2.2.1.3 Pulsed laser deposition**

Sun et al. obtained ZnO nanorod arrays using Pulsed laser deposition (PLD) method which are single synthesis process without doping, or use of catalyst or the need of any prior templating [87]. This technique bombards the ceramic ZnO target by excimer laser and deposit ZnO on substrate. The nanorods array synthesized by this way is suitable for application in opto electronic nanodevice [87]. Hong et al. utilized PLD to deposit ZnO thin film and grew ZnO nanowires on top of this thin film using vapor-solid-solid growth method [88]. The texture of ZnO film can be controlled at room temperature via the control of the energy of the deposited atoms.

#### **2.2.1.4 Electrospinning**

In this method, the precursor solution is contained in a stainless steel needle under pumping condition. A cathode electrode is placed under the needle tip. An electric field is applied to accelerate the precursor toward the cathode accompanied with partial solvent evaporation. Lin et al. produced aluminum-doped zinc oxide (AZO) nanofibers using electrospinning process [89]. This AZO perform better field emission and conductance characteristics. Sui et al. fabricated polyvinyl alcohol/ZnO hybrid nanofibers with diameter about 300nm which showed strong white emission with three band [90].

#### **2.2.1.5 Wet chemical method**

Wet chemical is the most promising method which has been investigated by many researchers until now [91]. In this route, hydrothermal treatment appears as a competitive candidate because of low price and high efficiency. Zhang et al. synthesized tubular ZnO with approximately 450 nm width and 4  $\mu$ m length by simple solution using ethanol solvent [92]. However, the nanopowder prepared by this method is only 20%. With template free hydrothermal treatment, Wang et al. can easily control the ZnO nanotubes powder synthesis process with high repeatability [93]. Recently, Nadia et al. have prepared ZnO nanotubes powder with wurtzite structure from zinc nitrate, urea and KOH for the first time [94]. As mention before, the nanopowder is hard to handle and recover after using. Thus, researchers force the interested into nanostructure array. With only water [95] or NH<sub>3</sub> [96] or Zn(NO<sub>3</sub>)<sub>2</sub> in KOH [97], many researchers deposited ZnO nanorods, nanoneedles directly on Zn foil by hydrothermal treatment. Growing directly on Zn substrate is simpler than other substrates which needs at least two steps, seed layer deposition and growth process. This however the

most common procedure for growing nanostructure of ZnO [98]. Amine compounds are the main reagent for direct grow in the c-direction of this two steps method [99, 100].

Anodization which is the most common method for producing TiO<sub>2</sub> nanotubes array, is also utilized to prepared the ZnO nanorods [101].

There was also some procedures which lasted for a long time 1-12 days [102], 0-60 days [103] at room temp. Nevertheless, these methods are not applicable to industry due to time consuming.

### 2.2.1.6 Others

HeO et al. utilized catalysis-driven molecular-beam epitaxy (MBE) to create the ZnO nanorods [104]. This method is carried out in vacuum chamber with ozone/oxygen as oxidizing source, Zn metal as cation flux source. With only magnetron sputtering, Chiou et al. could grow ZnO nanowires under controllable conditions [105]. He stated that to obtain the single crystal whiskers the presence of electroless plated copper is necessary. Xu et al. prepared ZnO nanorods using flux at very high temperature [106]. These prepared nanorods are uniformly distributed and single crystalline. Wu et al. deposited ZnO films from evaporation the precursors then etched these products with hydrogen stream to form ZnO nanorods [107].

## 2.2.2 The hydrothermal growth mechanism of ZnO nanorods

### 2.2.2.1 In water medium

From the point of chemistry view, water has the ability to oxidize Zn metal. Under hydrothermal condition, water interacts with Zn foil as following reaction:



This two reactions take place at distinct regions over the surface of Zn foil which created self-motivated cathode and anode system. Zn is oxidized at the anode into Zn<sup>2+</sup> with 2 electron left behind and ZnO is deposited at the cathode forming the ZnO nanorods as presented in Fig 2.8 [95].

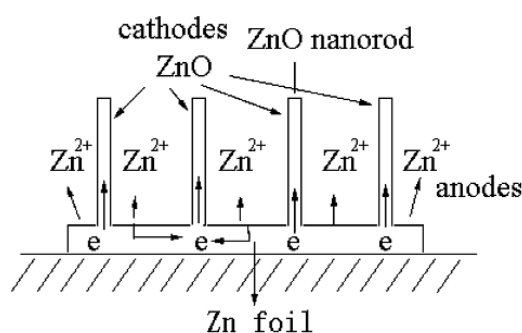
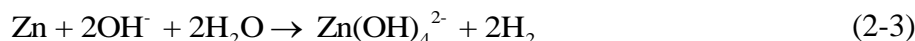


Fig 2.8: Proposed mechanism of ZnO nanorods growth in water under hydrothermal condition [95].

### 2.2.2.2 In alkali medium

The reaction in alkali medium mechanism is described in following equation:



The dissolution of Zn atoms into solution creates a concentration gradient of Zn<sup>2+</sup> and the intrinsic electric field of polar ZnO lattice could be a motivation for further growth of ZnO crystals along the c-axis [44]. The electrostatic interaction between the polar charges drives the preferred c-axis orientation of ZnO nanostructure to minimize surface energy.

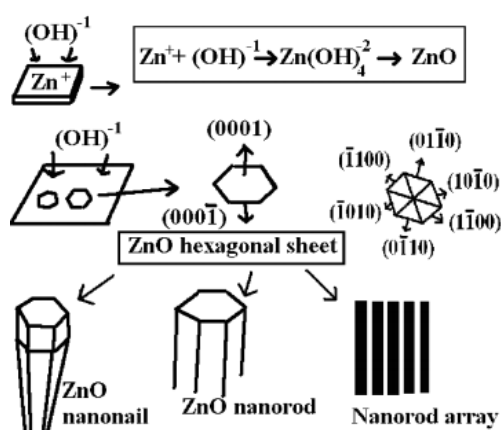


Fig 2.9. Schematic view of the growth mechanism of the ZnO nano form [108].

Kar et al. reported that Zn-rich positive (0001) surface are more reactive than the oxygen-rich negative (000-1) surface which attract new ZnO species to promote the anisotropic growth along the (0001) direction [108]. The six side facets are indexed by (10-10) family as shown in Fig 2.9 and it's well known that the growth rate corresponds to the sequence (0001)>(10-11)>(10-10). Normally, ZnO will grow in hexagonal structure along the (0001) direction but in some circumstance, the growth in this way is inhibited the lower specific surface energy such as (10-11) become preferred resulting in needle like ZnO array.

### 2.2.2.3 In amine medium

It has been known that ammonia could react with Zn to form ammonia complex [Zn(NH<sub>3</sub>)<sub>4</sub>](OH)<sub>2</sub> and under hydrothermal condition, this complex will be decomposed into ZnO. At initial stage, spherical ZnO nanoparticles are formed on the surface of Zn foil from reaction between Zn and ammonia. These nanoparticles will serve as seed for subsequent growth of ZnO. Along with the growth in c-axis, the side facets could react with ammonia which reduce the diameter of the nanorods as performed in Fig 2.10. When the reaction reaches the equilibrium, the shape of ZnO nanorods will hardly be changed [109].

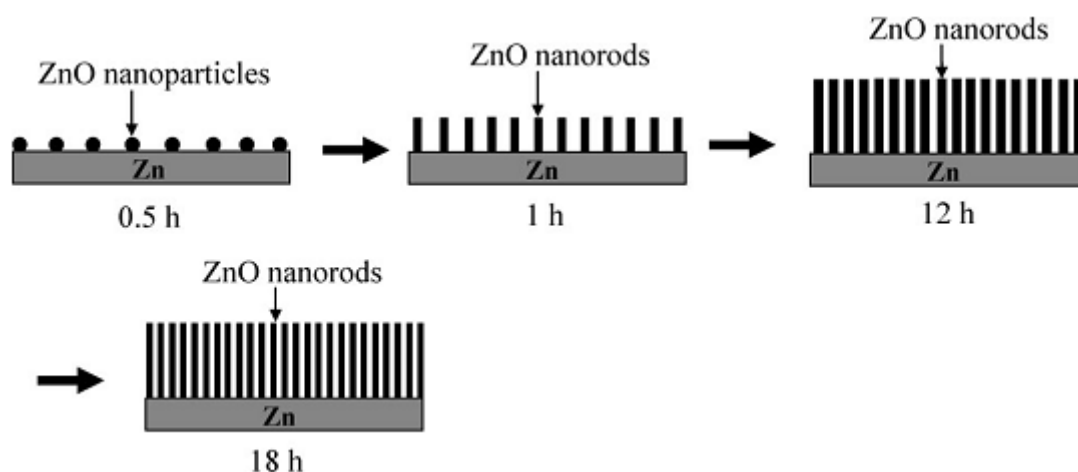
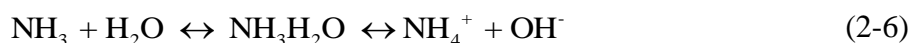


Fig 2.10. Schematic illustration of growth mechanism of ZnO nanorods array [109].

The most common reagent for ZnO nanorods growth is HMTA (Hexamethylenetetraamine) which is hydrolyzed into formaldehyde and ammonia, acting as pH buffer by slowly decomposing to provide a gradual and controlled supply of ammonia [110]. The reacting process are described as equations below:



The dehydration of monomeric hydroxyl species creates solid ZnO nuclei at the surface of the ZnO seed layer.

### 2.2.3 Silicon incorporation

The most common Si modified ZnO nanomaterial is about Si doped ZnO thin film [111, 112]. Incorporation with Si is a promising way to achieve low resistivity and high transmittance ZnO thin film [113]. Wu et al. also indicated the reduction in ZnO band gap from 0.73 eV to 0.34 eV at 12.5 %Si composition.

Beside silicon, silicon oxide is also utilized as stabilizer, protecting layer, passive layer and dielectric layer because of its inertness and transparency. To reduce immunogenic response when using implant devices, Chu et al. coated on ZnO nanorods a thin layer of SiO<sub>2</sub> using chemical vapor deposition [114]. Ranjbar et al. used SiO<sub>2</sub> as hydrophobic layer on ZnO for antifogging, self-cleaning, tribological and micro fluidics applications [115]. Thick silica shell, which quantum dots can be stabilized against photochemical degradation through, acts as stabilize metal clusters [50]. The key role of the silica shell is the retardation interaction with oxygen. Without the sufficient oxygen, direct electron-hole recombination dominates and the

material is photochemically stable [50]. By modifying the matrix refractive indices the position of the Au SPR band in the visible wavelength region can be controlled easily and systematically [49]. To be more specific, Medda et al. coated gold with different SiO<sub>2</sub> to TiO<sub>2</sub> mole ratio layer to obtain the distinct refractive indices. The higher the refractive index the higher gold surface plasmon resonance position [49]. In this work various thickness of SiO<sub>2</sub> layer on ZnO nanorods array will be investigated to test the effect of SiO<sub>2</sub> on ZnO nanorods.

## 2.2.4 Gold incorporation

### 2.2.4.1 Electron trap sites and spatial electricfield enhancement

When a semiconductor and a noble metal are brought into contact, the photocatalytic activity will increase. Due to the different Fermi level, work function of metal and band structure of semiconductor, a Schottky barrier is established at band interface, leading to a charge rectification [116]. Particularly, the work function of gold is 5.1 eV and the electron affinity of ZnO is 4.35 eV. Thus the Schottky barrier is approximately 0.75 eV in the case of gold in contact with ZnO. Under UV excitation, excited electron from ZnO is driven into the gold metal by the energetic different at the interface [117]. For balancing, gold automatically donates the electron for the acceptors in surrounding environment. In the other word, gold particles play a role as electron trap sites which promote the hole and electron separation. The process is described in Fig 2.11.

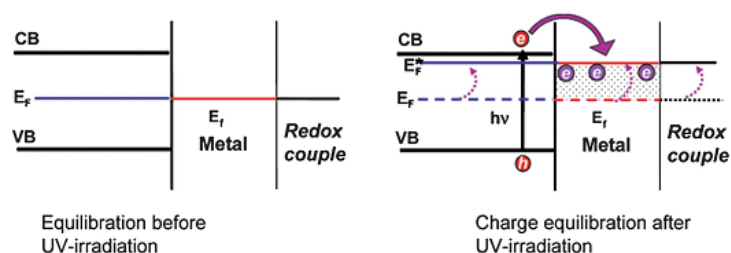


Fig 2.11. Electron transfer and Fermi level shift at a metal/semiconductor interface [117].

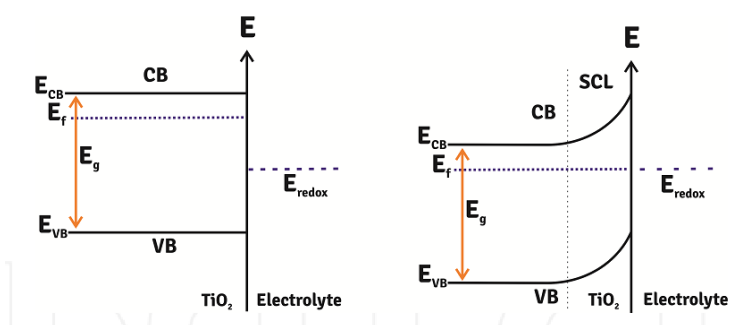


Fig 2.12. Energy band for n-type semiconductor and the formation of space charge area [116].

In photoelectrochemical measurement, semiconductors are dipped into the electrolyte. The difference in redox potential of electrolyte and fermi level of semiconductor leads to band bending at equilibrium to have the flow of charge from electrolyte to semiconductor [118]. The region where the band bending is, is called space charge layer (SCL). The process is shown in Fig 2.12

When applying the bias, fermi level also can be controlled [118]. At the initial, band edge is flat because the potential drop between the interfaces is zero which is called flat band potential. Applying the bias greater than flat band potential will result in band bending. Under light irradiation, the excited electron will flow via the external circuit to counter electrode. The greater band bending, the faster electron/hole separation takes place [116]. The whole process is illustrated in Fig 2.13.

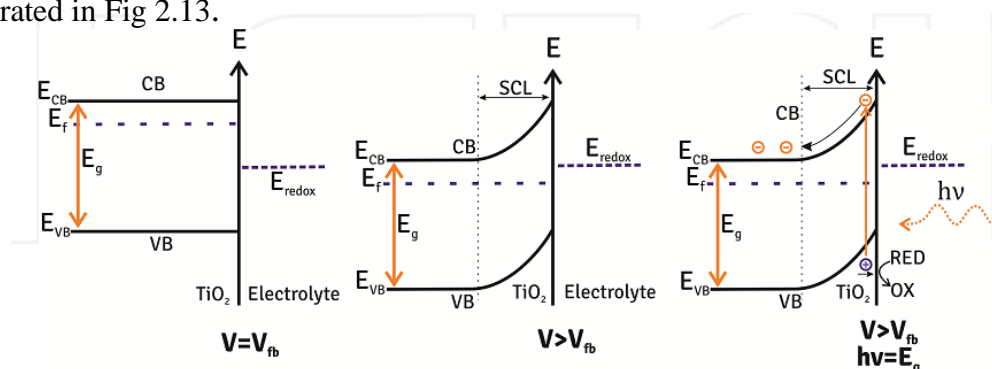


Fig 2.13. Band diagram when  $V=V_{fb}$ ,  $V > V_{fb}$  and  $V > V_{fb}$  when irradiated [116].

By Au loading, a lot of Schottky barrier junctions are formed which enhance the surface band bending significantly. This leads to a stronger spatial electric field which efficiently reduces the electron-hole pair recombination [119].

#### 2.2.4.2 Surface plasmon resonance (SPR)

SPR which is defined as the resonant photon-induced collective oscillation of valance electrons, is established when the frequency of the photo matches the natural frequency of surface electrons oscillating against the restoring force of positive nuclei [8]. Gold, silver and copper nanostructure perform the resonant when contacting with large fraction of abundant solar flux including UV-vis photon. Controlling the nature, size and shape of these metallic structures offers the desirable resonant wavelength and SPR intensity in area of interest, solar energy [120]. SPR effect promotes the rates of photocatalyst reactions by concentration of charge carriers through three non-mutually exclusive energy-transfer mechanisms, SPR-mediated charge injection from metal to semiconductor, near-field electromagnetic and scattering mechanisms.

Charge injection mechanism imitates the dye sensitizer where a dye molecule absorbs light and transfer energetic charge carriers, created in the process of the SPR excitation to the nearby semiconductor [121]. As a result, charge injection should play an important role in water splitting process mainly in visible region because of its plasmon band [122]. The schematic of this mechanism is illustrated on NHE scale in Fig 2.14.

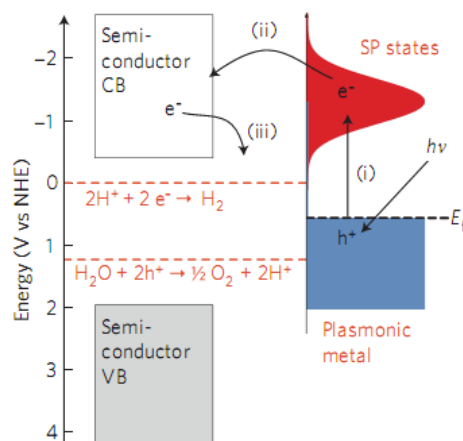


Fig 2.14. Mechanism of charge transfer from SPR band under visible light [8].

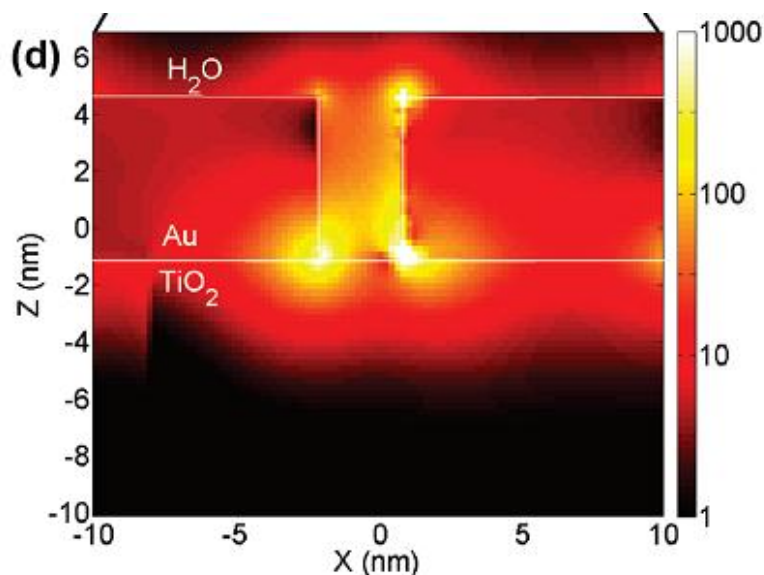


Fig 2.15. Electric field intensity at the interface of Au – TiO<sub>2</sub> calculated using FDTD

The near-field electromagnetic mechanism is described as the interaction of the semiconductor with the strong SPR-induced electric field localized nearby at the metallic nanostructure [8]. This electric field is spatially non-homogeneous with highest distributed at the surface and dramatically reduced throughout the depth. When a semiconductor is in contact with photo-excited plasmonic structure, the intense field will accelerate the rate of electron-hole pair formation. The formation of electron-hole pair at surface is beneficial for the

separation and short migration distance to the reagent of these charge carriers which is meaning full in water splitting reaction [123]. The simulated electric field distribution is displayed in Fig 2.15.

Additionally to the local electric fields, scattering of resonant photons are considered for large plasmonic structure (larger than 50 nm in diameter) [124]. This mechanism indicates the increase of average photon path length in plasmonic nanostructures and semiconductor composites which enhances the possibility of electron-hole pair formation. If the resonant photons are not absorbed on the first pass by semiconductor, the plasmonic nanostructures cause these photons to scatter many time in the system. A schematic about this mechanism is shown in Fig 2.16.

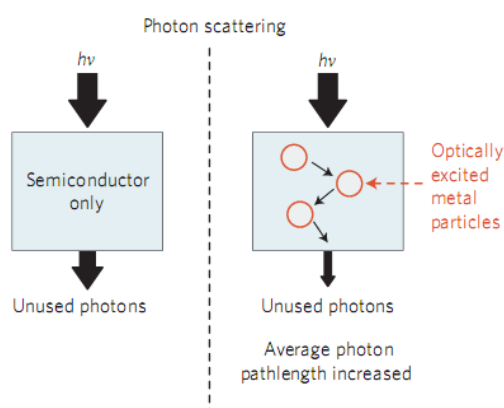


Fig 2.16. Schematic illustrating the scattering mechanism [8].

These three mechanisms are the main reasons explaining for SPR effect in composite materials. Depending on each condition, one of these mechanism will dominate the others.

## CHAPTER 3. MATERIALS FABRICATION

This chapter shows in detail the method to dope silicon directly on TNTs by hydrothermal method and the method to synthesize ZnO nanorods then coating it with gold and silicon dioxide in different orders.

### 3.1 Si doped TiO<sub>2</sub> nanotubes synthesis

#### 3.1.1 Hydrothermal reaction using TMAH as reagent

All chemicals were used as received without further purification. An amount of P25 powder (anatase, 99.7 %, Sigma-Aldrich) was placed in the Teflon tube together with different amount of TMAH 25%. Two main ratios  $Ti/TMAH = 0.81$  and  $Ti/TMAH = 2.4$  were investigated [69]. The Teflon tube was then heated at 125°C at various time under stirring condition. The white precipitates were washed with distilled water and HCl 0.01 M many times and separated using centrifugation (10 min, 22°C, 1800 rpm). The final product was dried at 80°C for 8h in electric oven.

#### 3.1.2 Hydrothermal reaction using NaOH as reagent

This work induces Si element into TNTs structure directly by hydrothermal method. TNTs were prepared using hydrothermal method proposed by Kasuga et.al [75]. Typically, 1.6 g TiO<sub>2</sub> (anatase, 99.7 %, Sigma-Aldrich) were mixed with different amounts of Si powder and 75 ml of NaOH 10 M in a 100 ml Teflon tube which was then heated at 150°C in 24h under stirring condition on a heater. The  $Si/(Si+Ti)$  mol ratio is varied from 0.01 to 0.3. After reaction, the white precipitates were filtered and washed several time with water and HCl 0.1 M until pH of washing solution approached 7.0. Finally, the sediment was dried at 80°C overnight and calcined at 450°C for 1h. The as synthesis samples were labelled as X-TNTs (X = the  $Si/(Si+Ti)$  mole ratio).

### 3.2 SiO<sub>2</sub> and Au layer on ZnO nanorods array synthesis

#### 3.2.1 Hydrothermal growth of ZnO nanorods directly on Zn metal using DI water

All chemicals were used as received without further purification. Surface treatment of Zinc foils (99.9%, Sigma-aldrich) with a thickness of 250 µm were carried out under ultrasonic conditions with absolute ethanol. Then a piece of Zn foil (10 x 20 x 0.25) was placed upside down at the bottom of a Teflon tube (capacity, 100 ml). 80 ml of deionized water (pH = 6-8) was added in this tube as oxidation reagent. After sealing, the Teflon tube was put into an electric oven at 95°C in 24h. Finally, the Zn foil was taken out, rinsed with water, absolute alcohol and rinsed in air.

### 3.2.2 Hydrothermal growth of ZnO nanorods directly on Zn metal using KOH

The same process above was repeated. Instead of using DI water, 0.18 M KOH was used as nanorods growing reagent. The hydrothermal reaction was carried out at 95°C in 21h30 to obtain the homogeneous morphology. The sample was then anneal at 350°C in 2 hours to get better crystallinity of ZnO.

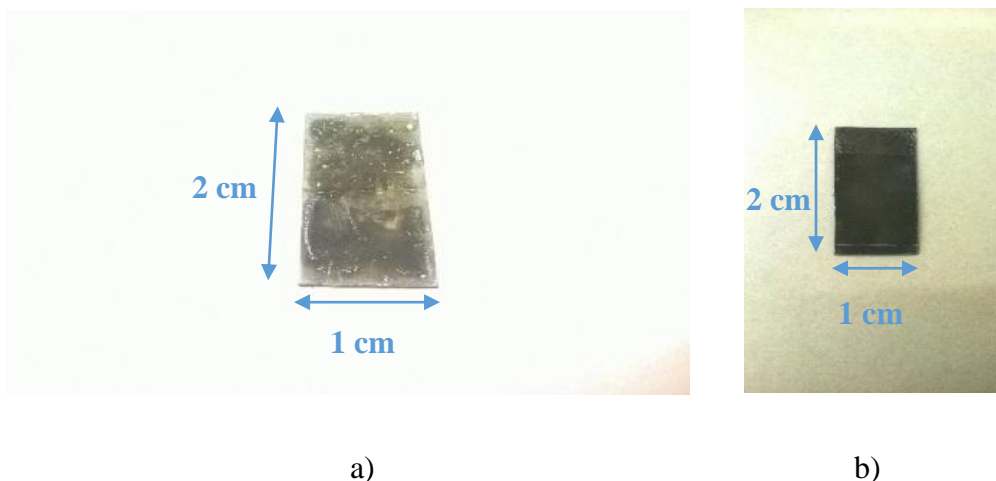


Fig 3.1. Image of ZnO nanorods array on Zn foil a) using water b) using KOH after hydrothermal treatment.

### 3.2.3 Two steps hydrothermal growth of ZnO nanorods on ITO glass

ZnO nanorods were deposited on ITO glass via two steps. A seed layer was created on the surface of ITO glass using dip coating method in the first step. In the second step, ZnO nanorods were grown on this seed layer using hydrothermal method.

0.22 g of zinc acetate powder were mixed with 10 ml of ethanol in a small jar in 2 hours until a clear and homogeneous solution was obtained. A piece of ITO glass (12 x 25 x 1 mm) was ultrasonically washed with acetone and ethanol respectively in 20 min.



Fig 3.2. 3D schematic of hydrothermal treatment a) on Zn foil b) on ITO glass.

This piece of glass was dipped in the as prepared solution within 20 sec and withdrawn at a slow, constant speed to maintain a uniform and thin layer of liquid. The process is displayed

in Fig 3.2. After annealing at 90°C in 30 min, dip coating and annealing steps were repeated several times to achieve the desired thickness.



Fig 3.3. Image of dip coating process.

Before hydrothermal treating, the ITO glass with seed layer was annealed in air at 200°C for 1 hour and clamped upside down in the Teflon tube containing 60 ml of 0.025 M zinc nitrate and hexamethylenetetramine. The hydrothermal treatment was conducted at 90°C in 4 hours in an electric oven. Finally, the ITO glass was rinsed several times with water and ethanol, dried at room temperature and calcined at 450°C in 30 min.

### 3.2.4 Deposition of the silicon oxide and gold layer

Gold thin film layer was deposited using Au sputter VG Microtech SC500 machine. Ar gas is purged into the chamber of this machine as the bombard reagent. To sputter approximately 5 nm of Au, the current is maintain at 10 mA in 110 sec. SiO<sub>2</sub> thin film layer was deposited using AJA sputtering machine.



a)



b)

Fig 3.4. a) Au sputter VG Microtech SC500 machine b) AJA Sputtering.

As can be seen from Fig 3.5, sputtering is a physical vapor deposition process. The main principle can be explained in three main steps: The bombardment of sufficiently energetic

particles (Ar<sup>+</sup>) on target surface, the ejection of the atom from the surface of the sputtering target and the ejected target atoms transferred to substrate. There are different types depending upon process conditions: RF sputtering, DC sputtering, Magnetron Sputtering and Reactive sputtering. Here in, the sputtering condition is the RF Magnetron sputtering.

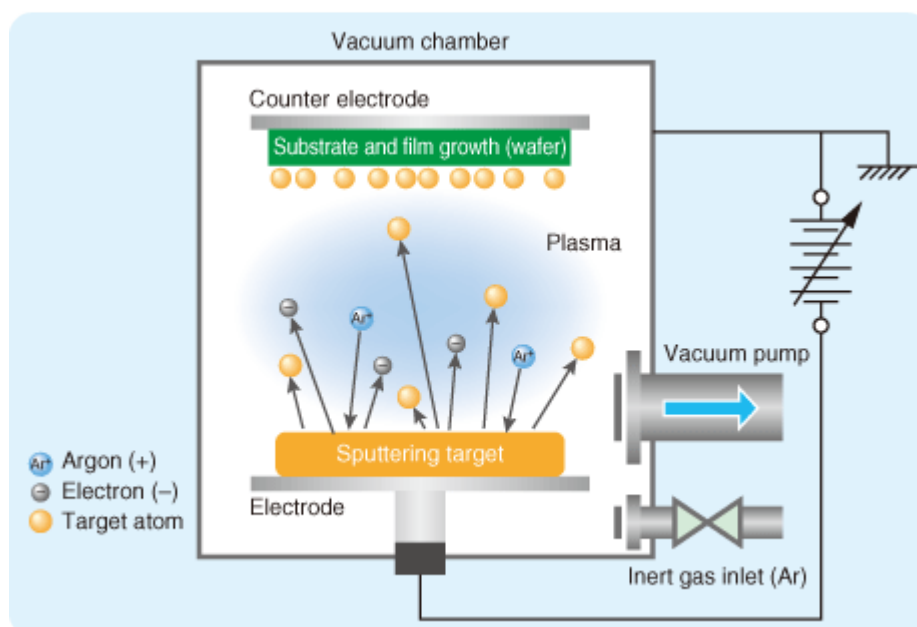


Fig 3.5. Illustration of sputtering process.

#### 3.2.4.1 Deposition of SiO<sub>2</sub> on ZnO nanorods array synthesized by using KOH

To investigate the effect of SiO<sub>2</sub> layer, 4 samples of ZnO nanorods array on Zn foil were prepared. 5, 10, 15 nm SiO<sub>2</sub> layer were sputtered on these samples. There are almost no visual differences in these samples after sputtering.

#### 3.2.4.2 Deposition of SiO<sub>2</sub> and Au on ZnO nanorods array on ITO glass

As discussed above, to investigate different plasmonic configurations, 5 labeled samples (1,2,3,4,5) were coated with nothing, SiO<sub>2</sub>, Au, SiO<sub>2</sub> then Au and Au then SiO<sub>2</sub> respectively as sketched in Fig 3.6. To be more specific, sample 3 and 5 were covered by 5 nm gold using VG sputtering. Then, sample 2, 4 and 5 were covered with 5 nm SiO<sub>2</sub> using AJA sputtering. Finally, sample 4 was covered with 5 nm gold in the same condition with sample 3 and 5.

The general conditions for sputtering SiO<sub>2</sub> and gold are recorded in Table 3.1 and Table 3.2 respectively.

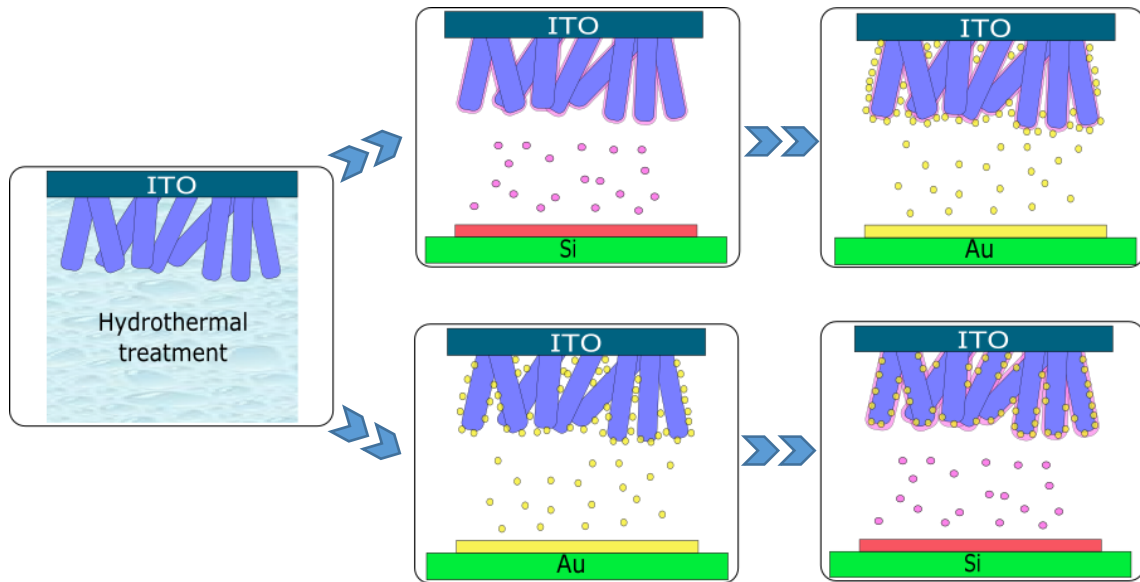


Fig 3.6. The schematic of fabrication process.

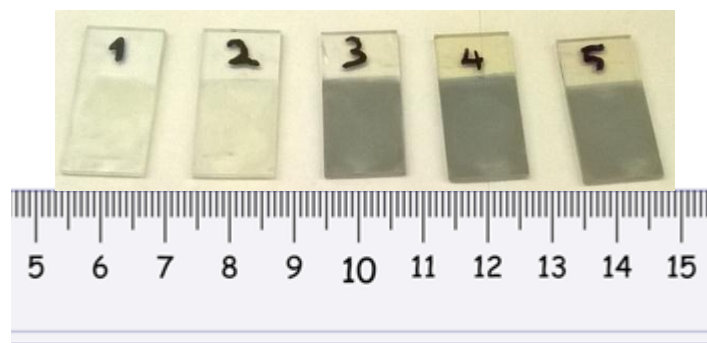


Fig 3.7. Picture of 5 samples after sputtering.

Table 3.1 SiO<sub>2</sub> Sputtering condition

Element	Pressure (mT)	Power (W)	Rate (Å/s)	Ramp (s)	Thickness (nm)	Gas (sccm)
SiO <sub>2</sub>	3.3	130	0.1	10	5	5

Table 3.2 Au Sputtering condition

Element	Pressure (bar)	Time (s)	Current (mA)
Au	0.08	110	10

## CHAPTER 4. MATERIALS CHARACTERIZATION AND MEASUREMENTS

In this part, the principle of the equipment for characterization and measurements will be investigated. The morphology of the nanostructure of the as prepared materials was revealed using scanning electron microscopy transmission electron microscope. The crystal structure and the absorption ability were tested using X-ray diffraction and Uv-vis spectroscopy respectively. Methylene blue (MB) degradation test and PEC test were also utilized.

### 4.1 Hydrothermal equipment

The schematic of hydrothermal equipment is illustrated in Fig 4.1. This equipment includes two part: the outside stand-less steel tube and the inside Teflon tube with the total reaction volume around 100 ml. The maximum working temperature and pressure are 220°C and 3-4 MPa respectively. There is a special rubber ring inside the Teflon tube to guarantee the sealing during hydrothermal reaction.

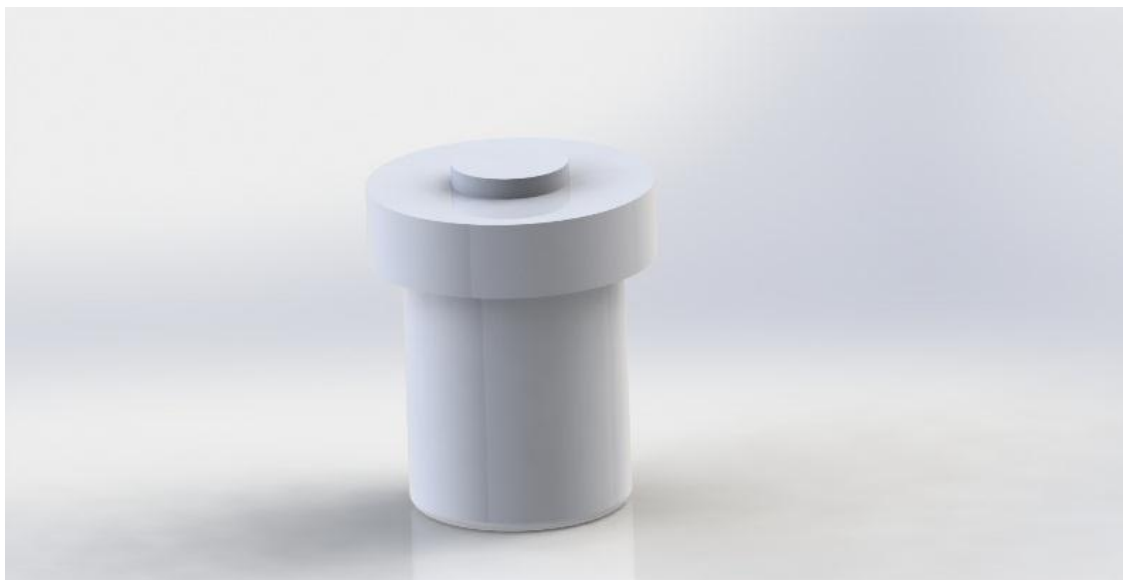


Fig 4.1. 3D schematic of hydrothermal reactor.

### 4.2 Materials characterization

#### 4.2.1 Scanning electron microscopy (SEM), Energy-dispersive X-ray spectroscopy (EDX) and Mapping

The morphology and composition of catalyst were characterized using scanning electron microscopy (SEM, Hitachi 1081) with accelerating voltage is 30 kV. An Energy-dispersive X-ray spectroscopy (EDX) is integrated in the SEM machine which is used to determine the

component proportion. The distribution of each component can also be tested using mapping mode in EDX operation.

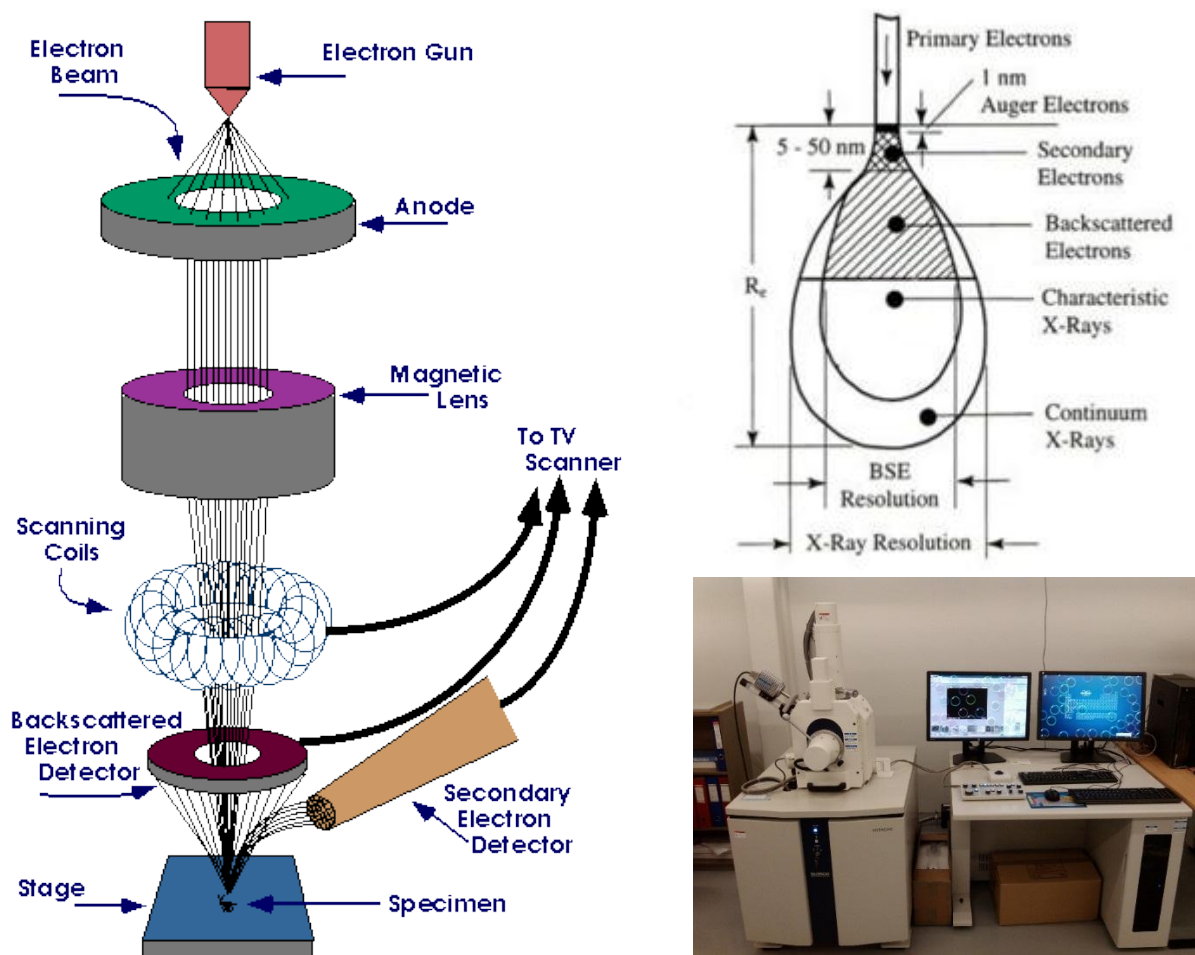


Fig 4.2. The schematic of SEM working principle.

By the bombardment of the electron beam on the specimen, three main type of signals are secondary electron (SE), reflected or back scattering electron (BSE) and photons of characteristic X-rays as shown in Fig 4.2. Depending on the acceleration voltage, the depth of field will be varied. SE contrast depends mainly on work function and topography while BSE is in proportional with the average atomic number of the sample. The characteristic X-rays is used to define which element presented in the specimen.

The sample preparation for SEM is quite simple for conductive materials, in this case, Zn foil and ITO glass while TNTs powder is more complicated. TiO<sub>2</sub> oxide is a very weak conductive material which is needed to be dispersed carefully on the two sides copper conductive tape for the observation. The charge accumulation is therefore reduced which produces better topology image.

#### 4.2.2 X-ray diffraction (XRD)

The crystallinity of TNTs was recorded by X-ray diffraction (XRD) using a diffractometer with Cu K $\alpha$  radiation with  $\lambda = 0.156$  nm (Bruker AXS D8 Discover). Using some relevant figures and equations, the crystal size can be estimated based on the XRD pattern.

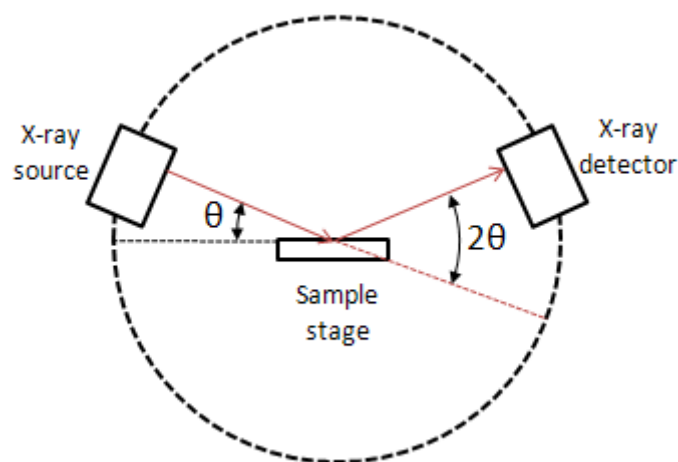


Fig 4.3. Illustration of XRD working principle.

Fig 4.3 performs the X-rays path from the source to sample and then to X-ray detector. This X-ray beam hits a sample and is diffracted, the distances between the planes of the atoms that constitute the sample by applying Bragg's Law, named after William, can be measured. According to Bragg's Law:  $n\lambda = 2d \sin\theta$ , where the integer  $n$  is the order of the diffracted beam,  $\lambda$  is the wavelength of the incident X-ray beam,  $d$  is the distance between adjacent planes of atoms (the  $d$ -spacings), and  $\theta$  is the angle of incidence of the X-ray beam, various crystal information can be extracted.

In this work, only crystal structure of TNTs is needed to be identified because it relates directly to the photocatalytic performance. About ZnO, the major structure at the processing condition is hexagonal wurtzite and hardly changed. Thus, the XRD measurement is not necessary.

#### 4.2.3 Uv-vis absorption

The absorption spectra were recorded on a spectrophotometer (SHIMADZU, UV-2600 with ISR-2600 integrating Sphere Attachment) in range of 220-830 nm with fine BaSO<sub>4</sub> powder as reference. This is utilized to measure the absorption ability of the substances.

This is the measurement based Beer-Lawbert law of attenuation of a light after passing through a sample (Fig 4.5) or after reflection from a sample surface (Fig 4.4). The working

principle of UV-vis absorption bases on the fact that molecular can absorb energy in form of ultraviolet or visible light to excite the internal electron to higher energy level.

To test the absorption ability of TNTs powder, it must be mounted on a glass piece by doctor blade method. Then this piece of glass with the thin film of TNTs on top is placed in the sample holder of the machine. This process is much easier for ZnO nanorod arrays on Zn foil or ITO glass. For photodegradation test, the reference sample was DI water contained in quartz cell.

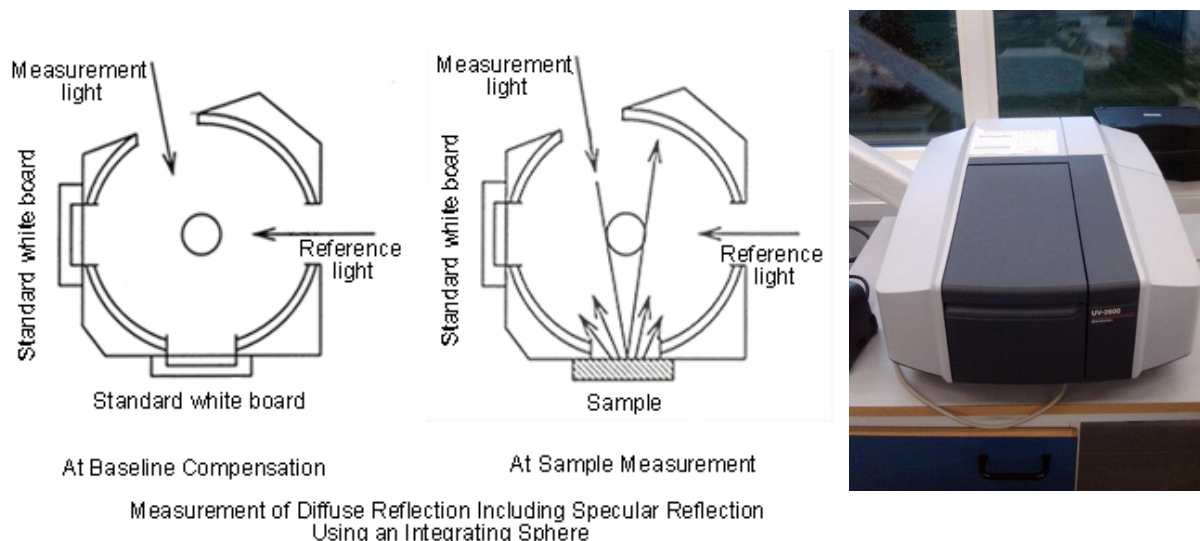


Fig 4.4. Schematic of UV-vis machine and measurement for solid sample.

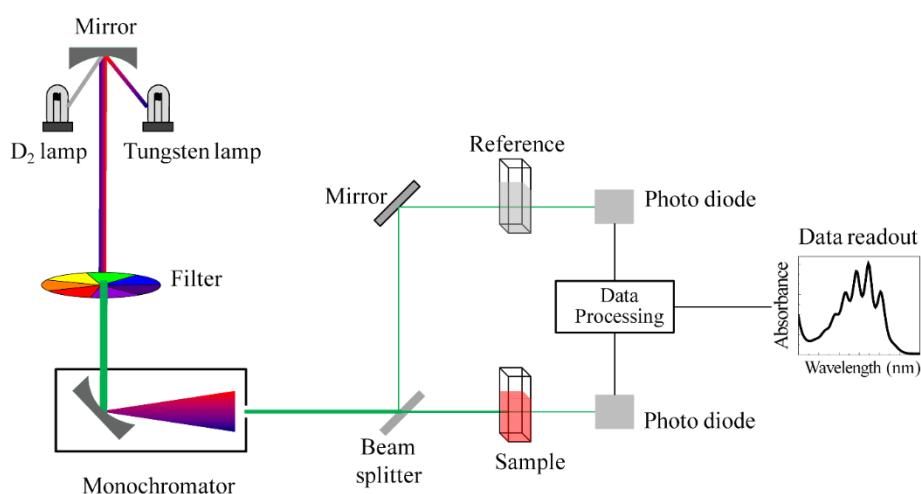


Fig 4.5. Schematic of UV-vis measurement for liquid sample.

#### 4.2.4 Transmission electron microscopy (TEM)

The TEM operates on the same basic principles as the light microscope but uses electrons instead of light. Because the wavelength of electrons is much smaller than that of light, the

optimal resolution attainable for TEM images is many orders of magnitude better than that from a light microscope. Thus, TEMs can reveal the finest details of internal structure. It can be seen from Fig 4.6 that the beam of electrons from the electron gun is focused into a small, thin, coherent beam by the use of the condenser lens. This beam is restricted by the condenser aperture, which excludes high angle electrons. The beam then strikes the specimen and parts of it are transmitted depending upon the thickness and electron transparency of the specimen. This transmitted portion is focused by the objective lens into an image on phosphor screen or charge coupled device (CCD) camera. Using this technique, the hollow structure of TNTs can be revealed.

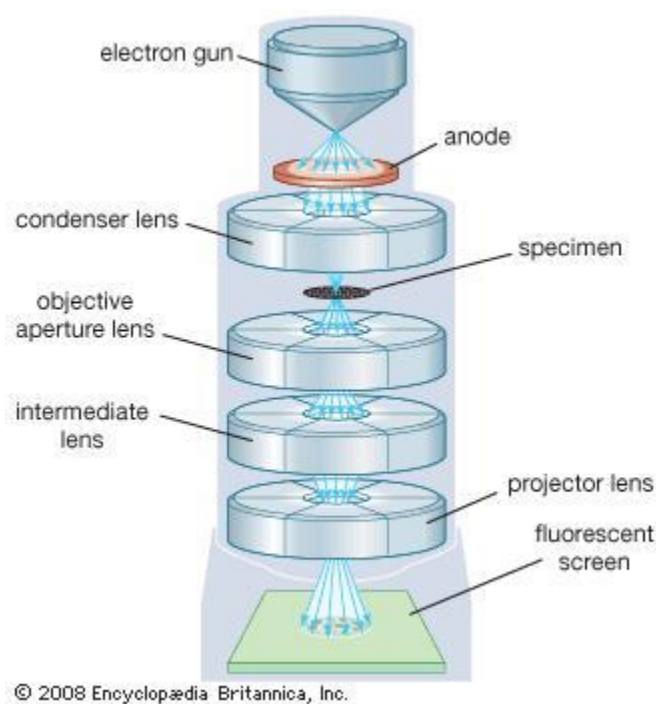


Fig 4.6. Schematic of TEM working principle.

## 4.3 Measurements

### 4.3.1 Methylene blue (MB) degradation test of Si doped TNTs

To evaluate the photocatalytic performance of TNTs and modified TNTs, the degradation of aqueous solution of methylene blue was carried out. 20 mg of catalyst powder was placed into 50 ml of 25 ppm methylene blue solution under stirring condition in dark for 30 min. After that, the photocatalytic reaction was taken place under ultraviolet ray, UV-LED illumination (HAMAMATSU L10561) with the maximum irradiance of 14000mW/cm<sup>2</sup> @ 365 nm and 15000 mW/cm<sup>2</sup> @ 385 nm and with wavelength 365 nm. The duration of irradiation were 10, 15, 30, 45 and 60 min. Finally, the adsorption spectra of solution were recorded by UV-vis spectrophotometer.

### 4.3.2 Methylene blue degradation test of ZnO nanorods array on Zn metal

To evaluate the photocatalytic performance of pure ZnO nanorods array and SiO<sub>2</sub> modified ZnO nanorods array, the degradation of aqueous solution of methylene blue was conducted. A piece of ZnO nanorods array (10 x 20 x 0.25 mm) was clamped and dipped in 50 ml solution of 6.25 ppm methylene blue. After that, the photocatalytic reaction was taken place under white light source using halogen lamp 15V/150W. The duration of irradiation were 30, 60, 90, 120, 150 and 180 min. Finally, the adsorption spectra of solution were recorded by UV-vis spectrophotometer.

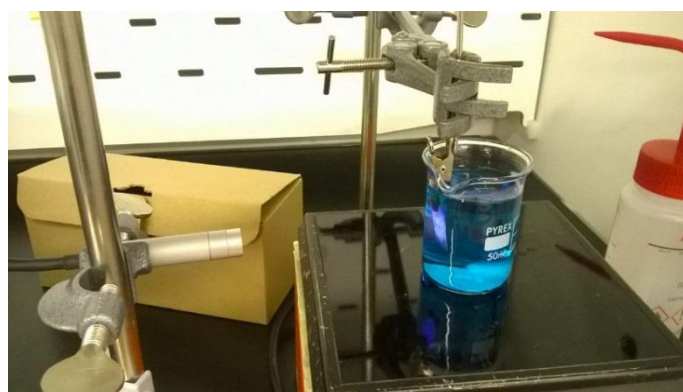


Fig 4.7. Methylene blue degradation setup.

### 4.3.3 Photoelectrochemical (PEC) measurement of ZnO nanorods array on ITO glass

The electrochemical characterization was conducted using three electrode-based methods with a standard electrochemical workstation (Zahner elektrik IM6). The ITO glass with difference coating layer on ZnO nanorods (effective layer 1 cm<sup>2</sup>) was the working electrode following by Ag/AgCl and Pt electrode as the reference and counter electrode respectively. 0.5 M Na<sub>2</sub>SO<sub>4</sub> (pH= 6.8) solution was the supporting electrolyte for all measurement. The light sources, white light source (halogen lamp 15V/150W) is utilized to test the photoelectrode current of sample in visible region.

#### 4.3.3.1 Steady state measurement

I/E scanning mode was used to carry out the steady state measurement. The voltage varied in range of -0.3 V to 1 V. There are two testing conditions for each sample, dark and white light illumination. The changing of current corresponding to voltage was recorded.

#### 4.3.3.2 Transient photoresponse

To evaluate the response ability to the light in white light, the transient photocurrent responses were conducted. POL setup was chosen with the bias voltage fixed at 0.5V. The sample first was remained in dark for 30s then exposed to the light for 40s. The response was recorded as light on and light off.



## CHAPTER 5. RESULTS AND DISCUSSION

Various morphology of TiO<sub>2</sub> and ZnO synthesized by using different templates are compared. The reasons for the enhancement in photocatalytic performance of these modified catalysts are proposed strictly based on theory and the other works.

### 5.1 Silicon doped TiO<sub>2</sub> nanotubes

#### 5.1.1 Morphology of titania using TMAH as reagent

The first observation was about the size of the precipitates. The nano size of the particles did not allow it to be separated by using normal filter paper with micro pores. Thus, centrifugation was utilized leading to low yield. Some of products were characterized under SEM machine which are shown in Fig 5.1.

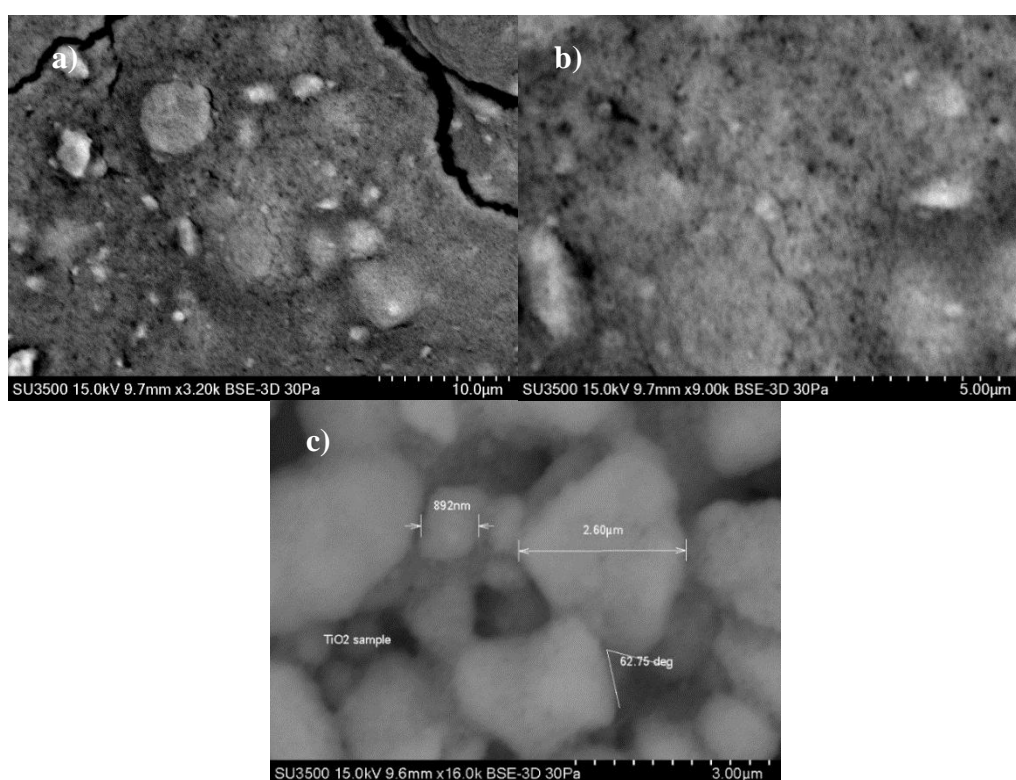


Fig 5.1. Titania morphology from reaction with a) TMAH 5 wt.% b) TMAH 8.3 wt.% c) TMAH 25wt. %

Different concentrations of TMAH were conducted with the same Ti/TMAH ratio. The morphology of Fig 5.1a) is unidentified because of the non-uniform of the catalyst. The sample with TMAH 8.3 wt.% shows the porous surface with various pore sizes. The final sample is the agglomeration of various particle sizes. By controlling the concentration of the TMAH, we could synthesize various morphology of titania [37]. However, no specific structure of titania was observed, especially nanotubes. According to nanotubes formation mechanism, this is due

to the large size of Me<sub>4</sub>N<sup>+</sup> compared to Na<sup>+</sup> which inhibits the scrolling mechanism. Therefore, no further investigations about TMAH are made.

### 5.1.2 Morphology of titania nanotubes using NaOH as reagent

Most of nanofibers or nanotubes are in cluster form which make the imaging of individual component by SEM become difficult. There are two main modes which are backscattering electron (BSE) and secondary electron (SE). BSE mode offers better contrast while SE mode offer better surface topology.

#### 5.1.2.1 Backscattering electron

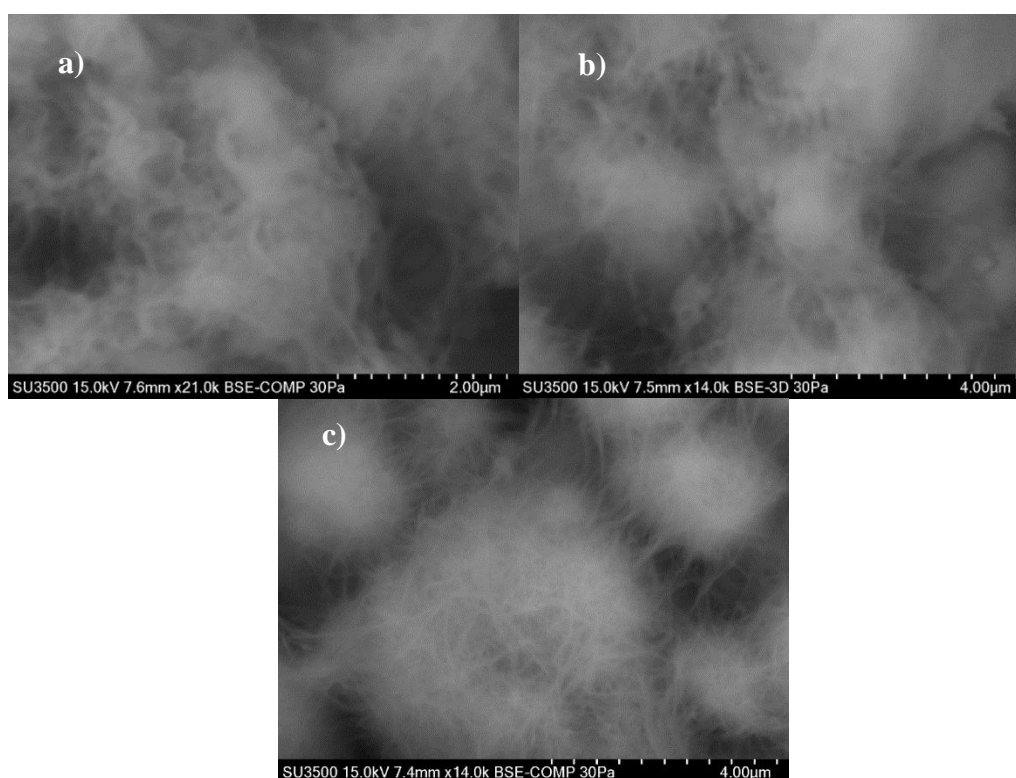


Fig 5.2. SEM image of TiO<sub>2</sub> nanotube a) at 5 hours reaction time b) at 24 hours reaction time c) after doping with small amount of Si.

Fig 5.2 illustrates the nanofibers or nanotubes of TiO<sub>2</sub> with different reaction time and reagents. The first figure proves that nanofibers or nanotubes were established from very beginning of the reaction stage. The overall morphology seem to be lower in amount and shorter in dimension compared to longer time reaction. This is in good agreement with Thu et al. group [125]. After doping with silica, the morphology of TiO<sub>2</sub> did not change much which implies that silica did not inhibit the formation of tubes [75]. The structure of doped sample is still nanofibers or nanotubes.

### 5.1.2.2 Secondary electron

Fig 5.3 shows clearer the topology of TNTs with low and high amount of Si doping. The higher resolution could reveal more details. It's obviously that at high amount of Si doping the structure of fibers is much smaller and the overall morphology is just like flowers. This is due to the pressure variation proportionally with the amount of doped silica. When silica powder reacts with NaOH, hydrogen will be released which increases the pressure in the whole system. At low dope level, the tubes appear to be thin and long in dimension.

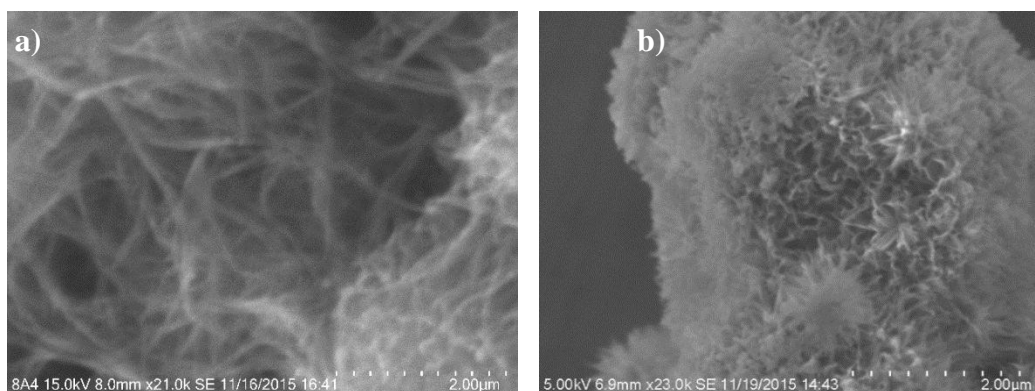


Fig 5.3. SEM image of TiO<sub>2</sub> nanotubes using secondary electron mode a) 0.01 Si doping b) 0.3 Si doping.

For better visualization, the nanotubes powder is dispersed in isopropanol under ultrasonic condition. Some of tubes were detached from the clusters which are easier for observing the individual tube. Fig 5.4 performs the dimension of individual tube. The dimension of these tubes are not uniform. Most of them are in range of 5 nm to 30 nm in diameter and several micrometers in length.

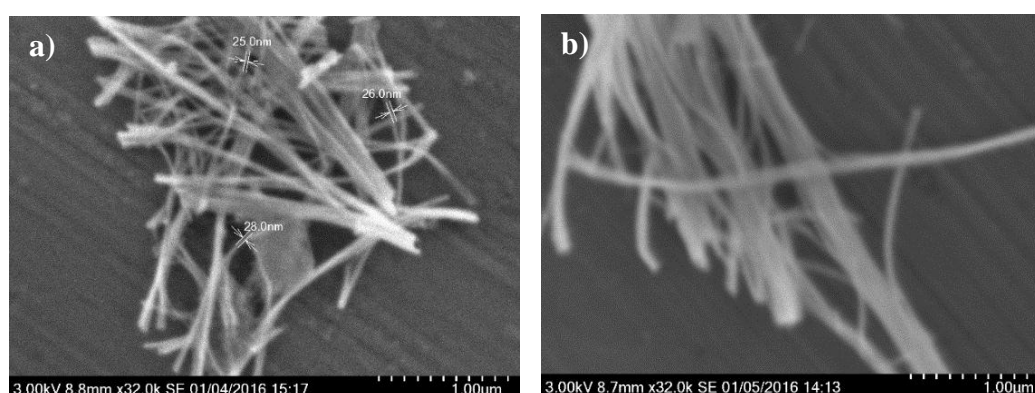


Fig 5.4. High resolution SEM image of a) undoped TiO<sub>2</sub> nanotubes b) doped TiO<sub>2</sub> nanotubes.

### 5.1.3 Transmission electron microscopy (TEM)

Fig 5.5(a) shows the TEM images which confirm the hollow structure of TNTs. A single tube with diameter of 7 nm and lattice fringes which represents for crystal structure of TNTs after heat treatment is revealed in Fig 5.5(b). It has clearly been seen that the morphology of

TNTs was not deformed after heat treatment at 450°C. Furthermore, there are no significant differences in the physical appearance of TNTs before and after doping. This observation is in good agreement with Kasuga et al. result [75] that SiO<sub>2</sub> does not affect the formation of TiO<sub>2</sub> nanotubes by chemical treatment method.

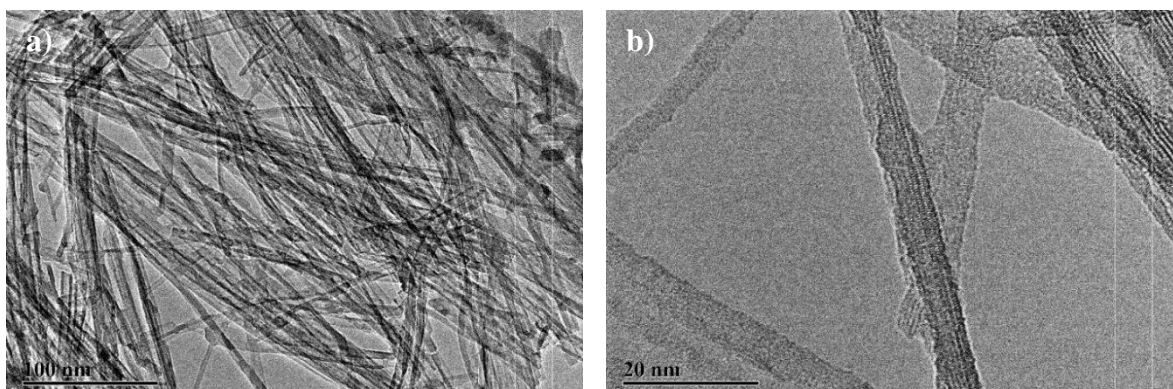


Fig 5.5. TEM image of titania nanotubes a) Individual tube b) Numerous tubes.

#### 5.1.4 Composition of TiO<sub>2</sub> nanotubes

In spite of high silica doping amount, hydrothermal treatment is an effective method for removing all amorphous Silica [75]. The same observation under EDS method is indicated in table 5.1. Very small amount of silica remains in the TNTs after hydrothermal treatment [68]. The amount of silica are varied from sample to sample but the exact value is unknown because of the uncertainty of EDS results.

Table 5.1 The composition of Si doped TiO<sub>2</sub> samples

Amount of Silicon (% mol)	Si actually doped (%mol)	Amount of TNTs (%mol)
1	0.17	99.83
5	0.20	99.80
10	1.18	98.80
30	0.73	99.27

Utilizing the mapping technique in EDS, the distributions of each component are illustrated in Fig 5.6. According to this results, the distribution of silica over titania is very uniform. However, because of low signal (dope level), this result is not so reliable.

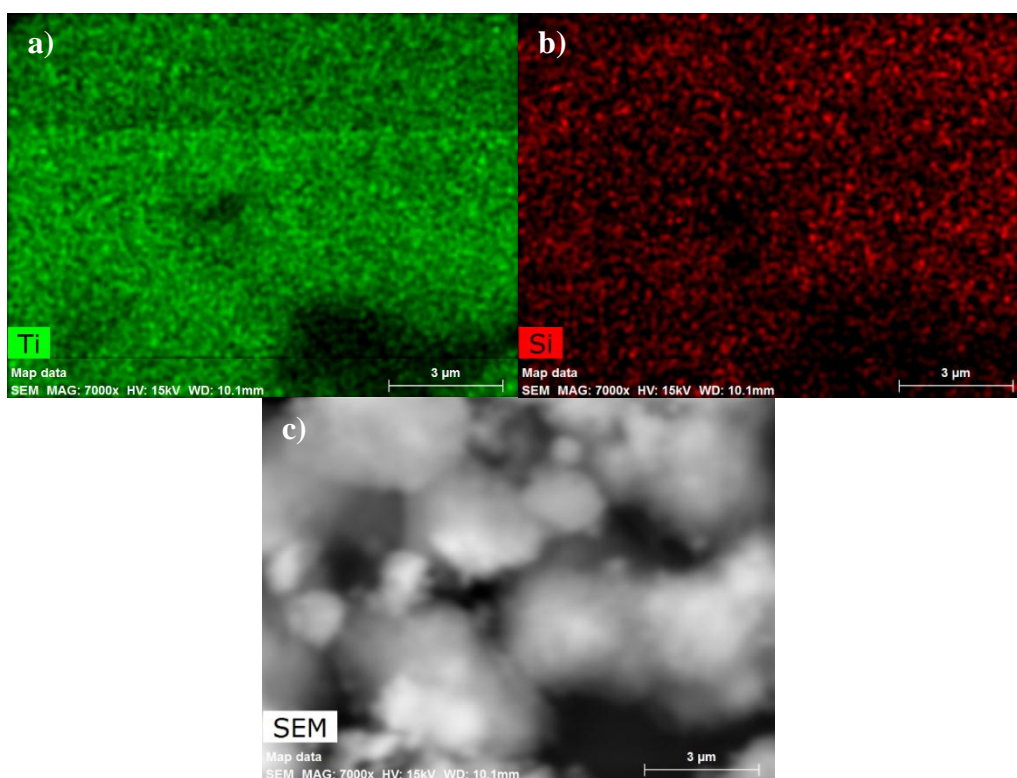


Fig 5.6. Mapping profile of a) Titanium b) Silica and c) the SEM image of 0.1 Si doped sample.

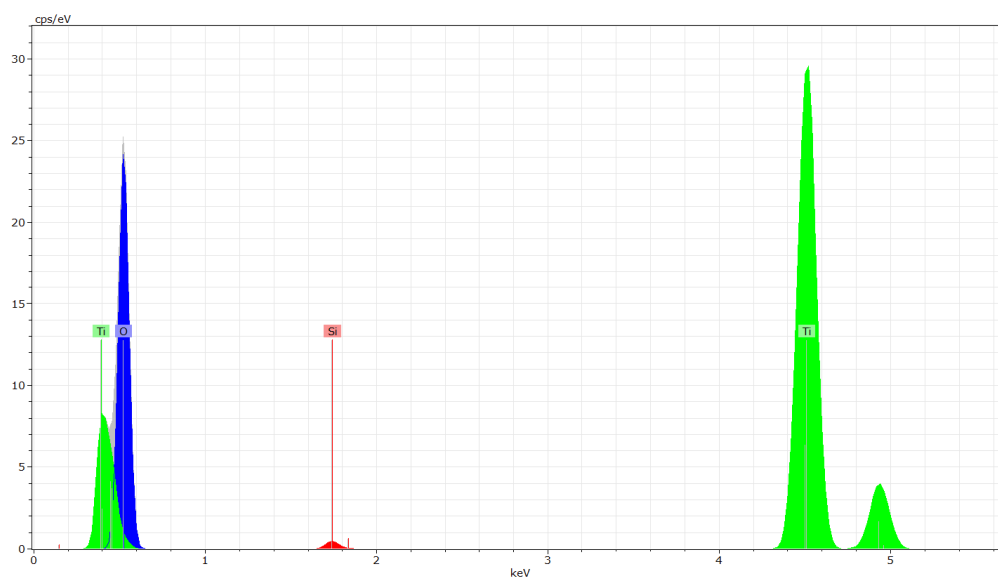


Fig 5.7. EDS spectra of 0.1 silica doped sample.

The EDS spectra (Fig 5.7) reflect the composition ratio of the sample. In this 0.1 silica doped TNTs, The mole ratio between titania and oxide is equal to 2 which is compatible with the compound TiO<sub>2</sub>. Beside a small amount of silica, there are also some impurities from incomplete washing process such as sodium and chloride.

### 5.1.5 Crystal structure of TiO<sub>2</sub> nanotubes

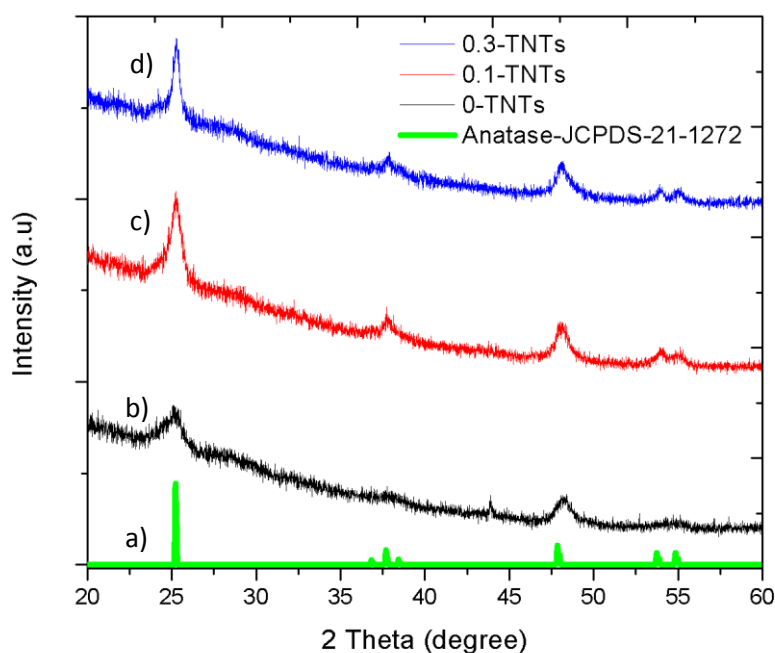


Fig 5.8. XRD pattern of a) Standard anatase crystal b) TiO<sub>2</sub> nanotubes c) 0.1 Si doped TNTs d) 0.3 Si doped TNTs.

The crystalline structure of doped and undoped samples were followed by employing XRD analysis techniques, as shown in Fig 5.9. The significant peaks at  $2\theta$  values 25.3, 37.8, 48, 53.9, 55.17 correspond to plane (101), (004), (200), (105), (211) respectively according to JCPDS-21-1272 standard. No trace of peak proves the existence of rutile or any titanate phases which denotes that there is no phase transformation and titanate has been decomposed into pure anatase phase at 450°C. The same results were reported by Natarajan et al. [126]. The different point between doped and undoped sample is the crystallinity. Pure TNTs sample performs poor crystallization. Introducing silicon supports the growth of anatase crystal which is chemically and optically active and widely used as catalysts and supports [127]. The crystal characteristics and size which was calculated based on the Scherrer's equation are illustrated in the table 5.2. The lattice spacing of plane (101) is quite close to that of anatase crystal [128]. Compared to the crystal size of precursor 25 nm, TNTs have smaller average size. Doping with silicon could associate with a small substitution of Si into TiO<sub>2</sub> lattice which leads to increase in the crystal size. The same size of different Si doping levels relates directly to formation energy [67]. No matter how much Si presents, only small amount of it is able to be doped into the TiO<sub>2</sub> lattice. This is in consistent with EDS results.

Table 5.2 XRD results of doped and undoped samples

Sample	Crystallite size (nm)	Lattice spacing, a for (101) plane	Interplanar spacing
TNTs	11.08	3.53	2.496
TNTs-0.1	24.02	3.52	2.489
TNTs-0.3	24.02	3.52	2.491

### 5.1.6 UV-visible absorption test

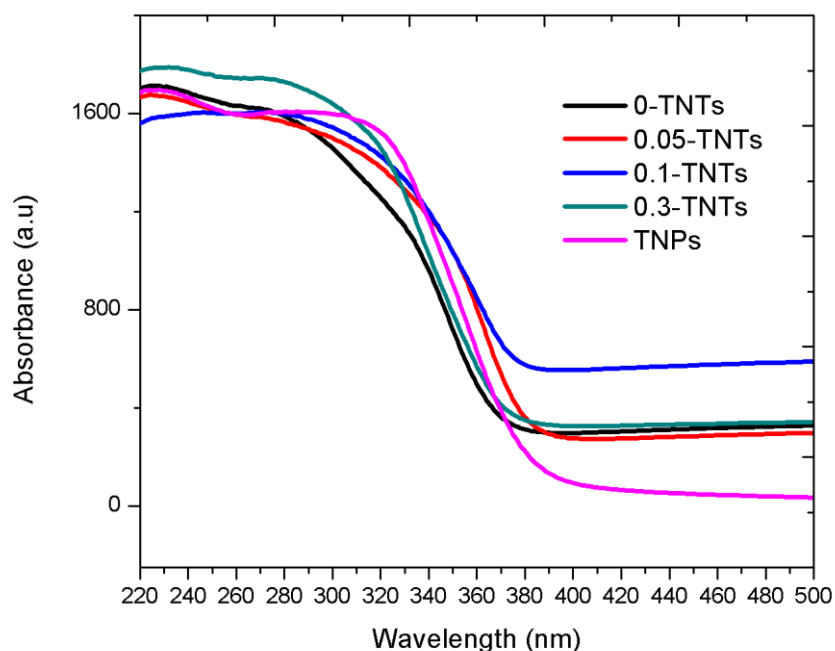


Fig 5.9. UV-vis absorption spectra of titania nanoparticles and titania nanotubes with the amount of Si doping in range of 0.01-0.3.

Fig 5.9 performs the UV-vis diffuse reflectance spectroscopy of undoped TiO<sub>2</sub> nanotubes and Si-doped TiO<sub>2</sub> nanotubes. It can be seen that there are two main groups with the band gap absorption edges at around 375 and 400 nm. The calculated band gap energies using the equation,  $E(\text{eV}) = 1239.95/\lambda$  (nm) [129] are listed in Table 5.3 and plotted in Fig 5.10. According to calculation, the band gap of TNPs is 3.22 eV which are typical for anatase TiO<sub>2</sub> photocatalytic band gap energy 3.2 eV [130]. After transformation into titania nanotubes, the band gap energy increases to the value of 3.26 eV. This blue shift could be attributed to quantum size effect of TiO<sub>2</sub> semiconductor in TNTs [131] due to very thin nanotube wall thickness. In the doped Si range of 0 to 0.1, the band gap energy of the TNTs decreases compared to TNPs and 0-TNTs. As reported by Yang et al., the substitutional Si to Ti-doped anatase results in the band gap narrowing about 0.25 eV [66]. Band gap reduction proves the interruption of Si to TNTs lattice. The red shift which is beneficial for visible light absorption

[132] could be achieved at the silicon doped lower amount than 0.1. Nevertheless, with large amount of Si in precursor, the band gap of photon excitation has no further narrowing but increasing. This is in good agreement with the simulation results of Shi et al [67].

Table 5.3 Band gap of the calcined samples at 450°C

Sample	Band gap energy (eV)
TNPs	3.22
0-TNTs	3.26
0.05-TNTs	3.15
0.1-TNTs	3.04
0.3-TNTs	3.24

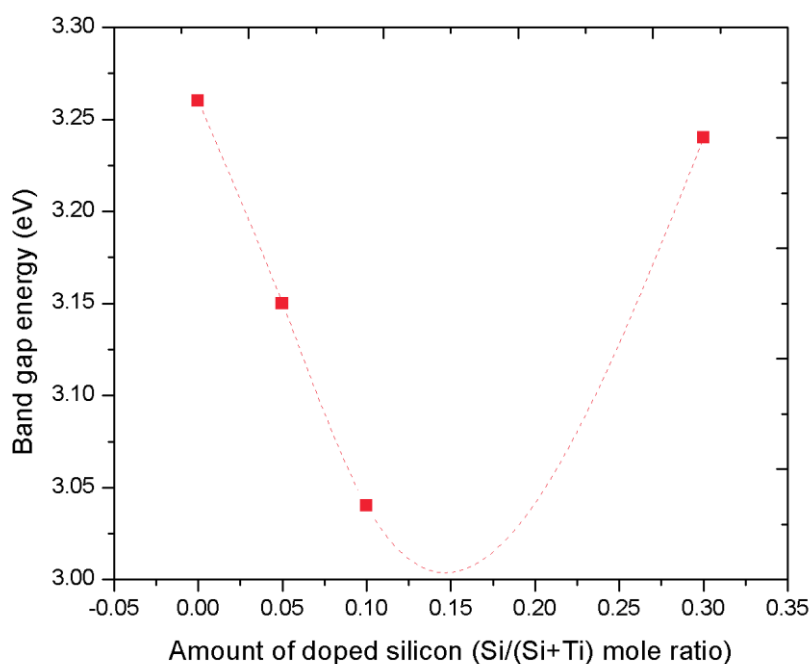


Fig 5.10. Band gap energy of different doped silicon amount

Introducing more Si into hydrothermal reactor would be a disadvantage because of high pressure released from the reaction between Si powder and NaOH. Too high pressure will suppress the dilution of Si. Thus, fewer amount of Si is successfully doped. Even if more silicon could be doped into titania, the band gap still increases corresponding to the simulation results of Shi et al [67]. It is expected that low amount of doped Si could exhibit a higher photocatalytic activity.

### 5.1.7 Methylene blue degradation test

For photocatalytic performance, undoped TNTs and doped TNTs were utilized to study the degradation of methylene blue (MB) absorption spectra. Based on the UV-vis absorption spectrum, the wavelength was chosen at 365 nm to define the distinctions between samples.

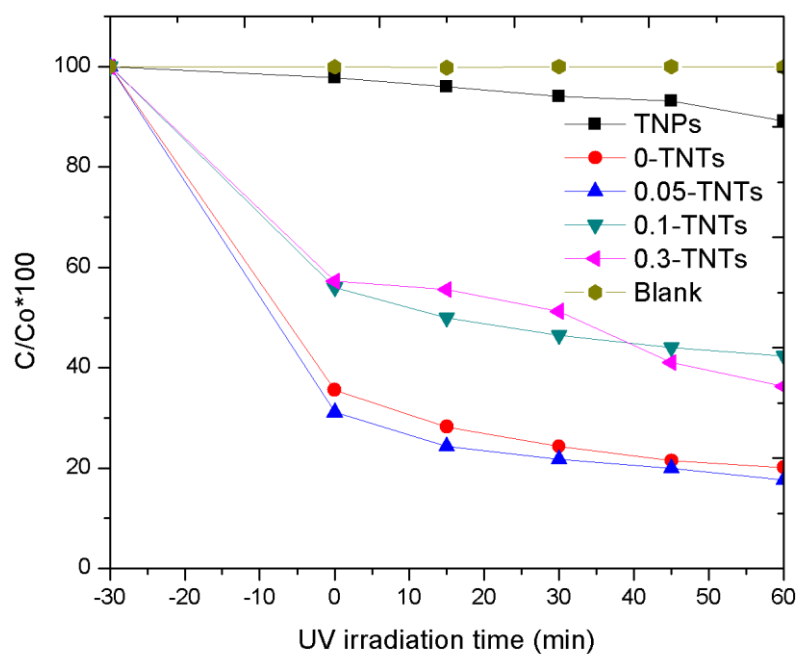


Fig 5.11. Photodegradation of MB using undoped TNTs and doped TNTs.

Fig 5.11 shows the variation of the MB concentration over the time under dark and UV illumination condition. The blank curve proves that without catalysts, methylene blue is barely degraded under UV-light. Dark absorption region is where the catalyst performs the ability to capture methylene blue without the energy from the light. Both catalytic activity and absorption ability are based on the particle size or surface area. Small particle size or high surface area would be beneficial for photodegradation of MB [133]. This is in good agreement with the XRD result that TNPs size is larger than 0.1, 0.3-TNTs and larger than 0-TNTs. The degradation ability also follows this order respectively. However, a suitable low amount doped Si could increase the photoactivity [30, 31]. According to XRD result and UV-vis spectrum, introducing Si enhances the crystallinity of anatase phase and the ability to absorb longer wavelength light which generate more electron and hole pairs for the oxidation of MB. The increase of hydroxyl group amount when doped with Si supports the dispersion of TiO<sub>2</sub> into water. As a result, dope with appropriate low amount of Si offers the highest photodegradation rate.

## 5.2 Composite of SiO<sub>2</sub> and Au on ZnO nanorods array

### 5.2.1 Morphology of ZnO nanorods on Zn foil using water

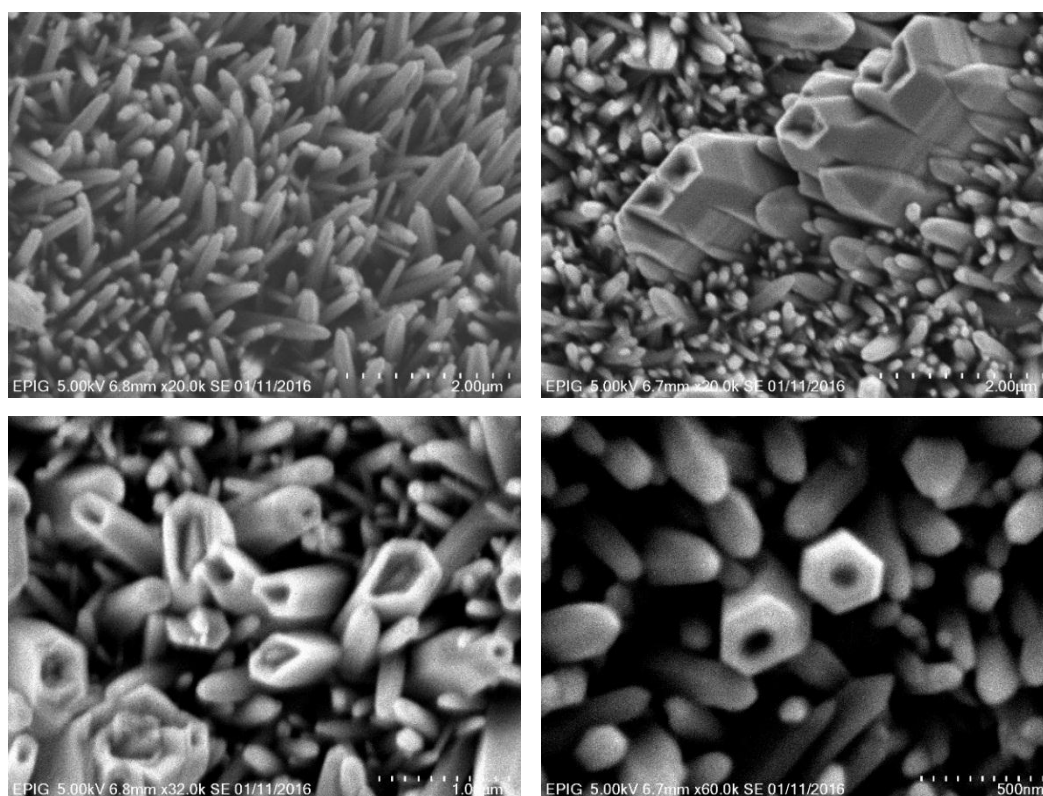


Fig 5.12. Different morphologies of nanorods on Zn foil using water

Fig 5.12 presents different morphologies of ZnO nanorods at distinct positions on Zn foil. According to the measurement by SEM, the nanorods array synthesized by using water is not uniform. Some areas on the foil have no formation of nanorods which means that DI water did not provide a homogeneous oxidation reagent. As observing from Fig 5.12, some rods are self-etched to form the nanotubes with different rates. The average length of the rods is approximately 1 micron and the diameter of the rods is about several nanometers. The non-uniform of this array is not preferable for the photocatalytic activity.

### 5.2.2 Investigating the optical properties of various SiO<sub>2</sub> layer thickness incorporating ZnO nanorods on Zn foil using KOH

#### 5.2.2.1 Morphology of ZnO nanorods on Zn foil using KOH

Fig 5.13 performs the morphology of ZnO nanorod arrays synthesized by using KOH before and after sputtering with SiO<sub>2</sub>. With more uniform nanorods everywhere on the Zn foil as visualized in Fig 5.13(a), hydrothermal treatment using KOH is a promising pathway to create the nanorods structure. The length and diameter of individual rods are several

micrometers and several hundred nanometers respectively. After depositing with thin SiO<sub>2</sub> layer on top, there was nothing changed in morphology as shown in Fig 5.14(b) because of the transparent characteristic of SiO<sub>2</sub> layer.

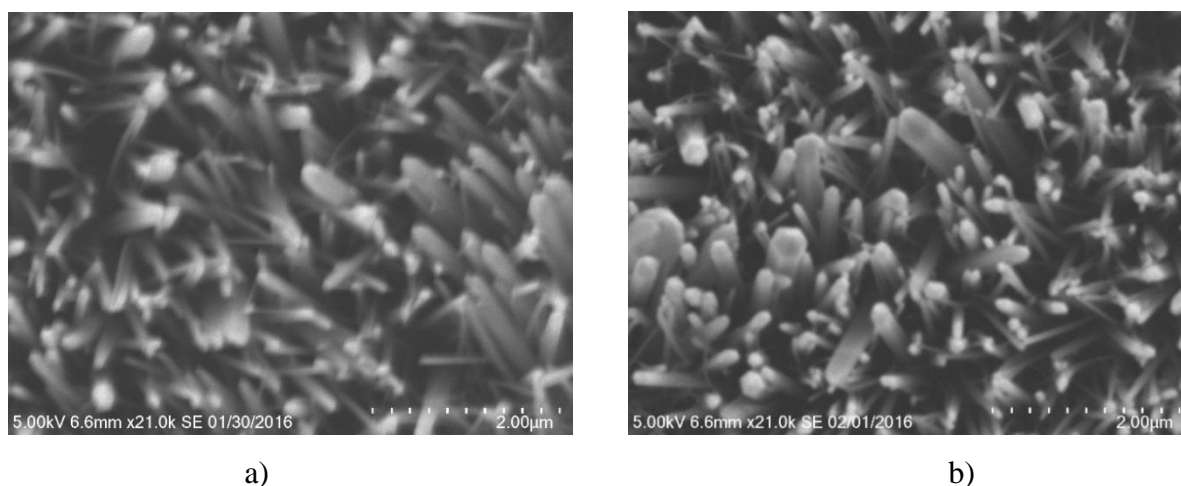


Fig 5.13. SEM image of a) Pure ZnO nanorods array on Zn foil b) ZnO nanorods array with SiO<sub>2</sub> thin layer on top

### 5.2.2.2 The Uv-vis absorption test

The UV-vis absorption spectra were recorded on four samples with different SiO<sub>2</sub> thickness as shown in Fig 5.14.

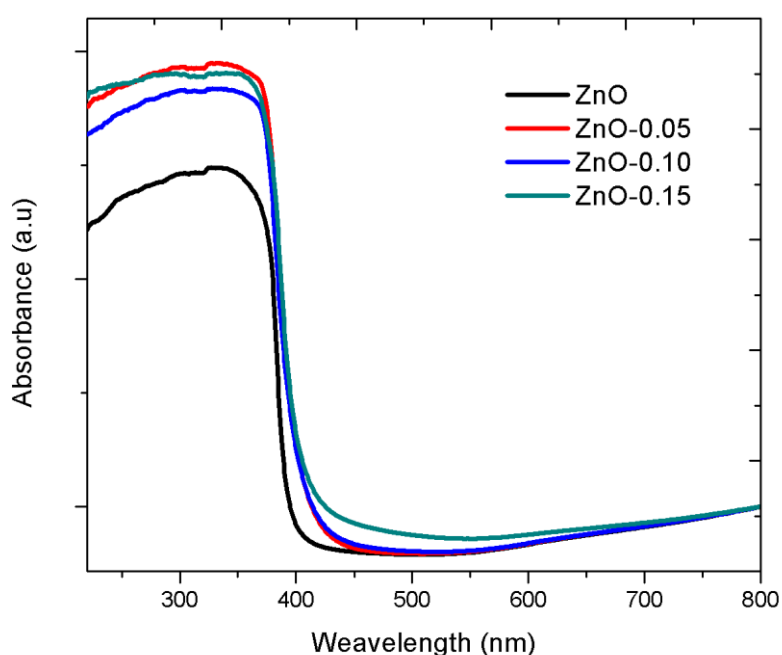


Fig 5.14. Uv-vis absorption spectra of ZnO nanorods with different SiO<sub>2</sub> thickness coating

According to literature review, SiO<sub>2</sub> layer is used for protection, passivation or dielectric layer with no obvious effect on absorption. However, there is a significant difference between

samples in our data points. Comparing to pristine ZnO nanorods, coating with SiO<sub>2</sub> layer induces the red shift from 400 nm to 430 nm. The absorption at 400-500 nm has trend to increase with the increase of SiO<sub>2</sub> thickness. This is due to the contribution of the dielectric properties of SiO<sub>2</sub> (refractive index  $n \sim 1.45$  larger than air). The efficiency of light absorption is enhanced as light has more chances to reflect back into the structure as sketched in Fig 5.15.

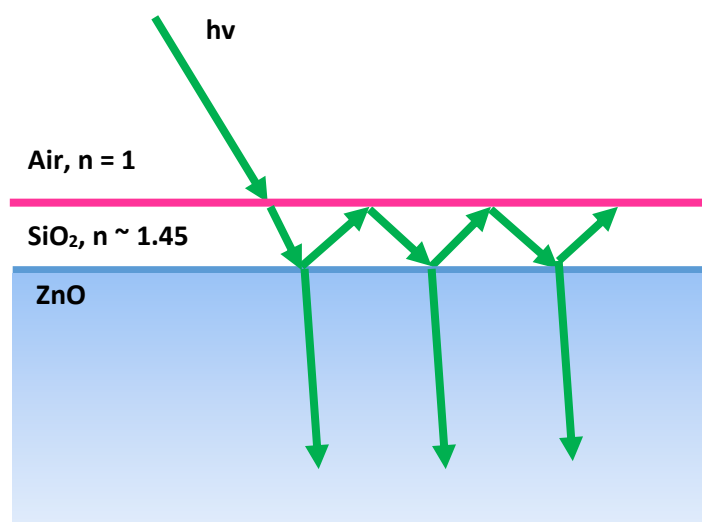


Fig 5.15. Illustration of light trap structure of SiO<sub>2</sub> coated sample.

### 5.2.2.3 Methylene blue degradation test

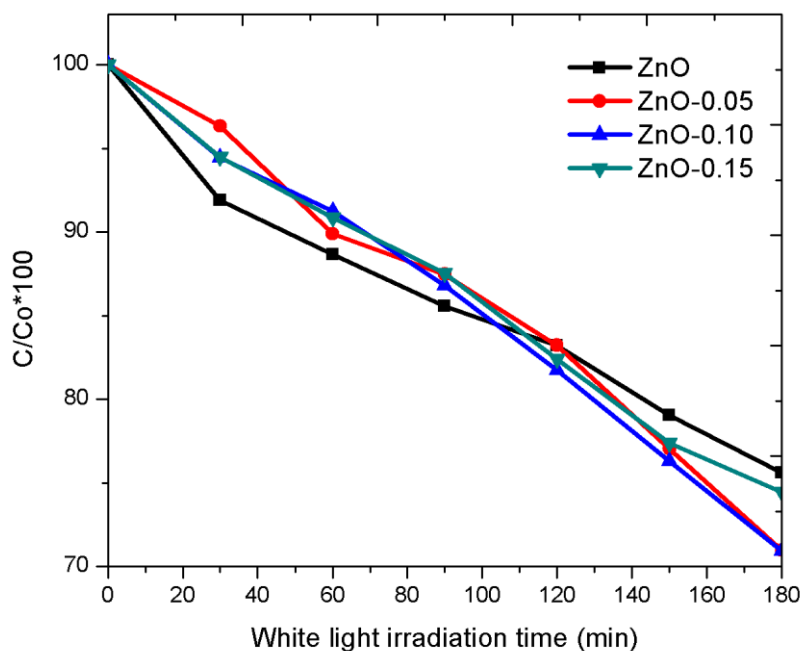


Fig 5.16. Methylene blue degradation under white light illumination of SiO<sub>2</sub> coated ZnO nanorods

Fig 5.16 illustrates degradation rate of pure ZnO and ZnO with different SiO<sub>2</sub> thickness on top under white light illumination. Basing on the Uv-vis absorption spectra in Fig 5.16, the difference at 400-500 nm leads to the choice of white light source. The aim of this test is to evaluate the photocatalytic activity of various SiO<sub>2</sub> thickness coated on ZnO nanorods. Although, there are not so much distinguishes between samples, but there is still a specialization for each sample. Obviously, pure ZnO nanorods is the least performance among samples after 180 illumination min. At the initial, pure ZnO nanorods show the highest degradation ability due to the fast electron to the interface of ZnO and methylene blue solution. However, after a period the rods got into contamination and corrosion resulting in the degradation over the time of photocatalyst. Three samples with SiO<sub>2</sub> coating exhibit a stable activity over the time. The lower degradation ability at the initial is because stimulated electrons have to tunnel through the SiO<sub>2</sub> layer to reach the methylene blue solution. Over the time, the degradation rate is still linear. This can be explained by the SiO<sub>2</sub> protection ability. On the other hand, in range of 5-10 nm, SiO<sub>2</sub> coated samples have better photoactivity. With too thick layer, energetic electrons from ZnO nanorods get harder to enter the methylene blue thus reduce the degradation ability.

### 5.2.3 Investigation the photocurrent properties of difference plasmonic configurations

#### 5.2.3.1 Morphology of ZnO nanorods before and after sputtering

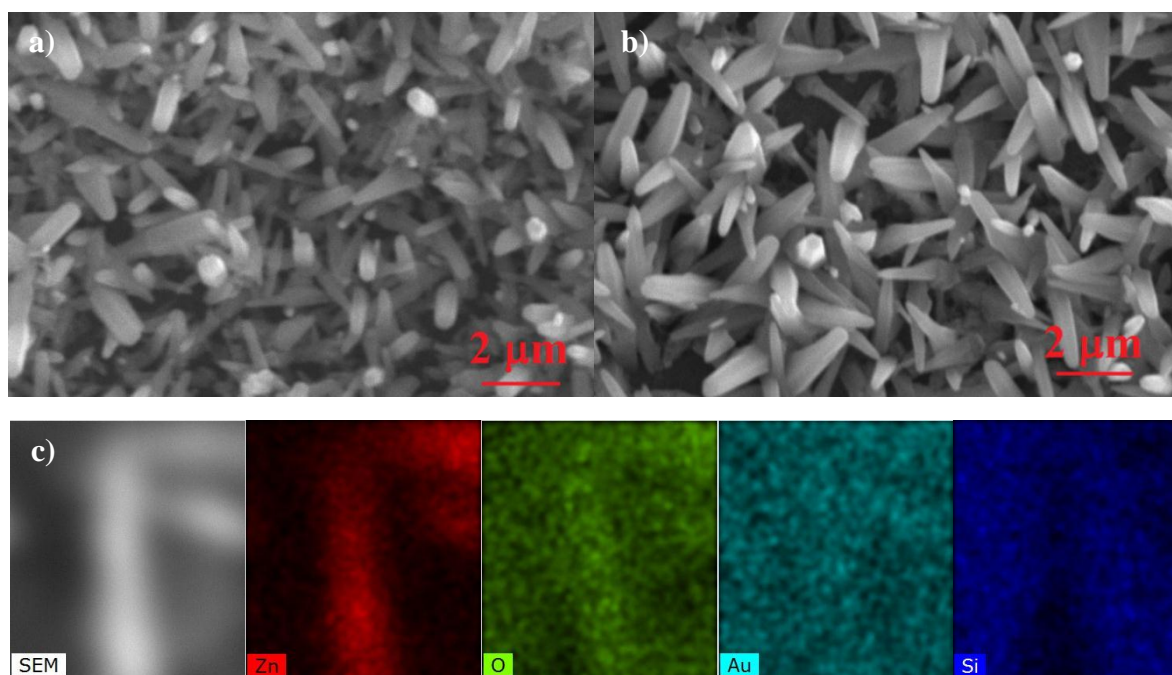


Fig 5.17. The SEM image of a) pure ZnO nanorods b) ZnO nanorods with SiO<sub>2</sub> and Au on top c) Mapping profile of ZnO-Au-SiO<sub>2</sub> sample on single rod.

Fig 5.17 shows the morphology of ZnO nanorods before and after sputtering along with mapping profile of single ZnO nanorod. In Fig 5.17(a), the SEM image collected for pure ZnO nanorods reveals that the length and the diameter of the rods are 1-2 micrometers and several hundred nanometers respectively. After sputtering with gold and silicon oxide as displayed in Fig 5.17(b), the SEM image of the sample is sharper than the pure one because of the conductive gold and transparent SiO<sub>2</sub>. A single horizontal ZnO nanorod on the ZnO-Au-SiO<sub>2</sub> sample was analyzed using EDS and mapping to detect the individual elements as shown in Fig 5.17 (c) and Fig 5.18. The ratio between Zn and O is roughly unity presenting for ZnO with small amount of gold (0.7 % .at) uniformly distribution (mapping). Nevertheless, the silicon and indium amount mostly come from the background ITO glass. Due to the nature and thin layer of silicon oxide (~5nm), it is hard to be detected through EDS.

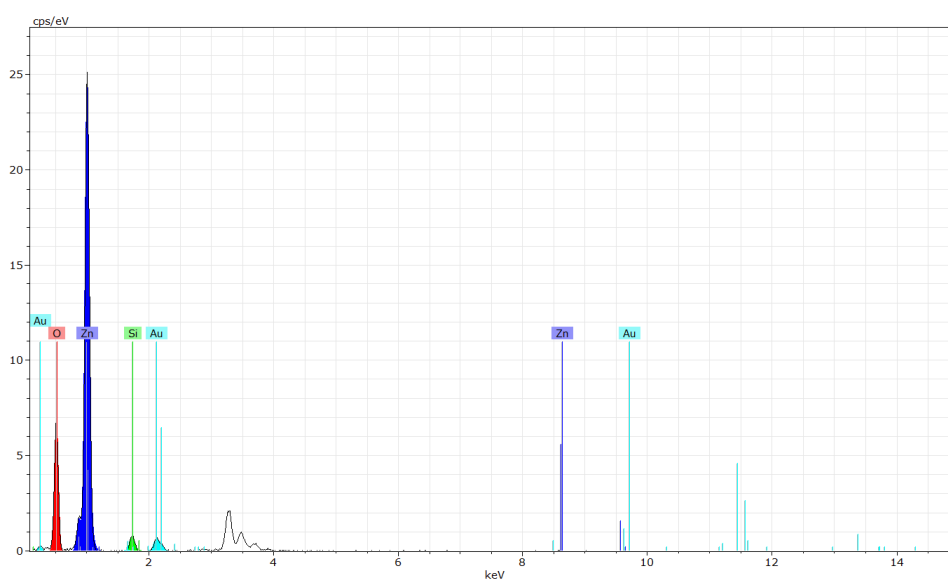


Fig 5.18. The EDS profiles of ZnO-Au-SiO<sub>2</sub> sample.

### 5.2.3.2 The UV-vis absorption test

Fig 5.19 displays the absorption profile of the samples before and after sputtering. In Fig 5.19(a), the absorption spectra of five as-prepared ZnO nanorods samples with the labels of future configuration have almost the same absorption in visible range. After sputtering (Fig 5.19(b)), the gold decorated samples exhibit strong absorption in visible light compared to pristine ZnO and ZnO-SiO<sub>2</sub> because of surface resonant plasmonic (SPR) effect. Depending on size and shape of the plasmonic structure, the SPR will have various behaviors [134]. The maximum peak is approximately 620 nm and there was no significant difference with the SiO<sub>2</sub> coated samples.

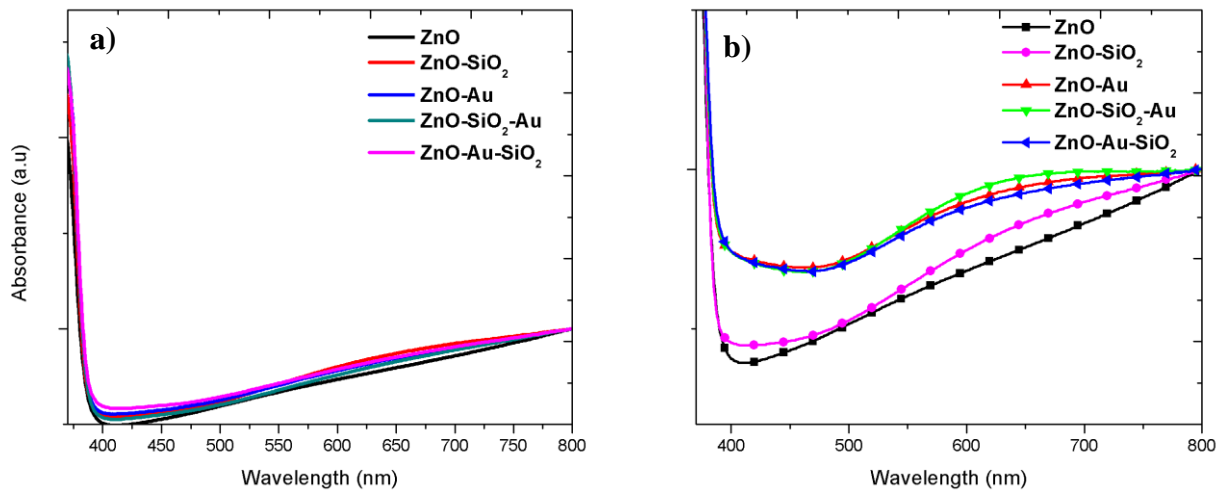


Fig 5.19. UV-VIS absorption spectra of a) 5 pure ZnO nanorods arrays b) after coating with different configurations.

### 5.2.3.3 PEC measurement

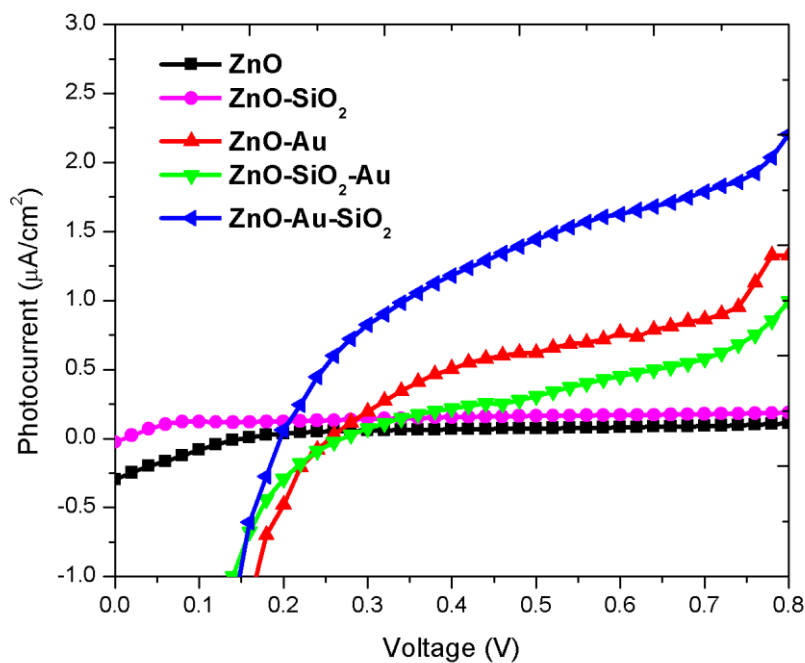


Fig 5.20. I-V curves of the samples under white light illumination

Fig 5.20 displays the photocurrent corresponding to bias voltage of the samples under white light illumination. Fig 5.21 shows the transient photocurrent of the samples at 0.5 V bias under white light illumination. Fig 5.22 performs the transient photocurrent of sample ZnO-Au-SiO<sub>2</sub> under 0.3, 0.5, 0.7 V bias under white light illumination.

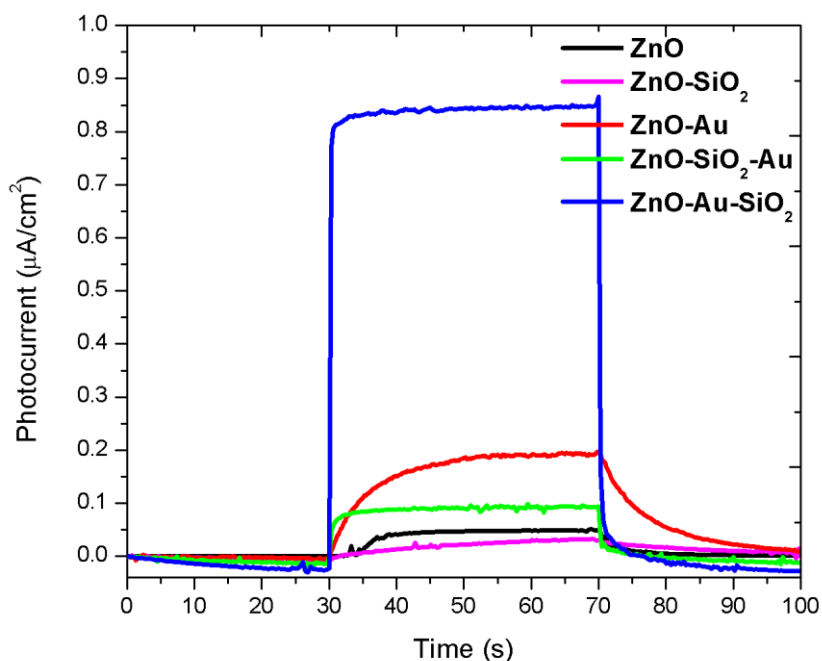


Fig 5.21. Transient photocurrent of the samples at 0.5V biasing under white light illumination.

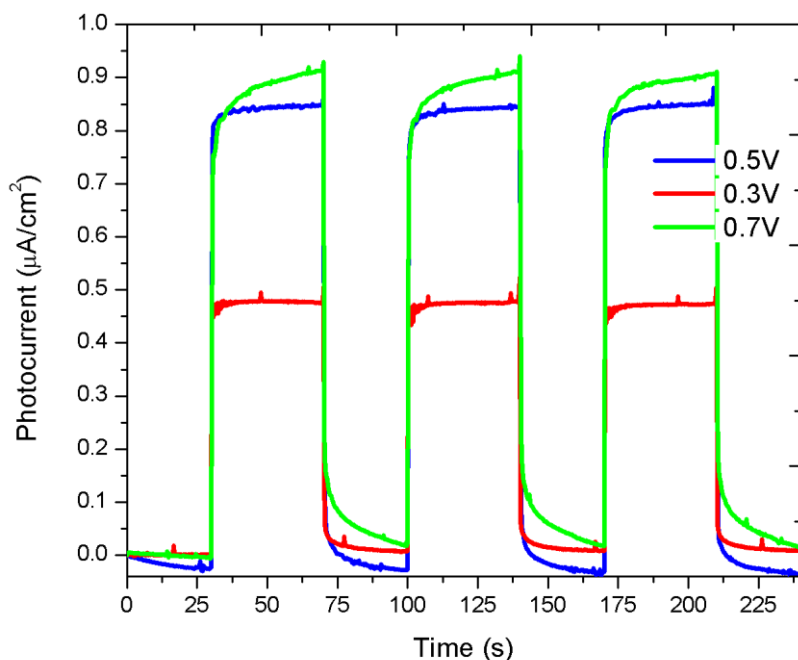


Fig 5.22. The transient photoresponse of ZnO-Au-SiO<sub>2</sub> sample at 0.3, 0.5, 0.7 V bias.

Due to the inertness and transparency, silicon oxide is utilized as a stabilizer, protecting layer, passive layer and dielectric layer. In the role of protecting layer, SiO<sub>2</sub> retards the interaction with oxygen resulting in the domination of electron-hole recombination [50]. This recombination significantly reduces the photocurrent. The same observation in our PEC

measurement is that the photoresponse of SiO<sub>2</sub> coated ZnO nanorods is lower than the pristine ZnO nanorods.

Gold nanoparticles coated ZnO nanorods is a well known plasmonic structure under visible irradiation. In UV, gold plays a role of electron trap which promotes the electron-hole pair separation [117]. Thus, gold incorporation increases the photocurrent significantly in sunlight region. Normally, when in touch with electrolyte, the difference in fermi level of semiconductor and electrolyte redox potential enables the band bending at the equilibrium where the space charge layer (SCL) is established [118]. In this space charge area, there would be a spatial electric field, which enhances the separation of charge carriers under light exciting. In addition to the bias voltage, incorporating metal, particularly gold with semiconductor like ZnO resulting in the Schottky barrier at the interface of contact causes the greater band bending [119]. Consequently, stronger spatial electric field is beneficial for electron-hole separation.

Because of the small portion of UV in white light and sunlight, the main attribution for the enhancement of photoresponse is the visible region where the surface plasmonic resonant effect (SPR) dominates. SPR effect promotes the rates of photocatalyst reactions by concentration of charge carriers through three non-mutually exclusive energy-transfer mechanisms, SPR-mediated charge injection from metal to semiconductor, near-field electromagnetic and scattering mechanisms. However, scattering mechanism can be ruled out of this discussion because it only affects if the structure of plasmonic metal is larger than 50 nm [124]. The charge injection mechanism is definitely the key for the effective water splitting process. As observed in Fig 5.19(b), the maximum absorption of gold decorated ZnO nanorods is approximately 620 nm, which stimulates the resonant electron up to 2eV. The electron affinity of ZnO and work function of Au are 4.35 eV and 5.1 eV respectively resulting in the Schottky barrier at 0.75 eV as shown in Fig 5.23. The energetic electrons have more than enough potential to jump up through Schottky barrier into ZnO conduction band. The near-field electromagnetic mechanism is described as the interaction of the semiconductor with the strong SPR-induced electric field localized nearby at the metallic nanostructure [8]. When a semiconductor is in contact with photo-excited plasmonic structure, the intense field will accelerate the rate of electron-hole pair formation. All superior effects of gold nanoparticles loading contributed for the great enhancement in photocurrent under white light irradiation compared to pristine ZnO nanorods as presented in Fig 5.20.

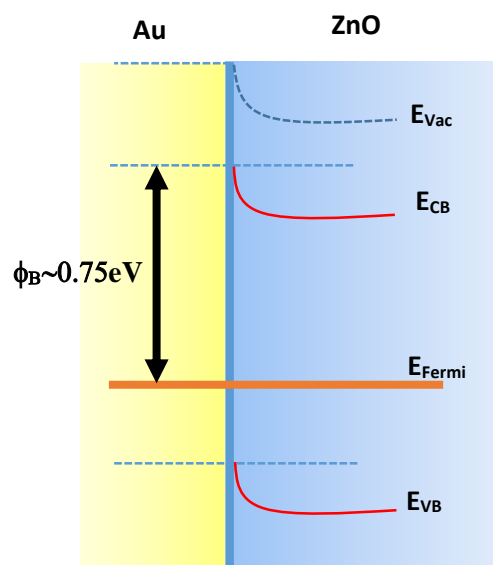


Fig 5.23. Band diagram of ZnO-Au sample.

In ZnO-SiO<sub>2</sub>-Au configuration, SiO<sub>2</sub> layer acts as insulator between gold nanoparticles and ZnO nanorods. The SCL is therefore, narrowed leading to less intensive spatial electric field. This insulator also weakens the near field electromagnetic, which significantly depresses the electron-hole separation. On the other hand, under visible light irradiation, the energetic electron still can tunnel through the SiO<sub>2</sub> layer to inject in to the ZnO nanorods as illustrated in Fig 5.24. These are reasons for the lower photocurrent of ZnO-SiO<sub>2</sub>-Au than only gold decorated ZnO nanorods but still higher than pristine ZnO nanorods.

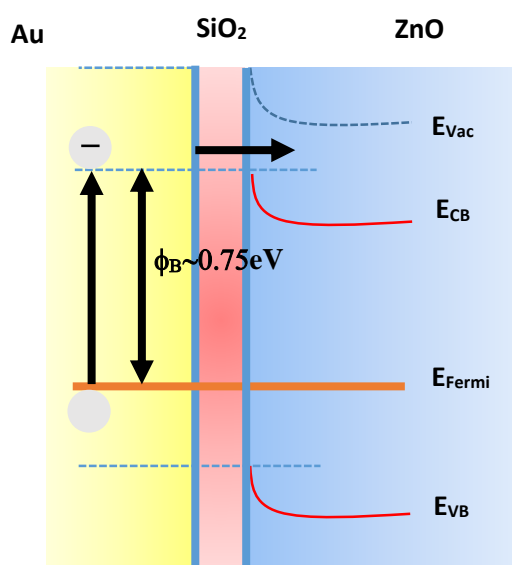


Fig 5.24. Band diagram of ZnO-SiO<sub>2</sub>-Au sample.

Interestingly, ZnO-Au-SiO<sub>2</sub> configuration performed an outstanding photoresponse compared to the others. This configuration is simply ZnO-Au with a thin layer of dielectric as

outer shell. Beside the positive effects of gold nanoparticles decorated ZnO nanorods, there are several factors contributing for the high photocurrent density of ZnO-Au-SiO<sub>2</sub>. The gold plasmonic structure alone has the possibility to interact with the electrolyte components that decreases the amount of energetic electrons into the ZnO nanorods. SiO<sub>2</sub> layer is able to inhibit the electron in conduction state interacting with the electrolyte components. Thus, SiO<sub>2</sub> not only increases the injection efficiency but the presence of negative charge localized in SiO<sub>2</sub> film also creates an effective electron transport channel in the ZnO backbone to suppress the carriers recombination by inducing a formation of electron depletion layer and band up bending at the nanorod surface [47] as shown in Fig 5.25. Using the same plasmonic configuration, the simulation results of Xu et al. group indicated that semiconductor-plasmonic metal-dielectric layer exhibits more intensive electric field at the semiconductor/plasmonic metal interface and deeper penetration into the semiconductor than the others [47]. Furthermore, the higher refractive index of dielectric layer than that of electrolyte establishes a light trap structure (Fig 5.15) which lengthens the pathway of incoming light. Therefore, it enhances the absorption opportunities of semiconductor and plasmonic metal leading to better electron-hole separation.

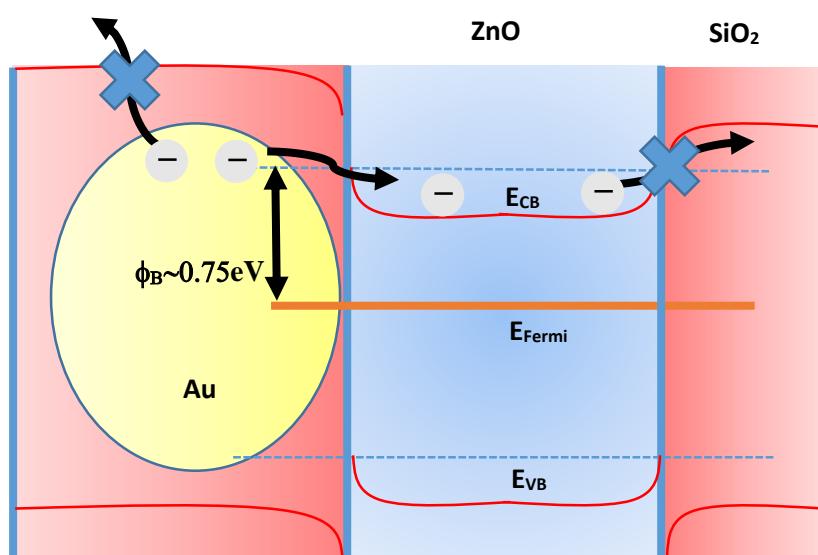


Fig 5.25. Band diagram of ZnO-Au-SiO<sub>2</sub> sample.

It's meaningful to have the fast photoresponse in some applications [135]. It can be seen from Fig 5.26 that ZnO-Au rising and decaying time is very large compared to ZnO-SiO<sub>2</sub>-Au and ZnO-Au-SiO<sub>2</sub>. This delaying is due to the recombination of photoexcited holes recombine with electrons in traps states [48]. In the experiment of Murphy et al, the extremely deep hole trap in wide band gap semiconductor such as ZnO attributes for slow photoresponse [136].

They also pointed out that the passivation with SiO<sub>2</sub> significantly depresses the density of deep traps at the ZnO surface. This is in good agreement with our data point that the sample with SiO<sub>2</sub> passivation layer perform very sharp response to light.

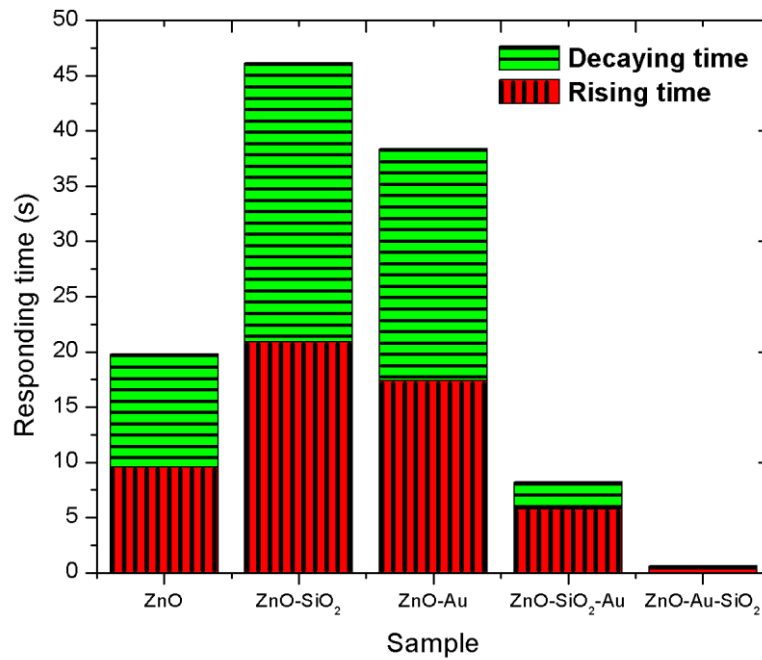


Fig 5.26. The photoresponse time of five samples in term of decaying and rising time and diagram of ZnO-Au-SiO<sub>2</sub> sample.

In conclusion, ZnO-Au-SiO<sub>2</sub> configuration exhibits an excellent photocurrent, fast photoresponse and highly stable during PEC measurement at different voltage biases as illustrated in Fig 5.22.

## CHAPTER 6. CONCLUSIONS AND PROSPECTS

All the modified catalysts have the positive effect on the photocatalytic performance. Though there are some limitations needed to avoid in next catalytic processing, these catalysts are promising for the reality photocatalytic application.

### 6.1 Achievements

#### 6.1.1 TiO<sub>2</sub> approach

In this study, silicon was in-situ doped on TiO<sub>2</sub> nanotubes by a simple hydrothermal method. Various amount of Si doping have been investigated. XRD results indicate that the size between undoped and doped sample varies from 11.08 nm to 24.02 nm. Higher crystallinity of anatase TiO<sub>2</sub> is observed after introducing Si. Especially, red shift in UV-absorption spectrum clarified the interruption of Si into TiO<sub>2</sub> lattice. The band gap energy decreases significantly from 3.26 eV (undope) to 3.04 eV (dope). The photodegradation result is consistent with XRD and UV-vis absorption test that low amount of doped Si (<5%) is beneficial for photocatalytic activity. The large surface area and high activity of the Si modified titania nanotubes powder attributed for the efficient degradation of methylene blue.

#### 6.1.2 ZnO approach

By simple hydrothermal and sputtering method, the effect of SiO<sub>2</sub> layer on the photocatalytic performance of ZnO nanorods was evaluated. An increase in absorption spectra was observed when increased the thickness of SiO<sub>2</sub>. Though, the improvement was not considerable, SiO<sub>2</sub> layer's function suggests a new role when it is reasonably integrated into other structure (plasmonic structure).

In this work, almost every possible photocatalytic enhancing mechanisms of gold decorated ZnO nanorods have been successfully reviewed in both uv and visible region such as (1) acting as electron trap site in Uv region, (2) enhancing the band bending resulting in the strong spatial electric field, (3) SPR-mediated charge injection from metal to semiconductor, (4) near-field electromagnetic and (5) scattering mechanisms. The presence of thin dielectric layer between gold and ZnO nanorods depresses the response to visible light owing to the near field magnetic inhibition induced by passivation effect. Among those configurations, ZnO-Au-SiO<sub>2</sub> exhibits superior photoresponse ascribed to (1) SiO<sub>2</sub> intensified SPR-mediated hot electron injection due to its higher dielectric index, (2) light trapping structure, (3) effective electron transportation channel through ZnO backbone. Additionally, SiO<sub>2</sub> passivates the trap site at the surface of semiconductor resulting in faster photoresponse. By using solar water splitting as

platform to elucidate the influences of gold and SiO<sub>2</sub> layer on 1D semiconductor, this work strengthens the understanding on the design engineering for high performance photocatalysts of solar to fuel energy conversion.

## **6.2 Prospects**

### **6.2.1 TiO<sub>2</sub> approach**

Though only small amount of silicon could be doped into titania lattice no matter how much it presents, the performance TNTs after doping with Si was improved. If more time is spent, the optimal amount of silicon could be found which will enhance the photocatalytic properties significantly. One more possibility is the balance between the doping amount and the level of liquid inside the thermal chamber. Higher amount of silicon contributes the higher pressure which can be reduced by decreasing the level of the liquid. The amount of Si doping therefore could be increased.

Handling nanopowder as well as using it is not simple. But, this material is suitable for conversion at gas phase and pollutant degradation because of its high surface area and the exposing of active sites.

### **6.2.2 ZnO approach**

If the synthesis condition is strictly followed, the repeatability is very high. More time need to be spent for the optimization the fabrication process for this ZnO nanorods array which should be uniform.

Synthesis ZnO nanorods on Zn foil is simpler than on ITO glass because of the seed layer step. Nevertheless, the inertness of ITO glass enables more application of ZnO nanorods than Zn foil.

The coating of SiO<sub>2</sub> and Au layer on ZnO opened a premise for tailoring technique on 1D nanostructure enhancing the desired effect for a specific process.

## References

- [1] U. S. E. I. Administration, *Annual energy outlook 2015*, 2015, EIA.
- [2] S. C. Roy, O. K. Varghese, M. Paulose, and C. A. Grimes, "Toward Solar Fuels: Photocatalytic Conversion of Carbon Dioxide to Hydrocarbons". *American Chemical Society Nano*, vol. 4, pp. 1259-1278, 2010.
- [3] J. A. Turner, "A Realizable Renewable Energy Future". *Science*, vol. 285, pp. 687-689, 1999.
- [4] G. Centi and S. Perathoner, "Towards solar fuels from water and CO<sub>2</sub>". *ChemSusChem*, vol. 3, no. 2, pp. 195-208, 2010.
- [5] G. Liu, N. Hoivik, K. Wang, and H. Jakobsen, "Engineering TiO<sub>2</sub> nanomaterials for CO<sub>2</sub> conversion/solar fuels". *Solar Energy Materials and Solar Cells*, vol. 105, pp. 53-68, 2012.
- [6] P. D. Tran, L. H. Wong, J. Barber, and J. S. C. Loo, "Recent advances in hybrid photocatalysts for solar fuel production". *Energy & Environmental Science*, vol. 5, no. 3, pp. 5902, 2012.
- [7] Fujishima and Honda, "Electrochemical Photolysis of water at a semiconductor electrode". *Nature*, vol. 238, pp. 37, 1972.
- [8] S. Linic, P. Christopher, and D. B. Ingram, "Plasmonic-metal nanostructures for efficient conversion of solar to chemical energy". *Nature Materials*, vol. 10, pp. 911, 2011.
- [9] M. Mikkelsen, M. Jørgensen, and F. C. Krebs, "The teraton challenge. A review of fixation and transformation of carbon dioxide". *Energy & Environment Science*, vol. 3, no. 1, pp. 43-81, 2010.
- [10] N. Liu, X. Chen, J. Zhang, and J. W. Schwank, "A review on TiO<sub>2</sub>-based nanotubes synthesized via hydrothermal method: Formation mechanism, structure modification, and photocatalytic applications". *Catalysis Today*, vol. 225, pp. 34-51, 2014.
- [11] J. Saha, A. Mitra, A. Dandapat, and G. De, "TiO<sub>2</sub> nanoparticles doped SiO<sub>2</sub> films with ordered mesopore channels: a catalytic nanoreactor". *Dalton Transactions*, vol. 43, no. 13, pp. 5221-9, 2014.
- [12] M. Anpo, "Use of visible light. Second-generation titanium oxide photocatalysts prepared by the application of an advanced metal ion-implantation method". *Pure and Applied Chemistry*, vol. 72, pp. 1787-1792, 2000.
- [13] A. Fuerte, M. D. Hernández-Alonso, A. J. Maira, A. Martínez-Arias, M. Fernández-García, J. C. Conesa, and J. Soria, "Visible light-activated nanosized doped-TiO<sub>2</sub> photocatalysts". *Chemical Communications*, vol., no. 24, pp. 2718-2719, 2001.
- [14] H. Yamashita, M. Harada, J. Misaka, M. Takeuchi, Y. Ichihashi, F. Goto, M. Ishida, T. Sasaki, and M. Anpo, "Application of ion beam techniques for preparation of metal ion-implanted TiO<sub>2</sub> thin film photocatalyst available under visible light irradiation: Metal ion-implantation and ionized cluster beam method". *Journal of Synchrotron Radiation*, vol. 8, pp. 569-571, 2001.

- [15] L. Xiaojing, "Titanium Oxide Modified by Plasma and Red Shift of Its Response Spectrum". *Progress in Chemistry*, vol. 19, 2007.
- [16] T. Ohno, M. Akiyoshi, T. Umehayashi, K. Asaib, T. Mitsui, and M. Matsumura, "Photocatalytic Activity of S-doped TiO<sub>2</sub> Photocatalyst under Visible Light". *Applied Catalysis A: General*, vol. 265, pp. 115–121, 2004.
- [17] Y. Liu, X. Chen, J. Li, and C. Burda, "Photocatalytic degradation of azo dyes by nitrogen-doped TiO<sub>2</sub> nanocatalysts". *Chemosphere*, vol. 61, no. 1, pp. 11-8, 2005.
- [18] T. Hirai, K. Suzuki, and I. Komasa, "Preparation and Photocatalytic Properties of Composite CdS Nanoparticles–Titanium Dioxide Particles". *Journal of Colloid and Interface Science*, vol. 244, no. 2, pp. 262-265, 2001.
- [19] D. Chatterjee and A. Mahata, "Demineralization of organic pollutants on the dye modified TiO<sub>2</sub> semiconductor particulate system using visible light". *Applied Catalysis B: Environmental*, vol. 33, pp. 119–125, 2001.
- [20] H. Irie, Y. Watanabe, K. Hashimoto, Y. Watanabe, and K. Hashimoto, "Nitrogen-Concentration Dependence on Photocatalytic Activity of TiO<sub>2</sub>-xN<sub>x</sub> Powders". *Journal of Physical Chemistry B*, vol. 107, pp. 5483-5486, 2003.
- [21] J. Su, X. Zou, and J.-S. Chen, "Self-modification of titanium dioxide materials by Ti<sup>3+</sup> and/or oxygen vacancies: new insights into defect chemistry of metal oxides". *Royal Society of Chemistry Advances*, vol. 4, no. 27, pp. 13979, 2014.
- [22] K. Y. Jung and S. B. Park, "Enhanced photoactivity of silica-embedded titania particles prepared by sol–gel process for the decomposition of trichloroethylene". *Applied Catalysis B: Environmental*, vol. 25, pp. 249–256, 2000.
- [23] M. Hirano, K. Ota, and H. Iwata, "Direct Formation of Anatase (TiO<sub>2</sub>)/Silica (SiO<sub>2</sub>) Composite Nanoparticles with High Phase Stability of 1300 °C from Acidic Solution by Hydrolysis under Hydrothermal Condition". *Chemistry of Materials*, vol. 16, pp. 3725-3732, 2004.
- [24] S. Iwamoto, and M. Inoue, "XANES and XPS Study of Silica-Modified Titanias Prepared by the Glycothermal Method". *Chemical of Materials*, vol. 17, pp. 650-655, 2005.
- [25] C. Xie, Z. Xu, Q. Yang, B. Xue, Y. Du, and J. Zhang, "Enhanced photocatalytic activity of titania–silica mixed oxide prepared via basic hydrolyzation". *Materials Science and Engineering: B*, vol. 112, no. 1, pp. 34-41, 2004.
- [26] Y. Li and C.-Y. Wu, "Role of Moisture in Adsorption, Photocatalytic Oxidation, and Reemission of Elemental Mercury on a SiO<sub>2</sub>-TiO<sub>2</sub> Nanocomposite". *Environmental Science & Technology*, vol. 40, pp. 6444-6448, 2006.
- [27] S. Iwamoto, and M. Inoue, "XANES and XPS Study of Silica-Modified Titanias Prepared by the Glycothermal Method". *Chem. Mater.*, vol. 17, pp. 650-655, 2005.
- [28] K. Y. Jung and S. B. Park., "Enhanced photoactivity of silica-embedded titania particles prepared by sol–gel process for the decomposition of trichloroethylene". *Applied Catalysis B: Environmental*, vol. 25, pp. 249–256, 2000.

- [29] G. Calleja, D. P. Serrano, R. Sanz, and P. Pizarro, "Mesoporous SiO<sub>2</sub>-doped TiO<sub>2</sub> with enhanced thermal stability prepared by a soft-templating sol-gel route". *Microporous and Mesoporous Materials*, vol. 111, no. 1-3, pp. 429-440, 2008.
- [30] Bao, N. Wei, Z. Ma, Z. Liu, and G. F. Yin, "Si-doped mesoporous TiO<sub>2</sub> continuous fibers: preparation by centrifugal spinning and photocatalytic properties". *Journal of Hazardous Materials* vol. 174, no. 1-3, pp. 129-36, 2010.
- [31] S. M. Oh, S. S. Kim, J. E. Lee, T. Ishigaki, and D. W. Park, "Effect of additives on photocatalytic activity of titanium dioxide powders synthesized by thermal plasma". *Thin Solid Films*, vol. 435, pp. 252-258, 2003.
- [32] T. Kogure and T. Umezawa, "Formation of TiO<sub>2</sub>(B) Nanocrystallites in Sol-Gel-Derived SiO<sub>2</sub>-TiO<sub>2</sub> Film". *Journal of the American Ceramic Society*, vol. 82, pp. 3248-50, 1999.
- [33] Zhe Ding, Xijun Hu, Gao Q. Lu, Po-Lock Yue, and P. F. Greenfield, "Novel Silica Gel Supported TiO<sub>2</sub> Photocatalyst Synthesized by CVD Method". *Langmuir*, vol. 16, pp. 6216-6222, 2000.
- [34] X. Yan, J. He, D. G. Evans, X. Duan, and Y. Zhu, "Preparation, characterization and photocatalytic activity of Si-doped and rare earth-doped TiO<sub>2</sub> from mesoporous precursors". *Applied Catalysis B: Environmental*, vol. 55, no. 4, pp. 243-252, 2005.
- [35] C. Kang, L. Jing, T. Guo, H. Cui, J. Zhou, and H. Fu, "Mesoporous SiO<sub>2</sub>-Modified Nanocrystalline TiO<sub>2</sub> with High Anatase Thermal Stability and Large Surface Area as Efficient Photocatalyst". *The Journal of Physical Chemistry C*, vol. 113, pp. 1006-1013, 2009.
- [36] R. Jin, Z. Wu, Y. Liu, B. Jiang, and H. Wang, "Photocatalytic reduction of NO with NH<sub>3</sub> using Si-doped TiO<sub>2</sub> prepared by hydrothermal method". *Journal of Hazardous Materials*, vol. 161, no. 1, pp. 42-8, 2009.
- [37] A. Chemseddine and T. Moritz, "Nanostructuring Titania: Control over Nanocrystal Structure, Size, Shape, and Organization". *European Journal of Inorganic Chemistry*, vol., pp. 235-245, 1999.
- [38] O. Tabata, "Anisotropic etching of silicon in (CH<sub>3</sub>)<sub>3</sub>NOH solutions". *IEEE*, vol. 480, no. 11, pp. 811, 1991.
- [39] G.-S. Chung, "Anisotropic Etching Characteristics of Si in Tetramethylammonium Hydroxide : Isopropyl Alcohol : Pyrazine Solutions". *Journal of the Korean Physical Society*, vol. 46, pp. 1152~1156, 2005.
- [40] C. L. Hsu and S. J. Chang, "Doped ZnO 1D nanostructures: synthesis, properties, and photodetector application". *Small*, vol. 10, no. 22, pp. 4562-85, 2014.
- [41] C. O. Chey, *Synthesis of ZnO and transition metals doped ZnO nanostructures, their characterization and sensing applications*, in *Physical Electronics and Nanotechnology Department of Science and Technology* 2015, Campus Norrköping, Linköping University: SE-601-74 Norrköping, Sweden.

- [42] S. K. Kansal, M. Singh, and D. Sud, "Studies on TiO<sub>2</sub>/ZnO photocatalysed degradation of lignin". *Journal of Hazardous Materials*, vol. 153, no. 1-2, pp. 412-7, 2008.
- [43] M. Samadi, M. Zirak, A. Naseri, E. Khorashadizade, and A. Z. Moshfegh, "Recent progress on doped ZnO nanostructures for visible-light photocatalysis". *Thin Solid Films*, vol., 2016.
- [44] N. Ekthammathat, T. Thongtem, A. Phuruangrat, and S. Thongtem, "Photoluminescence of Hexagonal ZnO Nanorods Hydrothermally Grown on Zn Foils in KOH Solutions with Different Values of Basicity". *Journal of Nanomaterials*, vol. 2013, pp. 1-4, 2013.
- [45] J. Lu, H. Wang, D. Peng, T. Chen, S. Dong, and Y. Chang, "Synthesis and properties of Au/ZnO nanorods as a plasmonic photocatalyst". *Physica E: Low-dimensional Systems and Nanostructures*, vol. 78, pp. 41-48, 2016.
- [46] W. Chen, Y. Lu, W. Dong, Z. Chen, and M. Shen, "Plasmon mediated visible light photocurrent and photoelectrochemical hydrogen generation using Au nanoparticles/TiO<sub>2</sub> electrode". *Materials Research Bulletin*, vol. 50, pp. 31-35, 2014.
- [47] Z. Xu, Y. Lin, M. Yin, H. Zhang, C. Cheng, L. Lu, X. Xue, H. J. Fan, X. Chen, and D. Li, "Understanding the Enhancement Mechanisms of Surface Plasmon-Mediated Photoelectrochemical Electrodes: A Case Study on Au Nanoparticle Decorated TiO<sub>2</sub> Nanotubes". *Advanced Materials Interfaces*, vol. 2, no. 13, pp. n/a-n/a, 2015.
- [48] Y. C. Pu, G. Wang, K. D. Chang, Y. Ling, Y. K. Lin, B. C. Fitzmorris, C. M. Liu, X. Lu, Y. Tong, J. Z. Zhang, Y. J. Hsu, and Y. Li, "Au nanostructure-decorated TiO<sub>2</sub> nanowires exhibiting photoactivity across entire UV-visible region for photoelectrochemical water splitting". *Nano Lett*, vol. 13, no. 8, pp. 3817-23, 2013.
- [49] S. K. Medda, S. De, and G. De, "Synthesis of Au nanoparticle doped SiO<sub>2</sub>-TiO<sub>2</sub> films: tuning of Au surface plasmon band position through controlling the refractive index". *Journal of Materials Chemistry*, vol. 15, no. 32, pp. 3278, 2005.
- [50] P. Mulvaney, L. M. Liz-Marzán, M. Giersig, and T. Ung, "Silica encapsulation of quantum dots and metal clusters". *Journal of Materials Chemistry*, vol. 10, no. 6, pp. 1259-1270, 2000.
- [51] X. Gao and I. E. Wachs, "Titania-silica as catalyst: molecular structural characteristics and physico-chemical properties". *Catalysis Today*, vol. 51, pp. 233-254, 1999.
- [52] C. Anderson and A. J. Bard, "An Improved Photocatalyst of TiO<sub>2</sub>/SiO<sub>2</sub> Prepared by a Sol-Gel Synthesis". *The Journal of Physical Chemistry A*, vol. 99, pp. 9882-9885, 1999.
- [53] D. Wu, F. Mao, Z. Yang, S. Wang, and Z. Zhou, "Silicon and aluminum co-doping of titania nanoparticles: Effect on thermal stability, particle size and photocatalytic activity". *Materials Science in Semiconductor Processing*, vol. 23, pp. 72-77, 2014.
- [54] P. Periyat, K. V. Baiju, P. Mukundan, P. K. Pillai, and K. G. K. Warriar, "High temperature stable mesoporous anatase TiO<sub>2</sub> photocatalyst achieved by silica addition". *Applied Catalysis A: General*, vol. 349, no. 1-2, pp. 13-19, 2008.

- [55] N. Ma, X. Quan, Y. Zhang, S. Chen, and H. Zhao, "Integration of separation and photocatalysis using an inorganic membrane modified with Si-doped TiO<sub>2</sub> for water purification". *Journal of Membrane Science*, vol. 335, no. 1-2, pp. 58-67, 2009.
- [56] J. Saha, A. Mitra, A. Dandapat, and G. De, "TiO<sub>2</sub> nanoparticles doped SiO<sub>2</sub> films with ordered mesopore channels: a catalytic nanoreactor". *Dalton Trans*, vol. 43, no. 13, pp. 5221-9, 2014.
- [57] Erik Pitoniak, Chang-YuWu, Kevin Powers , D. Londeree, W. Sigmund, David Mazyck, and J.-C. Bonzongo, "Nanostructured silica-gel doped with TiO<sub>2</sub> for mercury vapor control". *Journal of Nanoparticle Research*, vol. 5, pp. 281–292, 2003.
- [58] M. Sun, X. Zhang, J. Li, X. Cui, D. Sun, and Y. Lin, "Thermal formation of silicon-doped TiO<sub>2</sub> thin films with enhanced visible light photoelectrochemical response". *Electrochemistry Communications*, vol. 16, no. 1, pp. 26-29, 2012.
- [59] Zhe Ding, Xijun Hu, Gao Q. Lu, Po-Lock Yue, and P. F. Greenfield, "Novel Silica Gel Supported TiO<sub>2</sub> Photocatalyst Synthesized by CVD Method". *Langmuir* vol. 16, pp. 6216-6222, 2000.
- [60] Y. Su, S. Chen, X. Quan, H. Zhao, and Y. Zhang, "A silicon-doped TiO<sub>2</sub> nanotube arrays electrode with enhanced photoelectrocatalytic activity". *Applied Surface Science*, vol. 255, no. 5, pp. 2167-2172, 2008.
- [61] Y. Su, J. Wu, X. Quan, and S. Chen, "Electrochemically assisted photocatalytic degradation of phenol using silicon-doped TiO<sub>2</sub> nanofilm electrode". *Desalination*, vol. 252, no. 1-3, pp. 143-148, 2010.
- [62] S. Imamura and H. Tarumoto, "Decomposition of 1,1-dichloroethane on TiO<sub>2</sub>/SiO<sub>2</sub>". *Industrial & Engineering Chemistry Research* vol. 28, pp. 1449-1452, 1989.
- [63] C. B. Khouw, C. B. Dartt, J. A. Labinger, and M. E. Davis, "Studied on the catalytic oxidation of Alkanes and alkenes by titanium silicates". *Journal of Catalysis*, vol. 149, pp. 195-205, 1994.
- [64] S. Yoshida, S. Takenaka, T. Tanaka, H. Hirano, and H. Hayashi, "Highly dispersed titanium oxide on silica: preparation, characterization by XAFS, and photocatalysis". *Surface Science and Catalysis*, vol. 101, pp. 871, 1996.
- [65] C. L. Wong, Y. N. Tan, and A. R. Mohamed, "A review on the formation of titania nanotube photocatalysts by hydrothermal treatment". *Journal of Environmental Management*, vol. 92, no. 7, pp. 1669-80, 2011.
- [66] K. Yang, Y. Dai, and B. Huang, "First-principles calculations for geometrical structures and electronic properties of Si-doped TiO<sub>2</sub>". *Chemical Physics Letters*, vol. 456, no. 1-3, pp. 71-75, 2008.
- [67] W. Shi, Q. Chen, Y. Xu, D. Wu, and C.-f. Huo, "Investigation of the silicon concentration effect on Si-doped anatase TiO<sub>2</sub> by first-principles calculation". *Journal of Solid State Chemistry*, vol. 184, no. 8, pp. 1983-1988, 2011.

- [68] M. N. Asiah, M. H. Mamat, Z. Khusaimi, S. Abdullah, M. Rusop, and A. Qurashi, "Structural and optical properties of hydrothermally synthesized mesoporous Si/TiO<sub>2</sub> nanowire composites". *Microelectronic Engineering*, vol. 136, pp. 31-35, 2015.
- [69] Y. Gao and S. A. Elder, "TEM study of TiO<sub>2</sub> nanocrystals with different particle size and shape". *Materials Letters*, vol. 44, pp. 228–232, 2000.
- [70] X. Dong, J. Tao, Y. Li, and H. Zhu, "Oriented single crystalline TiO<sub>2</sub> nano-pillar arrays directly grown on titanium substrate in tetramethylammonium hydroxide solution". *Applied Surface Science*, vol. 256, no. 8, pp. 2532-2538, 2010.
- [71] S.-B. Choa, J.-S. Noha, M. M. Lenckab, and R. E. Rimanc, "Low temperature hydrothermal synthesis and formation mechanisms of lead titanate (PbTiO<sub>3</sub>) particles using tetramethylammonium hydroxide: thermodynamic modelling and experimental verificatio". *Journal of the European Ceramic Society*, vol. 23, pp. 2323–2335, 2003.
- [72] Z.-h. Liu, K. Ooi, H. Kanoh, W.-p. Tang, and T. Tomida, "Swelling and Delamination Behaviors of Birnessite-Type Manganese Oxide by Intercalation of Tetraalkylammonium Ions". *Langmuir*, vol. 16, pp. 4154-4164, 2000.
- [73] Q. Gao, O. Giraldo, a. W. T., and S. L. Suib, "Preparation of Nanometer-Sized Manganese Oxides by Intercalation of Organic Ammonium Ions in Synthetic Birnessite OL-1Preparation of Nanometer-Sized Manganese Oxides by Intercalation of Organic Ammonium Ions in Synthetic Birnessite OL-1". *Chemical of Materials*, vol., no. 13, pp. 778-786, 2001.
- [74] Z. Tan, K. Sato, and S. Ohara, "Synthesis of layered nanostructured TiO<sub>2</sub> by hydrothermal method". *Advanced Powder Technology*, vol. 26, no. 1, pp. 296-302, 2015.
- [75] T. Kasuga, M. Hiramatsu, A. Hoson, T. Sekino, and K. Niihara, "Formation of Titanium Oxide Nanotube". *Langmuir*, vol. 14, pp. 3160-3163, 1998.
- [76] J. Yang, Z. Jin, X. Wang, W. Li, J. Zhang, S. Zhang, X. Guo, and Z. Zhang, "Study on composition, structure and formation process of nanotube Na<sub>2</sub>Ti<sub>2</sub>O<sub>4</sub>(OH)<sub>2</sub>". *Dalton Transactions*, vol., no. 20, pp. 3898, 2003.
- [77] T. Kasuga, M. Hiramatsu, A. Hoson, T. Sekino, and K. Niihara, "Titania Nanotubes Prepared by Chemical Processing". *Advanced Materials*, vol. 11, no. 15, pp. 1307-1311, 1999.
- [78] C.-C. Tsai, J.-N. Nian, and H. Teng, "Mesoporous nanotube aggregates obtained from hydrothermally treating TiO<sub>2</sub> with NaOH". *Applied Surface Science*, vol. 253, no. 4, pp. 1898-1902, 2006.
- [79] Q. Chen, W. Zhou, G. H. Du, and L.-M. Peng, "Trititanate Nanotubes Made via a Single Alkali Treatment". *Advanced Materials*, vol. 14, no. 17, pp. 1208-1211, 2002.
- [80] G. H. D. Q. Chen, S. Zhang and L.-M. Peng, "The structure of trititanate nanotubes". *Acta Crystallographica Section B Structural Science*, vol. B58, pp. 587-593, 2002.
- [81] Akos Kukovecz, Ma ´ria Hodos, Endre Horva ´th, Gyorgy Radno ´czi, Zolta ´nKo ´nya, and I. Kiricsi, "Oriented Crystal Growth Model Explains the Formation of Titania

- Nanotubes". *The journal of physical chemistry letters B*, vol. 109, pp. 17781-17783, 2005.
- [82] Z. W. Pan, Z. R. Dai, and Z. L. Wang, "Nanobelts of Semiconducting Oxides". *Science*, vol. 291, pp. 1949, 2001.
- [83] Y. W. Micheal H. Huang, Henning Feick, Ngan Tran, Eicke Weber and Peidong Yang, "Catalyst Growth of Zinc Oxide Nanowires by Vapor Transport". *Advanced Materials*, vol. 13, pp. 113, 2001.
- [84] B. D. Yao, Y. F. Chan, and N. Wang, "Formation of ZnO nanostructures by a simple way of thermal evaporation". *Applied Physics Letters*, vol. 81, no. 4, pp. 757, 2002.
- [85] W. I. Park, G. C. Yi, M. Kim, and S. J. P. Cook, "ZnO nanoneedles Grown vertically on Si substrate by non catalytic Vapor phase epitaxy". *Advanced Materials*, vol. 14, pp. 1841, 2002.
- [86] W. I. Park, D. H. Kim, S. W. Jung, and G.-C. Yi, "Metalorganic vapor-phase epitaxial growth of vertically well-aligned ZnO nanorods". *Applied Physics Letters*, vol. 80, no. 22, pp. 4232, 2002.
- [87] Y. Sun, G. M. Fuge, and M. N. R. Ashfold, "Growth of aligned ZnO nanorod arrays by catalyst-free pulsed laser deposition methods". *Chemical Physics Letters*, vol. 396, no. 1-3, pp. 21-26, 2004.
- [88] J. I. Hong, J. Bae, Z. L. Wang, and R. L. Snyder, "Room-temperature, texture-controlled growth of ZnO thin films and their application for growing aligned ZnO nanowire arrays". *Nanotechnology*, vol. 20, no. 8, pp. 085609, 2009.
- [89] D. Lin, W. Pan, and H. Wu, "Morphological Control of Centimeter Long Aluminum-Doped Zinc Oxide Nanofibers Prepared by Electrospinning". *Journal of the American Ceramic Society*, vol. 90, no. 1, pp. 71-76, 2007.
- [90] X. M. Sui, C. L. Shao, and Y. C. Liu, "White-light emission of polyvinyl alcohol/ZnO hybrid nanofibers prepared by electrospinning". *Applied Physics Letters*, vol. 87, no. 11, pp. 113115, 2005.
- [91] S. Xu and Z. L. Wang, "One-Dimensional ZnO Nanostructures: Solution Growth and Functional Properties". *Nano Research*, vol. 4, no. 11, pp. 1013-1098, 2011.
- [92] J. Zhang, L. Sun, C. Liao, and C. Yan, "A simple route towards tubular ZnO". *Chemical Communications*, vol., no. 3, pp. 262-263, 2002.
- [93] C. Wang, B. Mao, E. Wang, Z. Kang, and C. Tian, "Solution synthesis of ZnO nanotubes via a template-free hydrothermal route". *Solid State Communications*, vol. 141, no. 11, pp. 620-623, 2007.
- [94] N. A. Aal, F. Al-Hazmi, A. A. Al-Ghamdi, A. A. Al-Ghamdi, F. El-Tantawy, and F. Yakuphanoglu, "Novel rapid synthesis of zinc oxide nanotubes via hydrothermal technique and antibacterial properties". *Spectrochim Acta A Mol Biomol Spectrosc*, vol. 135, pp. 871-7, 2015.

- [95] Yueping Fang, Xiaogangwen, and S. Yang, "Hydrothermal Synthesis and Optical Properties of ZnO Nanostructured Films Directly Grown from/on Zinc Substrates". *Journal of Sol-Gel Science and Technology*, vol. 36, pp. 227-234, 2005.
- [96] S. Zhu, L. Shan, X. Tian, X. Zheng, D. Sun, X. Liu, L. Wang, and Z. Zhou, "Hydrothermal synthesis of oriented ZnO nanorod–nanosheets hierarchical architecture on zinc foil as flexible photoanodes for dye-sensitized solar cells". *Ceramics International*, vol. 40, no. 8, pp. 11663-11670, 2014.
- [97] X. Wu, H. Bai, C. Li, G. Lu, and G. Shi, "Controlled one-step fabrication of highly oriented ZnO nanoneedle/nanorods arrays at near room temperature". *Chem Commun (Camb)*, vol., no. 15, pp. 1655-7, 2006.
- [98] S. K. Arya, S. Saha, J. E. Ramirez-Vick, V. Gupta, S. Bhansali, and S. P. Singh, "Recent advances in ZnO nanostructures and thin films for biosensor applications: review". *Anal Chim Acta*, vol. 737, pp. 1-21, 2012.
- [99] HaoMing Chen, Chih Kai Chen, Chih-Jung Chen, Liang-Chien Cheng, Pin ChiehWu, Bo Han Cheng, You ZheHo, Ming Lun Tseng, Ying-Ya Hsu, Ting-Shan Chan, Jyh-Fu Lee, Ru-Shi Liu, and D. P. Tsai, "Plasmon Inducing Effects for Enhanced Photoelectrochemical Water Splitting: X-ray Absorption Approach to Electronic Structures". *ACS nano*, vol. 6, pp. 7362-7372, 2012.
- [100] S. K. Das, S. N. Sahoo, S. N. Sarangi, and P. K. Sahoo, "Substrate effect of hydrothermally grown ZnO nanorods and its luminescence properties". *Journal of Experimental Nanoscience*, vol. 8, no. 3, pp. 382-388, 2013.
- [101] X. Wu, G. Lu, C. Li, and G. Shi, "Room-temperature fabrication of highly oriented ZnO nanoneedle arrays by anodization of zinc foil". *Nanotechnology*, vol. 17, no. 19, pp. 4936-4940, 2006.
- [102] B. L. H. C. Zeng, "Room Temperature Solution Synthesis of Monodispersed Single-Crystalline ZnO Nanorods and Derived Hierarchical Nanostructures". *Langmuir*, vol. 20, pp. 4196-4204, 2004.
- [103] X. F. Q. HLCao, Q Gong, W. M. Du, X. D. Ma and Z. K. Zhu, "Shape- and size-controlled synthesis of nanometre ZnO from a simple solution route at room temperature". *Nanotechnology* vol. 17, pp. 3632–3636, 2006.
- [104] Y. W. Heo, V. Varadarajan, M. Kaufman, K. Kim, D. P. Norton, F. Ren, and P. H. Fleming, "Site-specific growth of ZnO nanorods using catalysis-driven molecular-beam epitaxy". *Applied Physics Letters*, vol. 81, no. 16, pp. 3046, 2002.
- [105] W.-T. Chiou, W.-Y. Wu, and J.-M. Ting, "Growth of single crystal ZnO nanowires using sputter deposition". *Diamond and Related Materials*, vol. 12, no. 10-11, pp. 1841-1844, 2003.
- [106] G. X. Congkang Xu, Yingkai Liu, Guanghou Wang, "A simple and novel route for the preparation of ZnO nanorods". *Solid State Communications*, vol. 122, pp. 175-179, 2002.

- [107] H.-I. W. Jih-Jen Wu, Chan-Hao Tseng and Sai-Chang Liu, "Well-Aligned ZnO nanorods via hydrogen treatment of ZnO film". *Advanced Functional materials*, vol. 14, pp. 806, 2004.
- [108] A. D. Soumitra Kar, and Subhadra Chaudhuri, "Simple Solvothermal Route To Synthesize ZnO Nanosheets, Nanonails, and Well-Aligned Nanorod Arrays". *Journal of physical Chemistry B*, vol. 110, pp. 17848-17853, 2006.
- [109] Heqing Yang, Yuzhe Song, Li Li, Junhu Ma, Dichun Chen, Shuling Mai, and H. Zhao, "Large-Scale Growth of Highly Oriented ZnO Nanorod Arrays in the Zn-NH<sub>3</sub> ·H<sub>2</sub>O Hydrothermal System". *Crystal Growth & Design*, vol. 8, pp. 1039-1043, 2008.
- [110] Z. Han, S. Li, J. Li, J. Chu, and Y. Chen, "Facile synthesis of ZnO nanowires on FTO glass for dye-sensitized solar cells". *Journal of Semiconductors*, vol. 34, no. 7, pp. 074002, 2013.
- [111] Q. Hua, W. Ligang, L. Ruijin, and Y. Wenfeng, "Influence of target substrate distance on the properties of transparent conductive Si doped ZnO thin films". *Optik - International Journal for Light and Electron Optics*, vol. 125, no. 15, pp. 3902-3907, 2014.
- [112] S.-H. Lee, W. Kim, and J.-S. Park, "Effects of co-sputtering powers on the properties of silicon-incorporated zinc oxide used as a channel layer of thin film transistors". *Thin Solid Films*, vol. 549, pp. 46-49, 2013.
- [113] H.-C. Wu, Y.-C. Peng, and T.-P. Shen, "Electronic and Optical Properties of Substitutional and Interstitial Si-Doped ZnO". *Materials*, vol. 5, no. 12, pp. 2088-2100, 2012.
- [114] C. Y. C. B.H. Chua, L.C. Leub, D. Nortonb , J. Leea, T. Lelea, P. Jianga, Y. Tsenga, S. J. Peartonb, A. Guptec, B. Keselowskyd, and F. Rena, "Hydrothermally Grown ZnO Nanorods as Cell Adhesion Control Coating for Implant Devices". *ECS Transactions*, vol. 19, no. 3, pp. 147-157, 2009.
- [115] M. Ranjbar, M. A. Taher, and A. Sam, "Facile Single-Step Synthesis of SiO<sub>2</sub>-Coated ZnO Nanorod as Hydrophobic Layer by Hydrothermal Method". *Journal of Cluster Science*, vol. 27, no. 1, pp. 105-114, 2015.
- [116] G. G. Bessegato, T. T. Guaraldo, and M. V. B. Zanoni, "Enhancement of Photoelectrocatalysis Efficiency by Using Nanostructured Electrodes". 2014.
- [117] H. Zhang, G. Chen, and D. W. Bahnemann, "Photoelectrocatalytic materials for environmental applications". *Journal of Materials Chemistry*, vol. 19, no. 29, pp. 5089, 2009.
- [118] I. Paramasivam, H. Jha, N. Liu, and P. Schmuki, "A review of photocatalysis using self-organized TiO<sub>2</sub> nanotubes and other ordered oxide nanostructures". *Small*, vol. 8, no. 20, pp. 3073-103, 2012.
- [119] M. Mahanti and D. Basak, "Enhanced ultraviolet photoresponse in Au/ZnO nanorods". *Chemical Physics Letters*, vol. 612, pp. 101-105, 2014.

- [120] K. Lance Kelly, Eduardo Coronado, Lin Lin Zhao, and G. C. Schatz, "The Optical Properties of Metal Nanoparticles: The Influence of Size, Shape, and Dielectric Environment". *J. Phys. Chem. B*, vol. 107, pp. 668-677, 2003.
- [121] M. Grätzel, "Photoelectrochemical cells". *NATURE*, vol. 414, pp. 338, 2001.
- [122] P. Wang, D. Wu, Y. Ao, C. Wang, and J. Hou, "ZnO nanorod arrays co-loaded with Au nanoparticles and reduced graphene oxide: Synthesis, characterization and photocatalytic application". *Colloids and Surfaces A: Physicochemical and Engineering Aspects*, vol. 492, pp. 71-78, 2016.
- [123] Z. Liu, W. Hou, P. Pavaskar, M. Aykol, and S. B. Cronin, "Plasmon resonant enhancement of photocatalytic water splitting under visible illumination". *Nano Lett*, vol. 11, no. 3, pp. 1111-6, 2011.
- [124] D. D. Evanoff, Jr. and G. Chumanov, "Synthesis and optical properties of silver nanoparticles and arrays". *Chemphyschem*, vol. 6, no. 7, pp. 1221-31, 2005.
- [125] T. H. T. Vu, H. T. Au, L. T. Tran, T. M. T. Nguyen, T. T. T. Tran, M. T. Pham, M. H. Do, and D. L. Nguyen, "Synthesis of titanium dioxide nanotubes via one-step dynamic hydrothermal process". *Journal of Materials Science*, vol. 49, no. 16, pp. 5617-5625, 2014.
- [126] T. S. Natarajan, H. C. Bajaj, and R. J. Tayade, "Preferential adsorption behavior of methylene blue dye onto surface hydroxyl group enriched TiO<sub>2</sub> nanotube and its photocatalytic regeneration". *Journal of Colloid and Interface Science*, vol. 433, pp. 104-14, 2014.
- [127] L. B. Fen, T. K. Han, N. M. Nee, B. C. Ang, and M. R. Johan, "Physico-chemical properties of titania nanotubes synthesized via hydrothermal and annealing treatment". *Applied Surface Science*, vol. 258, no. 1, pp. 431-435, 2011.
- [128] S. Dai, Y. Wu, T. Sakai, Z. Du, H. Sakai, and M. Abe, "Preparation of Highly Crystalline TiO<sub>2</sub> Nanostructures by Acid-assisted Hydrothermal Treatment of Hexagonal-structured Nanocrystalline Titania/Cetyltrimethylammonium Bromide Nanoskeleton". *Nanoscale Research Letters*, vol. 5, pp. 1829-1835, 2010.
- [129] T.-V. Nguyen and O. B. Yang, "Photoresponse and AC impedance characterization of TiO<sub>2</sub>-SiO<sub>2</sub> mixed oxide for photocatalytic water decomposition". *Catalysis Today*, vol. 87, no. 1-4, pp. 69-75, 2003.
- [130] X. Quan, S. Yang, X. Ruan, and H. Zhao, "Preparation of Titania Nanotubes and Their Environmental Applications as Electrode". *Environment Science Technology*, vol. 39, pp. 3770-3775, 2005.
- [131] Y. Wang and N. Herron, "Nanometer-Sized Semiconductor Clusters: Materials Synthesis, Quantum Size Effects, and Photophysical Properties". *Journal of Physical Chemistry*, vol. 95, pp. 525-532, 1991.
- [132] A. Zaleska, "Doped-TiO<sub>2</sub>: A Review". *Recent Patents on Engineering*, vol. 2, pp. 157-164, 2008.

- [133] K. Kočí, L. Obalová, L. Matějová, D. Plachá, Z. Lacný, J. Jirkovský, and O. Šolcová, "Effect of TiO<sub>2</sub> particle size on the photocatalytic reduction of CO<sub>2</sub>". *Applied Catalysis B: Environmental*, vol. 89, no. 3-4, pp. 494-502, 2009.
- [134] K. Lance Kelly, Eduardo Coronado, Lin Lin Zhao, and G. C. Schatz, "The Optical Properties of Metal Nanoparticles: The Influence of Size, Shape, and Dielectric Environment". *Journal of Physical Chemistry B*, vol. 107, pp. 668-677, 2003.
- [135] S. Dhara and P. K. Giri, "Improved fast photoresponse from Al doped ZnO nanowires network decorated with Au nanoparticles". *Chemical Physics Letters*, vol. 541, pp. 39-43, 2012.
- [136] T. E. Murphy, K. Moazzami, and J. D. Phillips, "Trap-Related Photoconductivity in ZnO Epilayers". *Journal Of Electronic Materials*, vol. 35, no. 4, pp. 543, 2006.

## Appendix

### International journal papers

1. **Phuong Dao**, Kang Du, Guohua Liu, Gang Li, Muhammad Tayyib and Kaiying Wang, “Synthesis and photocatalytic properties of silicon doped TiO<sub>2</sub> nanotubes”, preparing for **Advances in Materials Science and Engineering**.
2. **Phuong Dao**, Guohua Liu, Kang Du, Vy Nguyen, and Kaiying Wang,” Modulation of surface plasmon in gold decorated ZnO nanorods by dielectric silicon oxide”, preparing to submit **Electrochimica Acta**.

## PAPER 1

### Synthesis and photocatalytic properties of silicon doped TiO<sub>2</sub> nanotubes

Phuong Dao<sup>1</sup>, Kang Du<sup>1</sup>, Guohua Liu<sup>1</sup>, Gang Li<sup>2</sup>, Muhammad Tayyib<sup>1</sup> and Kaiying Wang<sup>1</sup>

<sup>1</sup> Department of Micro and Nano Systems Technology, University College of Southeast Norway, Horten, 3184, Norway.

<sup>2</sup> MicroNano System Research Center, College of Information Engineering, Taiyuan University of Technology, Taiyuan 030024, China

\*Corresponding Author: E-mail: Kaiying.Wang@hbv.no, Tel: + 47 3100 9317

**Abstract:** In this paper, we report the synthesis and photocatalytic properties of silicon doped TiO<sub>2</sub> nanotubes (TNTs) through hydrothermal method, which the starting materials are crystal silicon and TiO<sub>2</sub> powders. The diameter of the TiO<sub>2</sub> nanotubes is about 20 nm with several micrometers in length and dopant (Si/(Si+Ti)) molar ratio in range of 1~30%. X-ray diffraction analysis verifies formation of nanocrystalline anatase phase for both pristine and Si-doped TNTs. The light absorption spectra of doped TNTs exhibit red shift from 375 nm to 410 nm as compared with that of the un-doped TNTs. Photodegradation experiment shows that this red-shift of spectra absorption is desirable for the redox reaction under relatively long wavelength light illumination.

**Key words:** TiO<sub>2</sub> nanotubes, Silicon dope TNTs, photoresponsivity.

#### 1. Introduction

Titanium dioxide (TiO<sub>2</sub>) are attractive materials due to their commercial availability, suitable optical/electronic qualities and chemical stability [1]. Compared to other forms of titanium dioxide nanomaterials, titania nanotubes exhibit better physical and chemical properties in photocatalysis [2]. However, because of large energy band gap ~3.87 eV for

anatase titanate nanotubes, 3.2 eV for nanoparticles, considerable attempts have been paid to narrow the band gap of TiO<sub>2</sub> by doping [3].

Silicon modified TiO<sub>2</sub> have been made in past few years. Introducing element Si into TiO<sub>2</sub> matrix enables higher photoactivity, quantum sized crystalline and good surface wettability [4-7]. Kyeong et al. reported that addition of silica suppresses the phase transformation from anatase to rutile, resulting in high thermal stability [8]. Chao et.al indicated that there is a strong interaction among the Ti-O-Si linkages according to FT-IR spectra (948 cm<sup>-1</sup> from) [9]. This interaction between titania and silica boosts up the surface properties and photocatalytic activity. An appropriate amount of the doped silica can generate positive influences [4] while the exceed amount of Si-dopant (>2%) reduces Ti atoms of the surface of catalyst [10]. Chao et al. synthesized higher thermal stability, lower bulk defects, optimal Bronsted acidity and highest photoactivity at TiO<sub>2</sub>-9.1% mol SiO<sub>2</sub> [9]. Jin et al. proved that the highest efficiency of photo-degradation of gas NO was obtained by using 0.03 Si doped TiO<sub>2</sub> [11]. There are also studies about doping silicon on nanotubes by depositing silicon onto self-ordered TiO<sub>2</sub> nanotube arrays using chemical vapor deposition and anodization method respectively [6, 12]. However, these studies focus on the photocatlytic performance of silicon doped-TNTs, lacking of discussion on band gap modification when introducing silicon.

Calleja et al. found that the introducing silicon to TiO<sub>2</sub> structure leads to increase of the band gap (E<sub>G</sub>) [13]. Bao et al. observed the blue shift in UV-spectra due to the quantum size and the interface interactions [4]. The increment in band gap energy results in lowering the energy of valance band and increasing in the conduction band edge [14]. However, first principles calculations points out that incorporation of Si element into the crystal structure of TiO<sub>2</sub>, especially TNTs would narrow down the band gap of TiO<sub>2</sub> [15, 16]. Thus, the red shifts in UV absorption spectrum are assumed for introducing silicon into TiO<sub>2</sub> crystal.

In this paper, silicon is introduced directly on TiO<sub>2</sub> nanotubes by using hydrothermal method from TiO<sub>2</sub> powder and Silicon powder. Different amounts of silicon are investigated and compared to the un-doped sample. Nanotubes morphology is characterized by SEM and TEM. It was found that Si doping would not affect the structure of TiO<sub>2</sub> nanotubes. UV-vis spectra indicates the red shift that effectively extends its optical absorption edges. This red shift is beneficial for photodegradation of methylene blue in long wavelength light illumination

## **2. Experimental details**

TNTs was prepared by using hydrothermal condition proposed by Kasuga et.al [17]. Typically, 1.6 g TiO<sub>2</sub> (anatase, 99.7 %, Sigma-Aldrich) were mixed with different amounts of

Si powder and 75 ml of NaOH 10 M in a 100 ml Teflon tube which was then heated at 150°C in 24h under stirring condition on a heater. The Si/(Si+Ti) mole ratios were varied from 0.01 to 0.3. After reaction, the white precipitates were filtered and washed several time with water and HCl 0.1 M until pH of washing solution approached 7.0. Finally, the sediment was dried at 80°C overnight and calcined at 450°C for 1h. The as synthesis samples were labelled as X-TNTs (X equals to the Si/(Si+Ti) mole ratio).

The morphology and composition of catalyst were characterized by using scanning electron microscopy (SEM, Hitachi 1081) with accelerating voltage at 30 kV and TEM (TEM LIBRA 120) operating at 120 kV. An Energy-dispersive X-ray spectroscopy (EDX) is integrated in the SEM machine to determine the composition of the catalyst. The crystallinity of TNTs was recorded by X-ray diffraction (XRD) using a diffractometer with Cu K $\alpha$  radiation = 0.154 nm (Bruker AXS D8 Discover). The absorption spectra was recorded on a spectrophotometer (SHIMADZU, UV-2600 with ISR-2600 integrating Sphere Attachment) in range of 220-830 nm with fine BaSO<sub>4</sub> powder as reference.

To evaluate the photocatalytic performance of TNTs and modified TNTs, the degradation of aqueous solution of methylene blue was carried out. 20 mg of catalyst powder were placed into 50 ml of 25 ppm methylene blue solution under stirring condition in dark for 30 min. After that, the photocatalytic reaction was taken place under ultraviolet ray with wavelength 365 nm. The durations of irradiation were 10, 15, 30, 45 and 60 min following by recording the adsorption spectra of each sample using a UV-vis spectrophotometer.

### 3. Results and Discussion

Titania nanotubes were hydrothermally synthesized at 150°C in 24 h using TiO<sub>2</sub> nanopowders (TNPs) as precursor with an average diameter of 25 nm. Fig. 1 illustrates the electron microscopy images, transmission electron microscopy and energy dispersive spectroscopy of the pure TNTs and doped TNTs. The as-prepared TNTs before calcining in Fig. 1(a) appears in shape of nanowires clusters at low magnification. Higher magnification clarifies the shape of individual wire with the diameter of 10 to 20 nm. The length of each nanotube is varied from hundred nanometers to several micrometers. Besides, only a certain small amount of silicon remained in 0.1-TNTs sample according to EDX result shown in Fig. 1(b). The amount of doped silicon did not change much despite the increase of initial doped amount. Fig. 1(c) shows the TEM images which confirm the hollow structure of TNTs. A single tube with diameter of 7 nm with lattice fringes, which represents for crystal structure of TNTs after heat treatment, is revealed in Fig. 1(d). It has clearly been seen that the morphology of TNTs was

not deformed after heat treatment at 450°C. Furthermore, there is no significant difference in the physical appearance of TNTs before and after doping. This observation is in good agreement with Kasuga et al. result [17] that SiO<sub>2</sub> does not interfere the formation of TiO<sub>2</sub> nanotubes by chemical treatment method.

The phase compositions of doped and non-doped samples were analyzed by XRD techniques, as shown in Fig. 2. The significant peaks at  $2\theta$  values 25.3, 37.8, 48, 53.9, 55.17 correspond to plane (101), (004), (200), (105), (211) respectively corresponding to JCPDS-21-1272 standard. No trace of peak proves the existence of rutile or any titanate phases which means that there is no phase transformation and titanate has been decomposed into pure anatase phase at 450°C. The similar results were reported by Natarajan et al. [18]. The distinct point between doped and undoped sample is the crystallinity. The pure TNTs sample performs poor crystallization while introducing silicon supports the growth of anatase crystal which is chemically and optically active and widely used as catalysts and supports [19]. The crystal characteristics and the calculated crystal size based on the Scherrer's equation are illustrated in the table 1. The lattice spacing of plane (101) is quite close to that of anatase crystal [20]. Comparing to the crystal size of precursor 25 nm, TNTs have smaller average size since doping with silicon could associate with a small substitution of Si into TiO<sub>2</sub> lattice which leads to an increase of the crystal size. The same crystal size of 0.1-TNTs and 0.3 TNTs is due to the requirement of large formation energy [16]. Thus, no matter how much Si presents, only small amount of it is able to be doped into the TiO<sub>2</sub> lattice. This is however consistent with EDS results.

Fig. 3 performs the UV-vis diffuse reflectance spectroscopy of undoped TiO<sub>2</sub> nanotubes and Si-doped TiO<sub>2</sub> nanotubes. It can be seen that there are two main groups with the band gap absorption edges at around 375 and 410 nm. The calculated band gap energies using the equation,  $E(\text{eV}) = 1239.95/\lambda$  (nm) [21] are listed in table 2 and plotted in Fig. 4. According to calculation, the band gap of TNPs is 3.22 eV which are typical for anatase TiO<sub>2</sub> photocatalytic band gap energy 3.2 eV [22]. After transformation into titania nanotubes, the band gap energy increases to the value of 3.26 eV. This blue shift could be attributed to quantum size effect of TiO<sub>2</sub> semiconductor in TNTs [23] due to very thin nanotube wall thickness. In the Si-doped range of 0 to 0.1, the band gap energy of the TNTs decreases compared to TNPs and 0-TNTs. As reported by Yang et al., the substitutional Si to Ti-doped anatase results in the band gap narrowing about 0.25 eV [15] and this band gap reduction proves the interruption of Si to TNTs lattice. The red shift which is beneficial for visible light absorption [24] could be achieved at

the doped silicon amount lower than 0.1. Nevertheless, with large amount of Si in precursor, the band gap of photon excitation has no further narrowing but increasing which is in good agreement with the simulation results of Shi et al [16]. Introducing more Si into hydrothermal reactor would be a disadvantage because of the released hydrogen from the reaction between Si powder and NaOH causing high pressure. Too high pressure will suppress the dilution of Si. Hence, fewer amount of Si is successfully doped. Even if more silicon could be doped into titania, the band gap still increases corresponding to the simulation results of Shi et al [16].

For photocatalytic performance, undoped TNTs and doped TNTs were utilized to study the degradation of methylene blue (MB) absorption spectra. Base on the UV-vis absorption spectrum, the wavelength of the light source was chosen at 365 nm to determine the distinctions between samples. Fig. 5 shows the variation of the MB concentration over the time under dark and UV illumination condition. The blank curve proves that without catalysts, methylene blue is barely degraded under UV-light. Dark absorption region is where the catalyst performs the ability to capture methylene blue without the energy from the light. Both photocatalytic activity and absorption ability depend on the particle size or surface area. Small particle size or high surface area would be beneficial for photodegradation of MB [25]. This is in good agreement with the XRD result that TNPs size is larger than 0.1, 0.3-TNTs and larger than 0-TNTs. The degradation ability also follows this order respectively. However, only a suitable low amount doped Si could increase the photoactivity [4, 10]. Moreover, according to XRD result and UV-vis spectrum, introducing Si enhances the crystallinity of anatase phase and the ability to absorb longer wavelength light which generates more electron and hole pairs for the oxidation of MB. It also increases the hydroxyl group amount supporting the dispersion of TiO<sub>2</sub> into water. As a result, doping with appropriate low amount of Si results in the highest photodegradation rate.

#### **4. Conclusion**

In this study, silicon was in-situ doped on TiO<sub>2</sub> nanotubes by a simple hydrothermal method. The morphology of TNTs was successfully revealed by TEM and SEM. The hollow structure of TNTs remains unchanged after modifying with silicon. XRD results indicate that the size between undoped and doped sample varies from 11.08 nm to 24.02 nm. Higher crystallinity of anatase TiO<sub>2</sub> is observed after introducing Si. Especially, red shift in UV-absorption spectrum clarified the interruption of Si into TiO<sub>2</sub> lattice. The band gap energy decreases significantly from 3.26 eV (undoped) to 3.04 eV (doped). The photodegradation result is consistent with XRD and UV-vis absorption test that low amount of doped Si (<5%) is beneficial for photocatalytic activity.

## Conflict of Interests

The authors declare that there is no conflict of interests regarding the publication of this paper.

## Acknowledgements

The authors are grateful to Zekija Ramic and Ragnar D. Johansen for helping experimental preparation, Joachim Seland Graff and Annett Thøgersen for help with SEM at SINTEF, Klaus Magnus Haland Johansen and Heine Nygard Riise for help with XRD at University of Oslo. The Norwegian Research Council-FRINATEK programme (231416/F20), EEA-Poland (237761) and partial funding for this work was obtained from the Norwegian PhD Network on Nanotechnology for Microsystems, which is sponsored by the Research Council of Norway, Division for Science, under contract no. 221860/F40.

## References

- [1] G. Liu, N. Hoivik, K. Wang, and H. Jakobsen, "Engineering TiO<sub>2</sub> nanomaterials for CO<sub>2</sub> conversion/solar fuels". *Solar Energy Materials and Solar Cells*, vol. 105, pp. 53-68, 2012.
- [2] C. L. Wong, Y. N. Tan, and A. R. Mohamed, "A review on the formation of titania nanotube photocatalysts by hydrothermal treatment". *Journal of Environmental Management*, vol. 92, no. 7, pp. 1669-80, 2011.
- [3] N. Liu, X. Chen, J. Zhang, and J. W. Schwank, "A review on TiO<sub>2</sub>-based nanotubes synthesized via hydrothermal method: Formation mechanism, structure modification, and photocatalytic applications". *Catalysis Today*, vol. 225, pp. 34-51, 2014.
- [4] N. W. Bao, Z. Ma, Z. Liu, F. Yin, G., "Si-doped mesoporous TiO<sub>2</sub> continuous fibers: preparation by centrifugal spinning and photocatalytic properties". *Journal of Hazardous Materials* vol. 174, no. 1-3, pp. 129-36, 2010.
- [5] X. Yan, J. He, D. G. Evans, X. Duan, and Y. Zhu, "Preparation, characterization and photocatalytic activity of Si-doped and rare earth-doped TiO<sub>2</sub> from mesoporous precursors". *Applied Catalysis B: Environmental*, vol. 55, no. 4, pp. 243-252, 2005.
- [6] Y. Su, S. Chen, X. Quan, H. Zhao, and Y. Zhang, "A silicon-doped TiO<sub>2</sub> nanotube arrays electrode with enhanced photoelectrocatalytic activity". *Applied Surface Science*, vol. 255, no. 5, pp. 2167-2172, 2008.
- [7] R. Klaysri, S. Wichaidit, T. Tubchareon, S. Nokjan, S. Piticharoenphun, O. Mekasuwandumrong, and P. Prasertdam, "Impact of calcination atmospheres on the physiochemical and photocatalytic properties of nanocrystalline TiO<sub>2</sub> and Si-doped TiO<sub>2</sub>". *Ceramics International*, vol. 41, no. 9, pp. 11409-11417, 2015.
- [8] K. Y. Jung and S. B. Park., "Enhanced photoactivity of silica-embedded titania particles prepared by sol-gel process for the decomposition of trichloroethylene". *Applied Catalysis B: Environmental*, vol. 25, pp. 249-256, 2000.
- [9] C. Xie, Z. Xu, Q. Yang, B. Xue, Y. Du, and J. Zhang, "Enhanced photocatalytic activity of titania-silica mixed oxide prepared via basic hydrolyzation". *Materials Science and Engineering: B*, vol. 112, no. 1, pp. 34-41, 2004.

- [10] S. M. Oh, S. S. Kim, J. E. Lee, T. Ishigaki, and D. W. Park, "Effect of additives on photocatalytic activity of titanium dioxide powders synthesized by thermal plasma". *Thin Solid Films*, vol. 435, pp. 252–258, 2003.
- [11] R. Jin, Z. Wu, Y. Liu, B. Jiang, and H. Wang, "Photocatalytic reduction of NO with NH<sub>3</sub> using Si-doped TiO<sub>2</sub> prepared by hydrothermal method". *Journal of Hazardous Materials*, vol. 161, no. 1, pp. 42-8, 2009.
- [12] Y. Zhang, X. Li, D. Chen, N. Ma, X. Hua, and H. Wang, "Si doping effects on the photocatalytic activity of TiO<sub>2</sub> nanotubes film prepared by an anodization process". *Scripta Materialia*, vol. 60, no. 7, pp. 543-546, 2009.
- [13] G. Calleja, D. P. Serrano, R. Sanz, and P. Pizarro, "Mesostructured SiO<sub>2</sub>-doped TiO<sub>2</sub> with enhanced thermal stability prepared by a soft-templating sol-gel route". *Microporous and Mesoporous Materials*, vol. 111, no. 1-3, pp. 429-440, 2008.
- [14] P. Periyat, K. V. Baiju, P. Mukundan, P. K. Pillai, and K. G. K. Warriar, "High temperature stable mesoporous anatase TiO<sub>2</sub> photocatalyst achieved by silica addition". *Applied Catalysis A: General*, vol. 349, no. 1-2, pp. 13-19, 2008.
- [15] K. Yang, Y. Dai, and B. Huang, "First-principles calculations for geometrical structures and electronic properties of Si-doped TiO<sub>2</sub>". *Chemical Physics Letters*, vol. 456, no. 1-3, pp. 71-75, 2008.
- [16] W. Shi, Q. Chen, Y. Xu, D. Wu, and C.-f. Huo, "Investigation of the silicon concentration effect on Si-doped anatase TiO<sub>2</sub> by first-principles calculation". *Journal of Solid State Chemistry*, vol. 184, no. 8, pp. 1983-1988, 2011.
- [17] T. Kasuga, M. Hiramatsu, A. Hoson, T. Sekino, and K. Niihara, "Formation of Titanium Oxide Nanotube". *Langmuir*, vol. 14, pp. 3160-3163, 1998.
- [18] T. S. Natarajan, H. C. Bajaj, and R. J. Tayade, "Preferential adsorption behavior of methylene blue dye onto surface hydroxyl group enriched TiO<sub>2</sub> nanotube and its photocatalytic regeneration". *Journal of Colloid and Interface Science*, vol. 433, pp. 104-14, 2014.
- [19] L. B. Fen, T. K. Han, N. M. Nee, B. C. Ang, and M. R. Johan, "Physico-chemical properties of titania nanotubes synthesized via hydrothermal and annealing treatment". *Applied Surface Science*, vol. 258, no. 1, pp. 431-435, 2011.
- [20] S. Dai, Y. Wu, T. Sakai, Z. Du, H. Sakai, and M. Abe, "Preparation of Highly Crystalline TiO<sub>2</sub> Nanostructures by Acid-assisted Hydrothermal Treatment of Hexagonal-structured Nanocrystalline Titania/Cetyltrimethylammonium Bromide Nanoskeleton". *Nanoscale Research Letters*, vol. 5, pp. 1829-1835, 2010.
- [21] T.-V. Nguyen and O. B. Yang, "Photoresponse and AC impedance characterization of TiO<sub>2</sub>-SiO<sub>2</sub> mixed oxide for photocatalytic water decomposition". *Catalysis Today*, vol. 87, no. 1-4, pp. 69-75, 2003.
- [22] X. Quan, S. Yang, X. Ruan, and H. Zhao, "Preparation of Titania Nanotubes and Their Environmental Applications as Electrode". *Environment Science Technology*, vol. 39, pp. 3770-3775, 2005.
- [23] Y. Wang and N. Herron, "Nanometer-Sized Semiconductor Clusters: Materials Synthesis, Quantum Size Effects, and Photophysical Properties". *Journal of Physical Chemistry*, vol. 95, pp. 525-532, 1991.
- [24] A. Zaleska, "Doped-TiO<sub>2</sub>: A Review". *Recent Patents on Engineering*, vol. 2, pp. 157-164, 2008.

[25] K. Kočí, L. Obalová, L. Matějová, D. Plachá, Z. Lacný, J. Jirkovský, and O. Šolcová, "Effect of TiO<sub>2</sub> particle size on the photocatalytic reduction of CO<sub>2</sub>". *Applied Catalysis B: Environmental*, vol. 89, no. 3-4, pp. 494-502, 2009.

## Figure

**Figure 1.** (a) SEM images of hydrothermal product of pure TNTs after calcining (b) EDX spectrum of TNTs after introducing Silicon. (c) TEM image of pure TNTs after calcining (d) TEM image of individual tube.

**Figure 2.** XRD pattern of calcined (a) 0.3 mol ratio silicon doped TiO<sub>2</sub> nanotubes (or nanowire), (b) 0.1 mol ratio of silicon doped TiO<sub>2</sub> nanotubes (or nanowires), (c) Pure TiO<sub>2</sub> nanotubes (or nanowires), (d) Anatase-JCPDS-21-1272 standard.

**Figure 3.** UV-vis absorption spectra of (a) 0-TNTs (b) 0.1-TNTs (c) 0.3-TNTs

**Figure 4.** Band gap energy of different doped silicon amount

**Figure 5.** Photodegradation of MB using undoped TNTs and doped TNTs.

## Table

**Table 1:** XRD results of doped and undoped sample.

**Table 2:** Band gap of the sample calcined at 450°C

Figure 1.

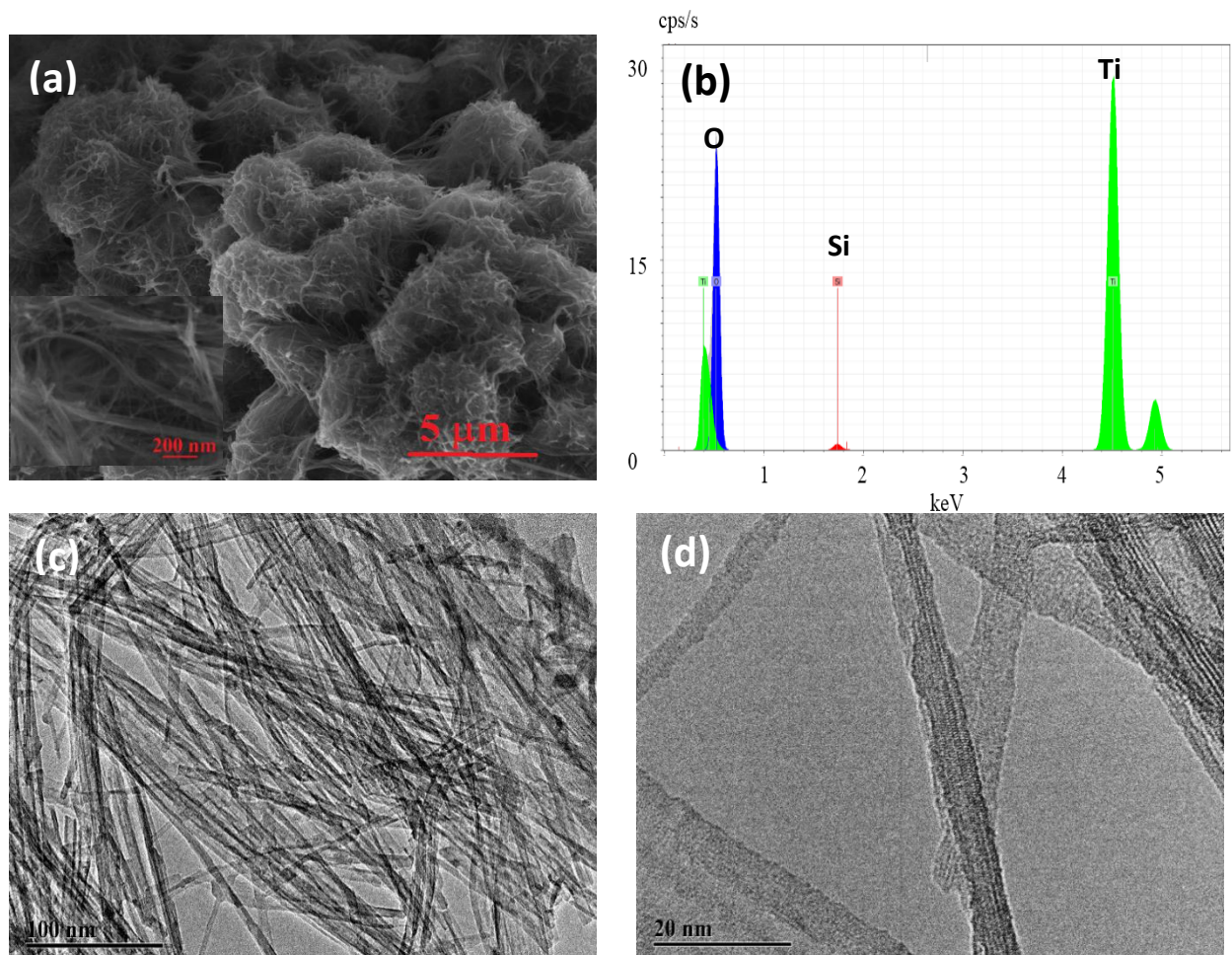


Figure 2.

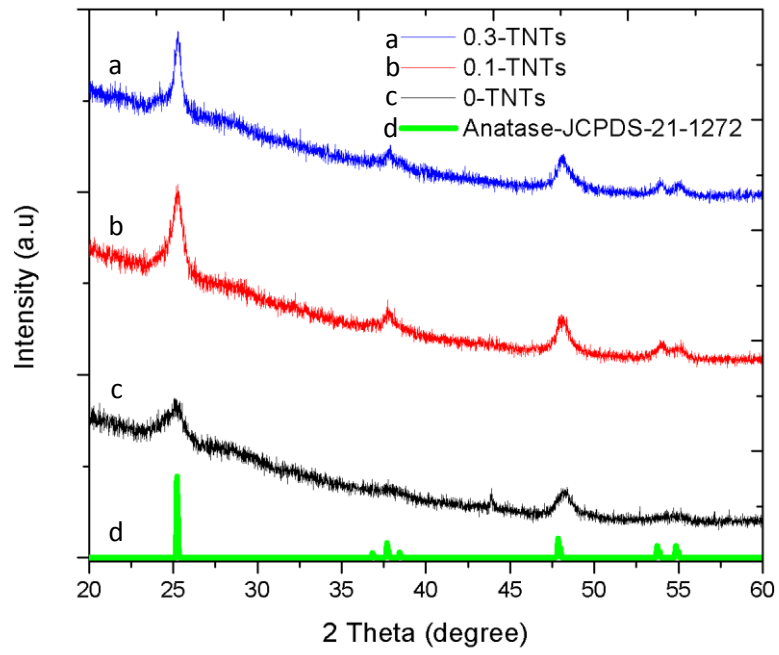


Figure 3.

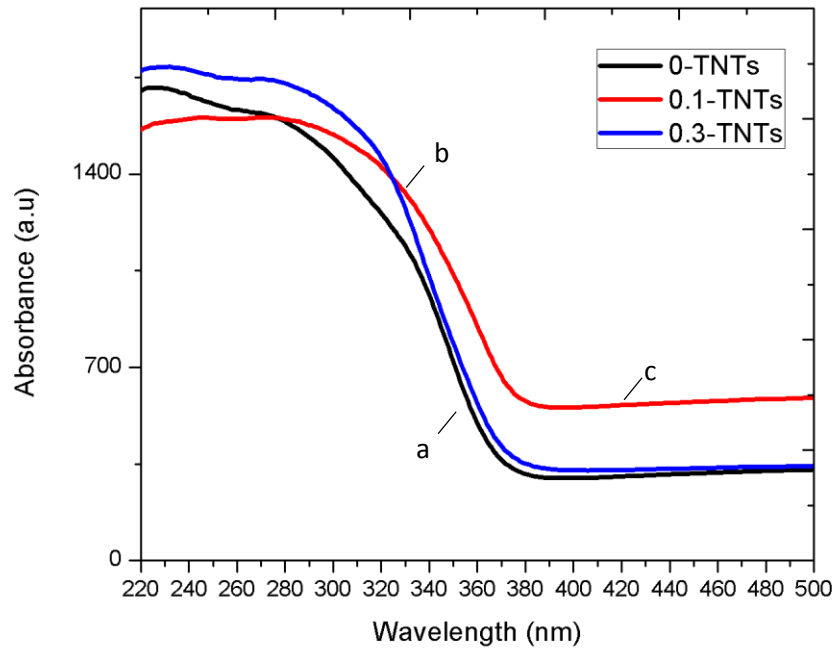


Figure 4.

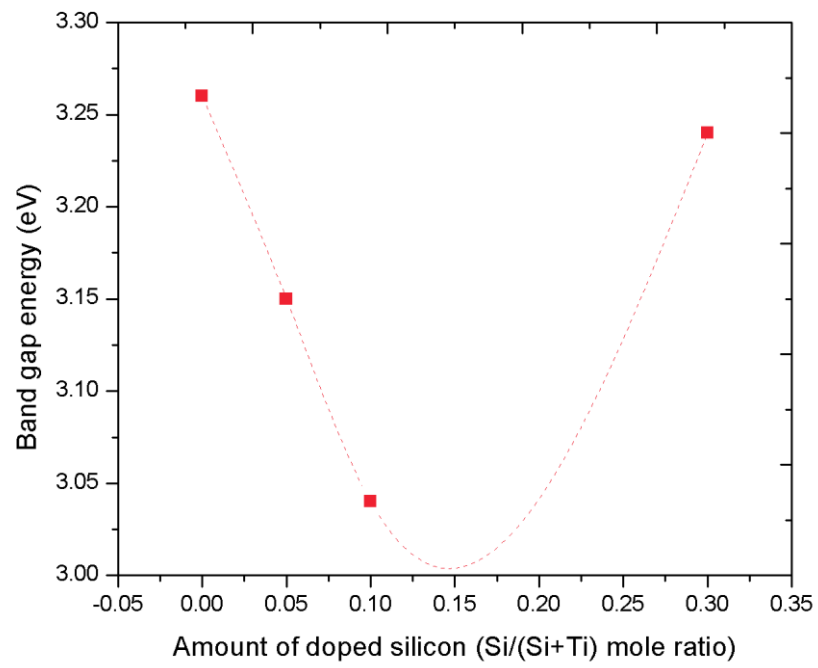
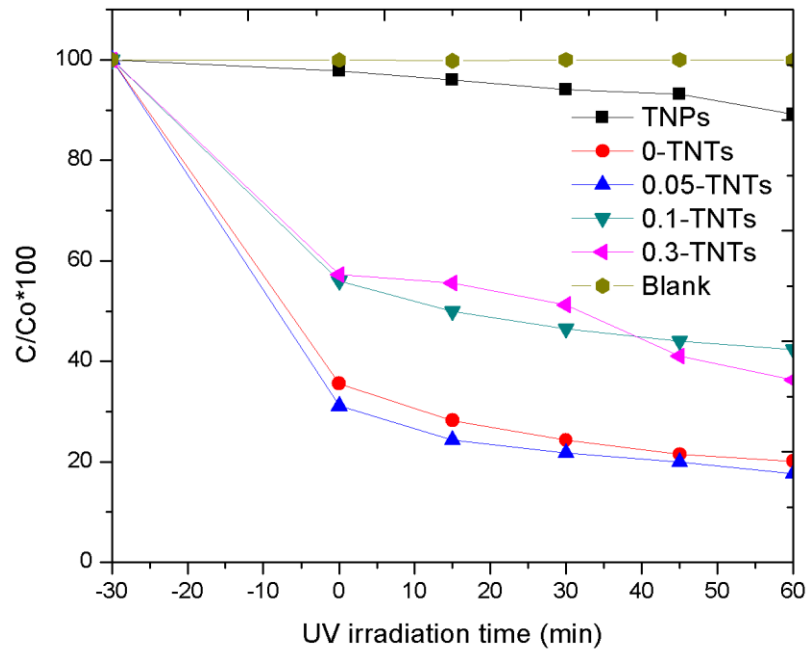


Figure 5.



**Table 1**

Sample	Crystalsize (nm)	Lattice spacing, a, for (101) plane	Interplanar spacing
TNTs	11.08	3.53	2.496
TNTs-0.1	24.02	3.52	2.489
TNTs-0.3	24.02	3.52	2.491

**Table 2**

Sample	Band gap energy (eV)
TNPs	3.22
0-TNTs	3.26
0.05-TNTs	3.15
0.1-TNTs	3.04
0.3-TNTs	3.24

## PAPER 2

# Modulation of surface plasmon in gold decorated ZnO nanorods by dielectric silicon oxide

Phuong Dao<sup>1</sup>, Guohua Liu<sup>1</sup>, Kang Du<sup>1</sup>, Vy Nguyen<sup>1</sup>, and Kaiying Wang<sup>1\*</sup>

<sup>1</sup>Department of Micro and Nanosystems Technology, University College of Southeast Norway, Horten 3184, Norway

\*Corresponding Author: E-mail: Kaiying.Wang@hbv.no, Tel: + 47 3100 9317

**Abstract:** The noble metal nanoparticles show active absorption in visible region due to the existence of the unique feature known as surface plasmon resonance (SPR). On a fundamental aspect, it will be interest to explore how to modulate of surface plasmons by capitalizing on the advances in metamaterial science and nanosynthesis. In this paper, we combine self-assembling hydrothermal synthesis and magnetron sputtering deposition to tune the effective optical properties of a plasmonic array at atomic scale. Particularly, a series of composite photoelectrode based ZnO nanorods backbone coated by SiO<sub>2</sub> and Au with different orders are well prepared and characterized. The photoelectrical behavior of SPR effect in gold decorated ZnO nanorods are tested after tailoring the dielectric of surrounding environment. Among those, the sample ZnO-SiO<sub>2</sub>-Au with spacer in middle inhibits the SPR effect, while the ZnO-Au-SiO<sub>2</sub> configuration produces an outstanding photocurrent enhancement. Moreover, compared to gold decorated ZnO nanorods, the coating of SiO<sub>2</sub> dielectric layer onto the plasmonic ZnO-Au structure results in fast photoresponse in both rising and decaying time. These findings provide a unique mechanism for controlling the plasmonic properties of small metal nanoparticles.

**Keywords:** ZnO nanotubes, surface plasmon resonant, dielectric layer, photoresponse.

**Highlights:**

- (1) Sputtering an Au-nanoparticle array on the surface of semiconductor ZnO nanorods induces strong surface plasmon resonant.
- (2) The SiO<sub>2</sub> dielectric layer enhances light absorption by light trapping structure.
- (3) The SPR effect can be modulation through rational design of the plasmonic configurations.
- (4) The ZnO NRs-Au-SiO<sub>2</sub> and ZnO NRs-SiO<sub>2</sub>-Au configuration result in fast and strong photoresponse.

## 1. Introduction

One dimensional nanostructure (1D) ZnO have been attracting considerable attention owing to the high ratio length to width, larger specific surface area, higher light photons capture efficiency as well as higher photo induced charges generation and transfer rate than ZnO nanoparticles [2]. Because of its wide band gap (3.37 eV), a great of endeavors have been conducted by coupling semiconductor photocatalysts, semiconductor quantum dot, metal nanostructure, band gap narrowing and defect creation [4] to improve the visible light absorption ability and prominent charge recombination [5].

Surface plasmon resonant (SPR) effect has been widely investigated because of the drastic enhancement of photocurrent generation under visible light illumination. Among them, nanostructures of noble metals are rising a considerable concern due to its strong interaction with incoming photon through excitation of localized surface plasmon resonance (LSPR) [6, 7]. SPR can be defined as the resonant photo-induced collective oscillation of valence electrons when there is a match between photon frequency and the natural frequency of surface electron of the noble metal, typically gold [8]. Under visible light illumination, the continuously injected hot electrons from gold nanostructure into conduction band of semiconductor and the formation of Schottky barrier facilitates electron-hole separation thus promoting the photoelectrical performance [9, 10]. Although, tuning SPR by size, shape and distribution of noble metal has been widely studied, the dependence of SPR on the surrounding environment dielectric properties is seldom mentioned.

For smaller particles, the dielectric constant of surrounding environment becomes an important impact factor [12]. It has been reported that the plasmon resonant frequency and intensity intimately relate to the dielectric of surrounding environment [15]. Moreover, due to the fact that semiconductors suffer the anodic corrosion during PEC process [13], the presence of gold metal nanoparticles and dielectric layer such as silicon dioxide could possibly improve the photocatalytic stability [2, 14]. Coating with SiO<sub>2</sub> as dielectric circumstance enables higher refractive index resulting in the red shift and stronger localization of plasmonic near-field [16, 17]. However, such combination of both gold and silicon dioxide coating has been rarely studied for photocurrent enhancement [7].

Here in, we successfully tuned the surface plasmon resonant by dielectric silicon dioxide by elaborating the fabrication of composite photoelectrodes. Specifically, ZnO nanorods array was hydrothermally synthesized on ITO glass by two steps fabrication. To study the influence of LSPR and dielectric layer on photoelectrical properties of ZnO, gold and SiO<sub>2</sub> were sputtered

in different orders. The physic mechanism as well as the advantages that arise from the unique structure-property relationship are highlighted.

## 2. Experimental

**Chemical and substrate:** Zinc nitrate [Zn(NO<sub>3</sub>)<sub>3</sub>], absolute ethanol, zinc acetate [Zn(CH<sub>3</sub>CO<sub>2</sub>)<sub>2</sub>], hexamethylenetetramine (HMT) were purchased from Sigma-Aldrich. All of chemical were used as received without further purification. Indium tin oxide (ITO) coated glasses were purchased from Sigma-Aldrich.

**ZnO nanorods array fabrication:** ZnO nanorods were synthesized on ITO glass via two steps process. Particularly, ITO glass was under surface treatment by ultrasonic agitation in acetone and absolute ethanol respectively for 10 min. To prepare the seeding solution, 10 ml of zinc acetate 0.08 M in absolute ethanol with addition of 0.25 ml water were stirred in 2 hours. The ITO substrate was dipped into zinc acetate solution for 20 s with a fixed withdrawing speed and then dried in oven at 75°C for 35 min. This process was repeated four times. The seeded substrate was then annealed in air at 220°C for 1 hour and immersed up side down in the solution of 0.025 M zinc nitrate and hexamethylenetetramine. The hydrothermal treatment was conducted at 90°C in 4 hours in an electric oven. Finally, the ITO glass was rinsed several times with water and ethanol, dried at room temperature and calcined at 450 °C in 30 min.

**Deposition of Au and SiO<sub>2</sub>:** Five different configurations including ZnO, ZnO-SiO<sub>2</sub>, ZnO-Au, ZnO-SiO<sub>2</sub>-Au, ZnO-Au-SiO<sub>2</sub> were fabricated by using magnetron sputtering on ZnO nanorods array as illustrated in Fig. 1. The Au sputter coater (VG Microtech SC500) was operated at 10 mA for 110 s with the vaccum pressure of Argon process level at 10<sup>-2</sup> mbar to produce approximately 5 nm of Au thin film. In the SiO<sub>2</sub> sputtering process using AJA sputter, the substrate was fixed at room temperature, the Ar flow at 5sccm, the power applied to the ZnO target at 130W and the pressure at 3.3 mT. By employing the above sputtering process with various orders, a series of nanostructures has been conducted.

**Materials characterization:** The morphology of ZnO nanorod array before and after sputtering were elucidated with scanning electron microscope (SEM, Hitachi 1081) at 30kV accelerating voltage. The elements detection and elemental maps were revealed by employing energy dispersive x-ray (EDX) and mapping integrated in SEM. The absorption spectra were recorded on a spectrophotometer (SHIMADZU, UV-2600 with ISR-2600 intergrating Sphere Attachment) in range of 220-830 nm with fine BaSO<sub>4</sub> powder as reference.

**Photoelectrochemical characterization:** The electrochemical characterization was conducted using three electrode-based methods with a standard electrochemical workstation (Zahner

electrik IM6). The ITO glass with difference coating layer on ZnO nanorods (effective layer 1 cm<sup>2</sup>) was the working electrode following by Ag/AgCl and Pt electrode as the reference and counter electrode respectively. 0.5 M Na<sub>2</sub>SO<sub>4</sub> (pH= 6.8) solution was the supporting electrolyte for all measurement. The light sources, white light source (halogen lamp 15V/150W) is utilized to test the photoelectrode current of sample in visible region with bias of +0.3, +0.5 and +0.7 V.

### 3. Results and discussion (Different plasmonic structures)

The morphology of ZnO nanorods after sputtering with gold and silicon oxide (Fig. 2a) reveals that the length and the diameter of the rods are 1-2 micrometers and several hundred nanometers, respectively. The SEM image of this sample is sharper than the pure one because of the conductive gold and transparent SiO<sub>2</sub>. A single horizontal ZnO nanorod on the ZnO-Au-SiO<sub>2</sub> sample was analyzed using EDX mapping to detect the individual element (Fig. 2b and Fig. 2c). The ratio between Zn and O is roughly unity presenting for ZnO with small amount of gold (0.7 %at) that uniformly distribution. Nevertheless, the silicon and indium amount mostly come from the ITO background. Due to the nature and thin layer of silicon oxide (~5nm), it is hard to be detected through EDX.

Fig. 3 shows the absorption spectra of the five as-prepared ZnO nanorods samples after sputtering. The gold decorated samples exhibit strong absorption in visible light compared to pristine ZnO and ZnO-SiO<sub>2</sub> because of surface plasmon resonant (SPR) effect. Depending on size and shape of the plasmonic structure, the SPR will have various behaviors [18]. The maximum peak is approximately 620 nm while there was no significant difference between Au coated samples. Sample with only SiO<sub>2</sub> on top of ZnO performs stronger light absorption than pure ZnO which could be explained by the higher refractive index properties of SiO<sub>2</sub>.

Fig. 4(a) plots the I-V curves of ZnO, ZnO-SiO<sub>2</sub>, ZnO-Au, ZnO-SiO<sub>2</sub>-Au, ZnO-Au-SiO<sub>2</sub> sample under white light illumination at the potential from 0 to 0.8V. For ZnO and ZnO-SiO<sub>2</sub> sample, the photocurrent are very low (in range of nanoampere). However, this value of the others are much higher (in range of microampere) and distinguished to each other. Particularly, ZnO-Au-SiO<sub>2</sub> configuration performs the highest photocurrent value meanwhile ZnO-SiO<sub>2</sub>-Au exhibits the lower value than gold decorated ZnO. Fig. 4(b) presents the photoresponse of the samples at 0.5 V bias under while light illumination. Most of the responses appear in square pulses shape corresponding to light excitation. The maximum photocurrent reaches 0.86 μA/cm<sup>2</sup> on ZnO-Au-SiO<sub>2</sub> sample, which is much larger than that of ZnO-Au (0.20 μA/cm<sup>2</sup>), ZnO-SiO<sub>2</sub>-Au (0.09 μA/cm<sup>2</sup>), ZnO (0.05 μA/cm<sup>2</sup>) and ZnO-SiO<sub>2</sub> (0.03 μA/cm<sup>2</sup>). In addition,

it can be seen from Fig. 4(b) that the photoresponse time of ZnO-SiO<sub>2</sub>-Au and ZnO-Au-SiO<sub>2</sub> are much smaller than that of ZnO-Au. Fig. 4(c) shows the transient photoresponse of ZnO-Au-SiO<sub>2</sub> sample which is stable over the times at different bias.

Fig. 5(a-e) illustrates the band gap and electron hole pathway of the samples. Fig. 5(f) sketches the light trapping structure. Due to the inertness and transparency, silicon oxide is utilized as a stabilizer, protecting layer, passive layer and dielectric layer. In the role of protecting layer, SiO<sub>2</sub> retards the interaction with oxygen that resulting in domination of electron-hole recombination [14]. This recombination significantly reduces the photocurrent. The observation in our PEC measurement (Fig. 4b) is in good agreement with this assumption. Gold nanoparticles coated ZnO nanorods is a well-known plasmonic structure under visible light irradiation. The behavior of this plasmonic structure in electrolyte is well understood in previous studies. Typically, when contact with electrolyte, the difference in fermi level of semiconductor and electrolyte redox potential leads to the band bending at the equilibrium where the space charge layer (SCL) is established [19]. In this space charge area, there would be a spatial electric field, which enhances the separation of charge carriers under light exciting. In additional to the bias voltage, incorporating metal, particularly gold with semiconductor such as ZnO results in the Schottky barrier at the interface of contact causing the greater band bending [10]. Consequently, stronger spatial electric field is beneficial for electron-hole separation. Because of the small portion of UV in white light and sunlight, the main attribution for the enhancement of photoresponse is the visible region where the surface plasmonic resonant effect (SPR) dominates. SPR effect promotes the photocurrent by enhancing the concentration of charge carriers via three non-mutually exclusive energy-transfer mechanisms, SPR-mediated charge injection from metal to semiconductor, near-field electromagnetic and scattering mechanisms. However, scattering mechanism can be ruled out of this discussion because the influence is considerable only when the structure of plasmonic metal is larger than 50 nm [11]. As observed in Fig. 3, the maximum absorption of gold decorated ZnO nanorods is approximately 620 nm, which stimulates the resonant electron up to 2 eV. The electron affinity of ZnO and work function of Au are 4.35 eV and 5.1 eV respectively resulting in the Schottky barrier at 0.75 eV as shown in Fig. 5c. The energetic electrons have more than enough potential to jump up through Schottky barrier into ZnO conduction band. The near-field electromagnetic mechanism is described as the interaction of the semiconductor with the strong SPR-induced electric field localized nearby at the metallic nanostructure [8]. When a semiconductor is in contact with photo-excited plasmonic structure, the intense field will

accelerate the rate of electron-hole pair formation. All superior effects of gold nanoparticles loading contributed for the great enhancement in photocurrent under white light irradiation compared to pristine ZnO nanorods as presented in Fig. 4a and Fig. 4b.

In ZnO-SiO<sub>2</sub>-Au configuration, SiO<sub>2</sub> layer acts as insulator between gold nanoparticles and ZnO nanorods. The SCL is therefore, narrowed leading to less intensive spatial electric field. This insulator also weakens the near field electromagnetic, which significantly depresses the electron-hole separation. On the other hand, under visible light irradiation, the energetic electron can tunnel through the SiO<sub>2</sub> layer to inject in to the ZnO nanorods (Fig. 5d). These are reasons for the lower photocurrent of ZnO-SiO<sub>2</sub>-Au than only gold decorated ZnO nanorods but still higher than pristine ZnO nanorods (Fig. 4a).

Interestingly, ZnO-Au-SiO<sub>2</sub> configuration performed an outstanding photoresponse compared to that of the others. This configuration is simply ZnO-Au with a thin layer of dielectric as outer shell. Beside the positive effects of gold nanoparticles decorated ZnO nanorods, there are several factors contributing for the high photocurrent density. The gold plasmonic structure alone has the possibility to interact with the electrolyte components that decreases the amount of energetic electrons into the ZnO nanorods. SiO<sub>2</sub> layer is able to inhibit the electron in conduction state interacting with the electrolyte components. Thus, SiO<sub>2</sub> not only increases the injection efficiency but the presence of negative charge localized in SiO<sub>2</sub> film also creates an effective electron transport channel in the ZnO backbone to suppress the carriers recombination by inducing a formation of electron depletion layer and band up bending at the nanorod surface [7] as shown in Fig. 5e. Using the same plasmonic configuration, the simulation results of Xu et al. group indicated that semiconductor-plasmonic metal-dielectric layer exhibits more intensive electric field at the semiconductor/plasmonic metal interface and deeper penetration into the semiconductor than the others [7]. Furthermore, the higher refractive index of dielectric layer than that of electrolyte establishes a light trap structure (Fig. 5f) which lengthens the pathway of incoming light. Hence, SiO<sub>2</sub> layer enhances the absorption opportunities of semiconductor and plasmonic metal leading to better electron-hole separation.

It's meaningful to have the fast photoresponse in some applications [20]. It can be seen from Fig. 4(b) that the SiO<sub>2</sub> coated sample without the interaction with plasmonic structure performed the longest photoresponse time in both rising and decaying term which are not desirable for many applications. On the other hand, when combining with plasmonic structure, SiO<sub>2</sub> and Au coated samples show a rapid photoresponse compared to gold decorated ZnO alone. The delaying of photoresponse is due to the recombination of photoexcited holes

recombine with electrons in traps states [13]. In the experiment of Murphy et al, the extremely deep holes trap in wide band gap semiconductor such as ZnO attributes for slow photoresponse [21]. They also pointed out the passivation with SiO<sub>2</sub> significantly depress the density of deep traps at the ZnO surface. This is in good agreement with our data point that the plasmonic sample with SiO<sub>2</sub> passivation layer performed rapid response to light.

#### **4. Conclusions**

In this work, plasmonic enhancement of the photoelectrical performance of gold decorated ZnO nanorods have been observed in visible region. The function and role of plasmonic Au are identified as: (1) enhancing the band bending resulting in the strong spatial electric field, (2) SPR-mediated charge injection from metal to semiconductor, (3) near-field electromagnetic. The presence of thin dielectric layer between gold and ZnO nanorods weaken the response to visible light owing to the near field magnetic inhibition induced by passivation effect. The ZnO-Au-SiO<sub>2</sub> exhibits superior photoresponse which is four times higher than ZnO-Au. This is ascribed to (1) SiO<sub>2</sub> intensified SPR-mediated hot electron injection due to its higher dielectric index, (2) light trapping structure, (3) effective electron transportation channel through ZnO backbone. Additionally, SiO<sub>2</sub> passivates the trap site at the surface of semiconductor resulting in fast photoresponse. This work strengthens the understanding on the design engineering for high performance photocatalysts of solar to fuel energy conversion. The findings from this study will be informative for the design of plasmonic photocatalysts or optoelectronic devices, such as photovoltaic and water-splitting cells.

#### **Acknowledgements**

Norwegian Research Council-FRINATEK programme (231416/F20), the Norwegian PhD Network on Nanotechnology for Microsystems (221860/F40) and EEA-Poland (237761) are acknowledged for their financial support.

#### **References**

- [1] T. İpeksaç, F. Kaya, C. Kaya, Hydrothermal synthesis of Zinc oxide (ZnO) nanotubes and its electrophoretic deposition on nickel filter, *Materials Letters*, 100 (2013) 11-14.
- [2] J. Lu, H. Wang, D. Peng, T. Chen, S. Dong, Y. Chang, Synthesis and properties of Au/ZnO nanorods as a plasmonic photocatalyst, *Physica E: Low-dimensional Systems and Nanostructures*, 78 (2016) 41-48.
- [3] R. Dom, L.R. Baby, H.G. Kim, P.H. Borse, Enhanced Solar Photoelectrochemical Conversion Efficiency of ZnO:Cu Electrodes for Water-Splitting Application, *International Journal of Photoenergy*, 2013 (2013) 1-9.
- [4] H. Zhang, G. Chen, D.W. Bahnemann, Photoelectrocatalytic materials for environmental applications, *Journal of Materials Chemistry*, 19 (2009) 5089.

- [5] Z. Liu, W. Hou, P. Pavaskar, M. Aykol, S.B. Cronin, Plasmon resonant enhancement of photocatalytic water splitting under visible illumination, *Nano letters*, 11 (2011) 1111-1116.
- [6] W. Chen, Y. Lu, W. Dong, Z. Chen, M. Shen, Plasmon mediated visible light photocurrent and photoelectrochemical hydrogen generation using Au nanoparticles/TiO<sub>2</sub> electrode, *Materials Research Bulletin*, 50 (2014) 31-35.
- [7] Z. Xu, Y. Lin, M. Yin, H. Zhang, C. Cheng, L. Lu, X. Xue, H.J. Fan, X. Chen, D. Li, Understanding the Enhancement Mechanisms of Surface Plasmon-Mediated Photoelectrochemical Electrodes: A Case Study on Au Nanoparticle Decorated TiO<sub>2</sub> Nanotubes, *Advanced Materials Interfaces*, 2 (2015) n/a-n/a.
- [8] Suljo Linic, Phillip Christopher, D.B. Ingram, Plasmonic-metal nanostructures for efficient conversion of solar to chemical energy, *Nature Materials*, 10 (2011) 911.
- [9] P. Wang, D. Wu, Y. Ao, C. Wang, J. Hou, ZnO nanorod arrays co-loaded with Au nanoparticles and reduced graphene oxide: Synthesis, characterization and photocatalytic application, *Colloids and Surfaces A: Physicochemical and Engineering Aspects*, 492 (2016) 71-78.
- [10] M. Mahanti, D. Basak, Enhanced ultraviolet photoresponse in Au/ZnO nanorods, *Chemical Physics Letters*, 612 (2014) 101-105.
- [11] D.D. Evanoff, Jr., G. Chumanov, Synthesis and optical properties of silver nanoparticles and arrays, *Chemphyschem : a European journal of chemical physics and physical chemistry*, 6 (2005) 1221-1231.
- [12] K. Lance Kelly, Eduardo Coronado, Lin Lin Zhao, G.C. Schatz, The Optical Properties of Metal Nanoparticles: The Influence of Size, Shape, and Dielectric Environment, *The Journal of Physical Chemistry B*, 107 (2003) 668-677.
- [13] Y.C. Pu, G. Wang, K.D. Chang, Y. Ling, Y.K. Lin, B.C. Fitzmorris, C.M. Liu, X. Lu, Y. Tong, J.Z. Zhang, Y.J. Hsu, Y. Li, Au nanostructure-decorated TiO<sub>2</sub> nanowires exhibiting photoactivity across entire UV-visible region for photoelectrochemical water splitting, *Nano letters*, 13 (2013) 3817-3823.
- [14] P. Mulvaney, L.M. Liz-Marzán, M. Giersig, T. Ung, Silica encapsulation of quantum dots and metal clusters, *Journal of Materials Chemistry*, 10 (2000) 1259-1270.
- [15] Teera Butburee, Yang Bai, Jian Pan, Xu Zong, Chenghua Sun, G. Liu, a.L. Wang, Step-wise controlled growth of metal@TiO<sub>2</sub> core-shells with plasmonic hot spots and their photocatalytic properties†, *Journal of Materials Chemistry A*, 2 (2014) 12776.
- [16] S.K. Medda, S. De, G. De, Synthesis of Au nanoparticle doped SiO<sub>2</sub>-TiO<sub>2</sub> films: tuning of Au surface plasmon band position through controlling the refractive index, *Journal of Materials Chemistry*, 15 (2005) 3278.
- [17] Z.W. Seh, S. Liu, M. Low, S.Y. Zhang, Z. Liu, A. Mlayah, M.Y. Han, Janus Au-TiO<sub>2</sub> photocatalysts with strong localization of plasmonic near-fields for efficient visible-light hydrogen generation, *Advanced materials*, 24 (2012) 2310-2314.
- [18] K. Lance Kelly, Eduardo Coronado, Lin Lin Zhao, G.C. Schatz, The Optical Properties of Metal Nanoparticles: The Influence of Size, Shape, and Dielectric Environment, *Journal of Physical Chemistry B*, 107 (2003) 668-677.
- [19] I. Paramasivam, H. Jha, N. Liu, P. Schmuki, A review of photocatalysis using self-organized TiO<sub>2</sub> nanotubes and other ordered oxide nanostructures, *Small*, 8 (2012) 3073-3103.
- [20] S. Dhara, P.K. Giri, Improved fast photoresponse from Al doped ZnO nanowires network decorated with Au nanoparticles, *Chemical Physics Letters*, 541 (2012) 39-43.

[21] T.E. Murphy, K. Moazzami, J.D. Phillips, Trap-Related Photoconductivity in ZnO Epilayers, Journal Of Electronic Materials, 35 (2006) 543.

## Figure

**Figure 1.** The schematic of fabrication process.

**Figure 2.** The SEM image of a) ZnO nanorods with Au and SiO<sub>2</sub> deposition b) The EDS profiles of ZnO-Au-SiO<sub>2</sub> sample.c) Mapping profile of the sample on single rod.

**Figure 3.** UV-VIS absorption spectra of the different configurations of ZnO nanorods with and without coating.

**Figure 4.** a) I-V curves of the samples under white light illumination b) Photoresponses of the samples at 0.5 V bias under white light illumination c) The transient photoresponse of the ZnO-Au-SiO<sub>2</sub> sample at 0.3, 0.5, 0.7 V bias.

**Figure 5.** Band diagrams of a) the ZnO sample, b) the ZnO-SiO<sub>2</sub> sample, c) the ZnO-Au sample, d) the ZnO-SiO<sub>2</sub>-Au sample, and e) of the ZnO-Au-SiO<sub>2</sub> sample, f) Illustration of light trapping in the sample with SiO<sub>2</sub> coating.

Figure 1

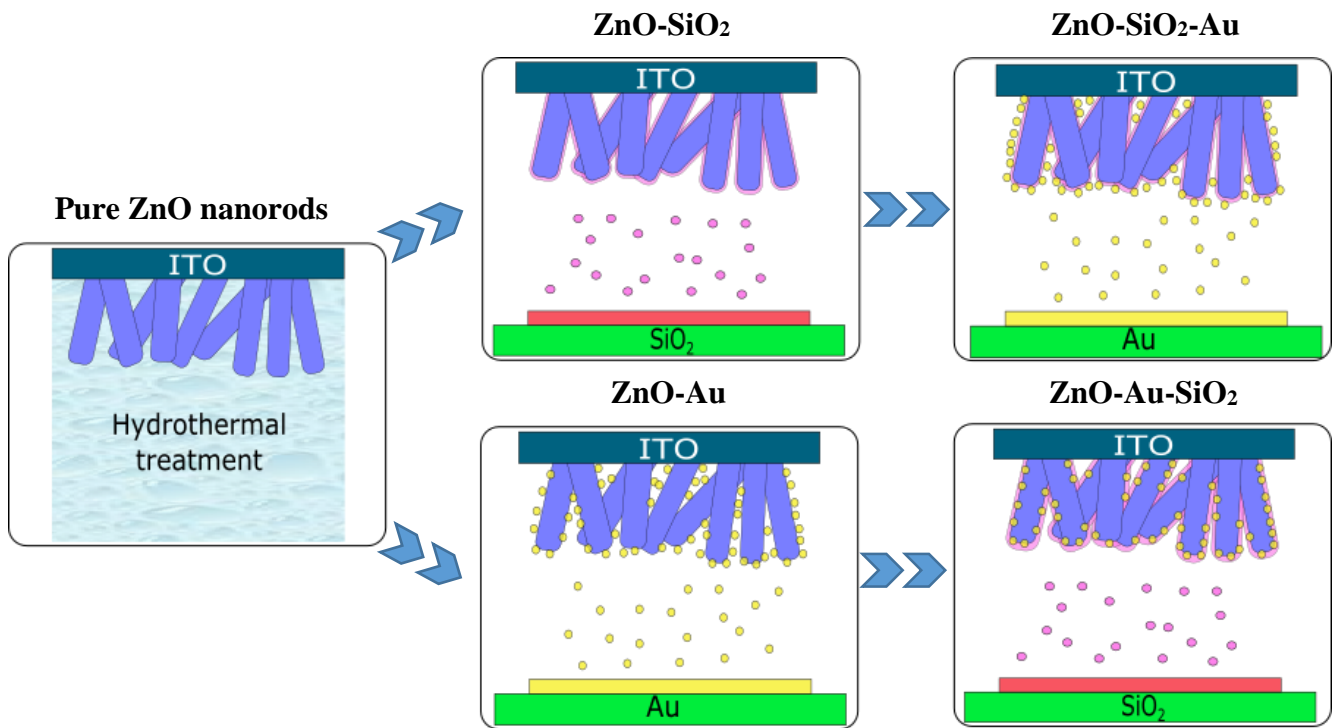


Figure 2

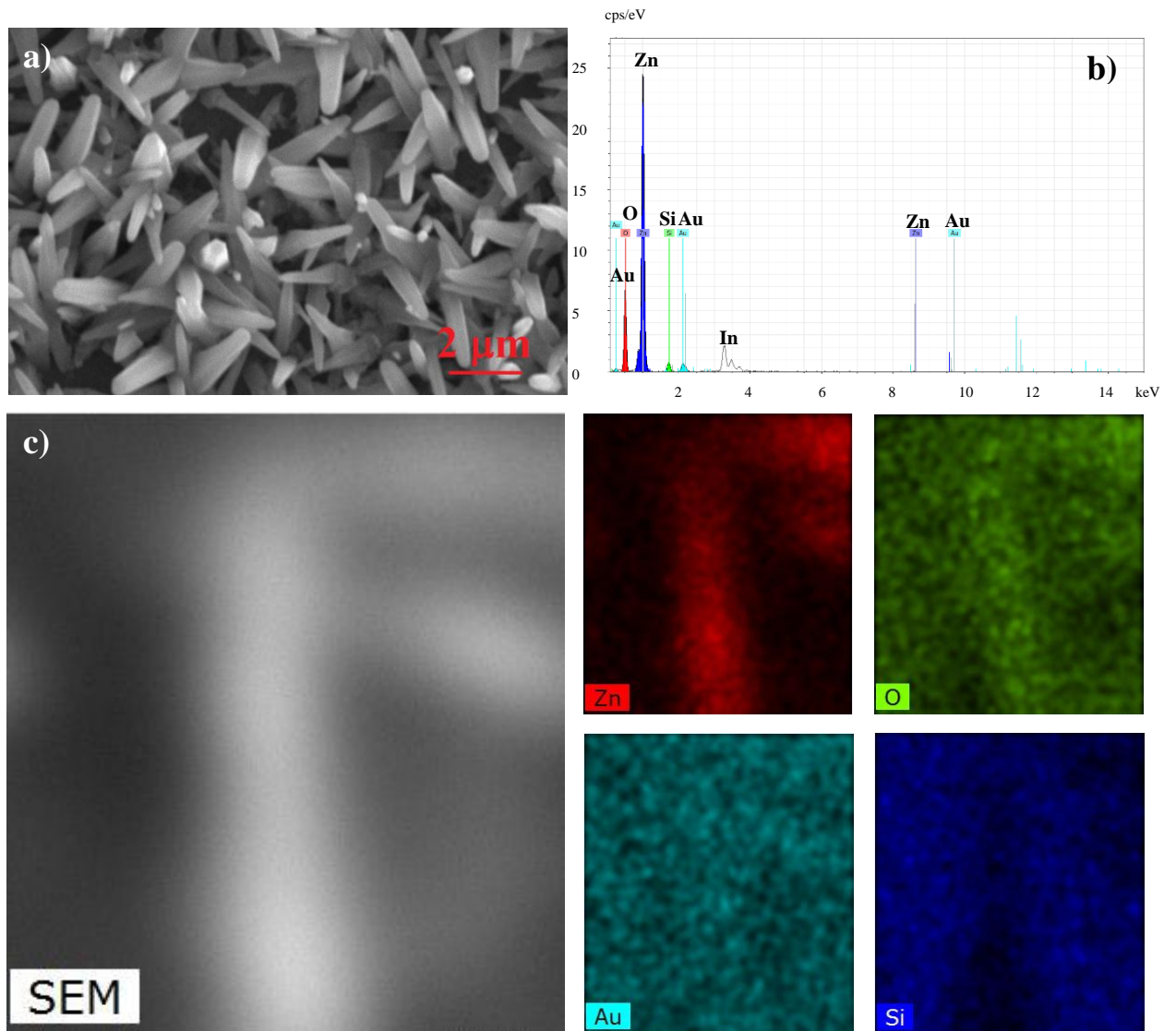


Figure 3

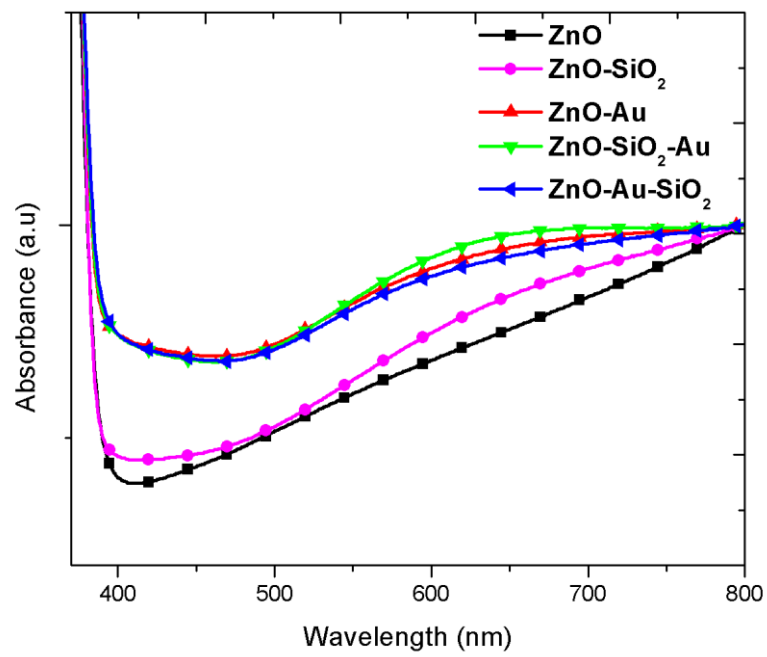


Figure 4

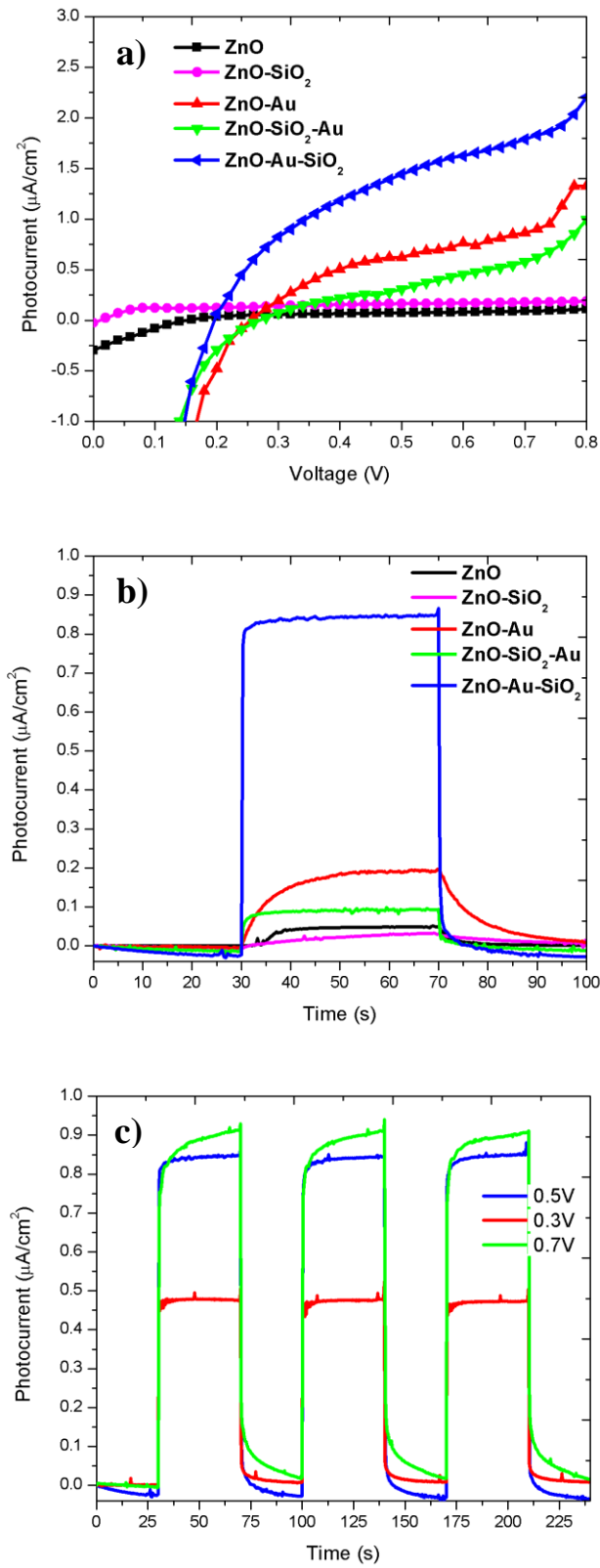


Figure 5

